Frequency swept fibre laser for wind speed measurements

Anders Tegtmeier Pedersen
Ph.D. Thesis
December 2011

DTU Fotonik
Department of Photonics Engineering

DTU Fotonik
Department of Photonics Engineering

Technical University of Denmark

Frequency swept fibre laser for wind speed measurements

PhD thesis

Anders Tegtmeier Pedersen

Academic Supervisors:
PhD Petter Lindelöw-Marsden &
Professor, Dr. Techn. Karsten Rottwitt

DTU Fotonik
Ørsteds plads 343
2800 Kongens Lyngby
Denmark

Technical University of Denmark

December, 2011

Abstract

This PhD thesis builds around a light source forming the basis for a novel type of wind measuring lidar. The lidar emits a train of laser pulses with each pulse being separated from its neighbours in frequency, while being closely spaced in time, thus combining the advantages of conventional continuous wave (CW) and pulsed lidars. A light source capable of emitting such a pulse train is suggested. A theoretical description of all components constituting the light source is presented, and a time dependent model is developed and compared to measurements as well as to previous theoretical work from the scientific literature. The model presented shows good agreement with the experimental results regarding the pulse train envelope as well as the individual pulses. A model adopted from the literature is subsequently expanded to incorporate frequency components other than the main signal frequency and compared to measurements of individual pulse spectra. Critical issues such as various contributions to noise, in particular amplified spontaneous emission (ASE), are investigated.

The realized frequency stepped pulse train (FSPT) emitting light source has been incorporated into a modified CW lidar, and the ability to measure wind speeds as well as the direction successfully demonstrated. A challenge still remains in the improvement of the signal to noise ratio (SNR), though.

Additionally, a theoretical study of the feasibility of mounting lidars in the blades of wind turbines for active pitch angle control has been undertaken with a positive outcome encouraging an experimental trial to measure wind with a such construction. Therefore, a small telescope CW lidar designed for turbine blade integration has been tested in a high performance wind tunnel, and very good agreement with reference measurements has been obtained.

Resumé

Denne ph.d.-afhandling omhandler en lyskilde, som udgør grundlaget for en ny type vindmålende lidar. Denne lidar udsender en serie af laser pulser hvor hver puls er adskilt fra sine naboer i frekvensdomænet, men tæt samlet i tidsdomænet, og dermed kombinerer den fordelene ved konventionelle CW- og pulsede lidarer. En lyskilde, som er i stand til at udsende et sådan pulstog, foreslås. En teoretisk beskrivelse af alle komponenterne, som udgør denne lyskilde, bliver givet, og en tidsafhængig model er blevet udviklet og sammenlignet med målinger så vel som teoretisk arbejde tidligere beskrevet i den videnskabelige litteratur. Den præsenterede model viser god overensstemmelse med de eksperimentelle resultater hvad angår pulstogets samlede indhyldningskurve så vel som de individuelle pulser. En tidligere publiceret model bliver efterfølgende udvidet til også at inkorporere andre frekvenskomponenter end den dominerende signalfrekvens og sammenlignet med målinger af individuelle pulsspektre. Kritiske emner så som forskellige støjbidrag, i særdeleshed forstærket spontan emission, bliver undersøgt.

Den realiserede lyskilde som emitterer pulstog bestående af frekvensskiftede pulser, er blevet inkorporeret i en modificeret CW lidar, og dens formåen til at måle vindens fart så vel som dens retning demonstreret. Der ligger dog stadig en udfordring i at forbedre signal-støj-forholdet.

Ydermere er der udført et teoretisk studie af muligheden for at montere lidarer i vindmøllevinger for på den måde aktivt at styre vingens pitch vinkel. Et yderst positivt resultat af dette studie ledte til en eksperimentel undersøgelse af muligheden for at måle vindhastigheder med en sådan konstruktion. En CW lidar med en lille teleskop-enhed designet med henblik på vingemontering er derfor blevet testet i en højtydende vindtunnel med særdeles god overensstemmelse med referencemålinger som resultat.

Preface

The present thesis represents the outcome of a PhD project carried out at DTU Fotonik (Department of Photonics Engineering), Technical University of Denmark from 2008 to 2011. The work has mainly taken place at DTU Fotonik, but a three month external research stay was spent at Natural Power/ZephIR, Ledbury, England from January to April 2011. The PhD project was supervised by Petter Lindelöw-Marsden (formerly DTU Risø) and Professor Karsten Rottwitt (DTU Fotonik). Petter Lindelöw-Marsden left DTU in the autumn of 2010 and a new supervisor was not appointed.

Anders Tegtmeier Pedersen
Kongens Lyngby, December 31, 2011.

Notes to the printed thesis

The results of this thesis were presented for public examination and debate on March 22, 2012 at the Technical University of Denmark. The evaluation committee consisted of Group Leader Christian Pedersen (DTU Fotonik), Dr. Chris Hill (Malvern Lidar Consultants), and CTO Christian Vestergaard Poulsen (NKT Photonics).

Some minor corrections and additions including an update of the list of publications have been made to the originally submitted thesis before printing.

Anders Tegtmeier Pedersen
Kongens Lyngby, May 21, 2012.

Acknowledgements

First of all, I would like to thank my supervisors Petter Lindelöw-Marsden and Karsten Rottwitt. Petter for introducing me to the fascinating world of lidars and for many fruitful discussions, and Karsten for believing in me, his always open door, and of course the hours spent discussing physics. Secondly, I thank my good colleague Anders Sig Olesen for great collaboration and many interesting hours in the lab as well as the office. Thank also goes to the Wind Energy Division at DTU Risø, notably Torben Mikkelsen and Jakob Mann for great help and support. I would furthermore like to express my sincere gratitude to all the people at Natural Power/ZephIR, where I spent three interesting months, for their kindness and warm hospitality, and especially to Mike Harris for sharing his huge knowledge and for his almost infinite patience. NKT Photonics and OFS Fitel Denmark are thanked for supplying me with a laser and optical fibres. I would also like to thank the many people who have passed through the office over the years and contributed to lighten up the days including Alessio Stefani, Lars Rishøj, Martin Pedersen, Michael Frosz, Anna Chiara Brunetti, Valentina Cristofori, Kristian Nielsen, and Toke Lund-Hansen. Last but certainly not least, I would like to thank Thomine Stolberg-Rohr for her support, meticulous proofreading, and for asking so many intelligent questions.

List of publications

The work presented in this thesis has resulted in the following publications

Scientific journals

- A. T. Pedersen, A. S. Olesen, and K. Rottwitt, Accurate simulation of Raman amplified lightwave synthesized frequency sweeper. *Journal of the Optical Society of America B: Optical Physics*, **28**(6): 1493–1497 (2011).

Conference proceedings

- A. T. Pedersen, and P. Lindelöw, Investigation of noise in Lightwave Synthesized Frequency Sweeper seeded LIDAR anemometers from leakage through the Acousto Optic Modulators. *Proceedings of CLRC 15th Coherent Laser Radar Conference*, (2009).

- A. T. Pedersen, and K. Rottwitt, Raman assisted lightwave synthesized frequency sweeper. *Proceedings of Optical Sensors – OSA*, (2010).

- A. S. Olesen, A. T. Pedersen, and K. Rottwitt, Simultaneous measurements of wind speed at multiple distances without range ambiguity. *Proceedings of CLRC 16th Coherent Laser Radar Conference*, (2011).

- A. S. Olesen, A. T. Pedersen, and K. Rottwitt, Frequency stepped pulse train modulated wind sensing lidar. *Proceedings of Lidar Remote Sensing for Environmental Monitoring – SPIE*, **8159**: 81590O-8 (2011).

- A. T. Pedersen, B. F. Montes, J. E. Pedersen, M. Harris and T. Mikkelsen, Demonstration of short-range lidar in high-performance wind tunnel. *Proceedings of European Wind Energy Association Conference*, (2012)

Book chapters

- K. Rottwitt, A. C. Brunetti, J. Lægsgaard, J. Weirich, L. S. Rishøj, X. Liu, L. Scolari, M. E. V. Pedersen, A. T. Pedersen, H. Steffensen and L. Wei, Enhancing the capacity of light. *Chapter in Beyond optical horizons - Today and tomorrow with photonics*, 75–87 (2009)

Papers in preparation

- A. T. Pedersen, and K. Rottwitt, Spectral content of optical pulses generated by a lightwave synthesized frequency sweeper.
- E. Branlard, A. T. Pedersen, N. Angelou and J. Mann, Retrieving wind statistics from the average spectrum of a continuous wave lidar

Contents

CHAPTER 1

Introduction

Knowledge of atmospheric winds is important within several sciences and affects many aspects of modern life, for example in meteorology where wind measurements are critical for making accurate weather forecasts or in aerospace where turbulence near the ground constitute a risk for an airplane during take off and landing. Another example is within the wind energy industry; wind turbines are being installed with increasing speed in large parts of the world [1], but the power output and life expectancy of a turbine are sensitive to the wind conditions at the site and it is therefore important to asses the wind field of the specific site before installing the turbine.

Measurement of wind speed is performed using an anemometer and these come in a variety of different configurations, relying on different physical properties. Perhaps best known is the cup anemometer which measures the rotational speed of a small propeller driven by the wind, but also sonic anemometers, measuring the transit time of an ultrasonic pulse depending on the wind speed, are common [2]. Hot wire anemometers measure the resistance in an electrically heated metal wire and are often used for turbulence measurements [3], and Pitot tubes measure the pressure difference inside and outside a tube caused by the flow of air [4]. These anemometers all have in common that they measure the wind locally, but also remotely measuring anemometers are available. These include sodars which work by emitting an acoustic pulse and then measure the Doppler shifted echo reflected from temperature inhomogeneities in the atmosphere [5], and lidars which rely on similar principles but utilize laser light scattered off small particles in the atmosphere. A more thorough description of lidars is given in Chapter 2.

Lidars for wind measurements have since 2003 (when the commercial *ZephIR* wind lidar from the British QinetiQ, and now marketed by Natural

Power [6], was introduced) gained increasingly in popularity and are now available from a number of companies including the French Leosphere [7], the British SgurrEnergy [8], and the American Catch the Wind [9]. Not least within the wind energy industry have wind lidars found use and with good reason. As mentioned above it is important to evaluate the wind field before installing a turbine and this is traditionally done with an accurately calibrated cup anemometer mounted on a tall mast at hub height. However, with turbines growing taller and taller and with larger and larger rotor diameters such masts become increasingly expensive and cumbersome to erect. Lidars on the other hand can be ground based, can measure at different heights simultaneously thus covering the top as well as the bottom of the rotor disc, and can easily be moved to a different location when the measurement is over. Also within aerospace wind lidars are emerging and have for example been implemented for turbulence monitoring on runways in order to safely minimize time between landings [10]. Even the speed of an aeroplane measured from the plane itself has been measured [11].

This thesis is focused on the development and description of a light source for use in a novel type of wind measuring lidar. The project is thus placed in the cross field between the worlds of lasers and photonics and wind engineering, and one of the major challenges of the project has been to bridge these worlds; a challenge not necessarily reflected in the thesis. However, the outcome of the project has first and foremost been the development of a frequency shifted pulse emitting light source and the use of it in a lidar system which is now capable of remote measurement of wind speeds. Secondly, a substantial part of the thesis is concerned with lidar measurements inside a high performance wind tunnel. This is a novel application of a wind lidar and marks an advance in the state of the art within the field. This part therefore also represents a considerable amount of work from the initial preparations with design of the system over the actual measurements to the processing of data.

1.1 Thesis structure

The thesis consists of eight chapters organized as follows.

Chapter 2 - **Doppler lidar** gives an introduction to lidar wind speed measurements in general. The basic lidar setup is described together with the important concept of heterodyne detection. A vital part of the wind lidar is the laser and the requirements regarding wavelength, spectral stability, and

power are discussed. Finally, the principles behind a hybrid lidar combining the strengths of conventional continuous wave (CW) and pulsed lidar systems are presented.

Chapter 3 - **Blade-mounted lidar system** presents a mainly theoretical study of the possibility of mounting lidars in the blades of wind turbines for active pitch angle control. Different technical risks potentially impeding the wind speed measurement with a blade-mounted lidar are analyzed. It is concluded that these risks have negligible impact. The last part of the chapter is devoted to a small experimental study of how cross-talk in the lidar circulator can lead to a severe increase in noise levels.

Chapter 4 - **Wind tunnel trial** describes a measurement campaign where a small telescope CW lidar designed for turbine blade integration is tested in a high performance wind tunnel. The lidar is tested in various wind speeds from 5 m/s and up to 75 m/s, under different angles-of-attack. Good correlation with reference measurements is found. The concept of spectral broadening is discussed and evaluated in relation to a high angle-of-attack measurement, and also a measurement of turbulent wind flow is presented. Finally the uncertainties associated with the lidar measurements are analyzed.

Chapter 5 - **Frequency stepped pulse train** introduces a method for generating a succession of optical pulses each separated in frequency from its neighbours and the experimental setup called a lightwave synthesized frequency sweeper (LSFS) is described in detail. The LSFS is realized in two configurations one comprising an Erbium doped fibre amplifier (EDFA) and one comprising a Raman amplifier. A time dependent model of the LSFS is developed and compared against a time independent model adopted from the literature as well as experimental measurements.

Chapter 6 - **FSPT in the spectral domain** is devoted to describing the output of the LSFS in the frequency domain. The spectrum of each individual pulse is measured and compared against the predictions of the time independent model which is expanded to incorporate frequency components other than the main signal frequency. At the end of the chapter it is shown how the LSFS setup can be used to measure the linewidth of narrowband fibre lasers, and a short description of a different frequency swept laser source is given.

Chapter 7 - **Wind speed measurements with an FSPT modulated lidar**

presents measurements of atmospheric wind speeds performed with the hybrid lidar introduced in Chapter 2. The chapter describes three different measurement campaigns, between which modifications and improvements to the lidar have been made and it is shown how these modifications lead to improved measurements. Measurements of the noise level in the lidar spectra are presented and discussed in the end of the chapter.

Finally, the thesis is concluded in Chapter 8 and future work in the project is discussed.

CHAPTER 2

Doppler lidar

Lidar (light detection and ranging) is an umbrella term for different systems which utilize electromagnetic radiation in the optical part of the spectrum, typically from 400 nm to around 10 μm, for remote detection and sensing [12]. Lidars find use in a number of different applications from car speed measurement to glacier growth monitoring to measuring atmospheric gases or temperature [13, 14]. In its simplest form the lidar works by emitting a light pulse and measuring the time for backscattered reflections to arrive back at the starting point, and from this calculating the distance to the object causing the reflection. If the pulse repetition rate is sufficiently high, it is possible to measure the speed of a relative motion in the line-of-sight (LOS) between the lidar and the object, e.g. a speeding car, with high accuracy. Other lidars use more complicated schemes and measure for example some property of the backscattered light such as power, frequency, or polarization [2].

Just as different lidars rely on different working principles, they also come in different configurations. For example they can be either monostatic or bistatic. Monostatic systems have only one telescope or transceiver, used for both transmitting the output light as well as collecting the backscattered light. In bistatic systems the transmitting and receiving paths are separated in two telescopes. The bistatic lidar only collects light scattered from the volume in space where the fields of view of the transmitter and receiver overlap, and therefore a very tight spatial confinement of the measurement can be achieved [15]. The drawback of bistatic lidars is that it is difficult in practice to adjust the telescopes to obtain a good spatial overlap between the fields of view. Hence, bistatic lidars are more cumbersome to work with in addition to being more sensitive to vibrations which can easily disturb the alignment of the beams [16], and many lidars are therefore monostatic. Another distinction between

lidar systems lies in whether the transmitted beam is focused or collimated. The use of a focused beam gives, as the bistatic configuration, spatial confinement and in general a superior collection efficiency, but its range is in return limited to a few hundred meters [2]. Finally, a lidar can operate either in continuous or pulsed mode, referring to whether it emits continuous wave (CW) light or pulsed light. The pulsed system is also called a *range gated* system because the time-of-flight (TOF) from when a pulse is emitted to when the backscattered signal is received may be used to calculate the range at which light was scattered. When measuring on a dispersed target such as the atmosphere, light may scatter in all heights as the pulse propagates and information from different ranges can thus be retrieved. The spatial confinement is defined by the pulse length but can be improved at a desired range by using a focused beam. This, though, reduces our ability to measure simultaneously at different heights. The pulse repetition rate of the pulsed lidar must be sufficiently low to ensure that scattered returns from two pulses do not arrive simultaneously and thereby introduce ambiguities regarding the range. As a consequence it operates with a low duty cycle. A CW lidar needs to have a focused beam to obtain spatial confinement, so to measure at different ranges the focus must be changed. In exchange it operates with a high duty cycle compared to the pulsed lidar.

2.1 Doppler wind lidar

One specific type of lidar is the Doppler wind lidar which is used for measuring the speed of the wind and this will be the center of attention for the rest of this thesis. The Doppler wind lidar works by measuring the change in frequency induced on the backscattered laser light by the relative motion of aerosols, e.g. dust, pollen, or water droplets, upon which light is scattered. By assuming that these aerosols move with the wind, the wind speed in the LOS is calculated from

$$v_{\mathrm{LOS}} = \frac{c}{2}\frac{\Delta\nu_D}{\nu} = \frac{1}{2}\lambda\Delta\nu_D, \tag{2.1}$$

where c is the speed of light, $\Delta\nu_D$ is the induced Doppler shift, and ν and λ are the frequency and wavelength, respectively, of the transmitted laser light. To measure the 3D wind velocity it is necessary to point the laser beam in different directions in fast succession and from the LOS speeds estimate the velocity. This procedure implies an assumption of homogeneous wind speed over the points in space being probed, an assumption that might break down if the air flow is turbulent [17].

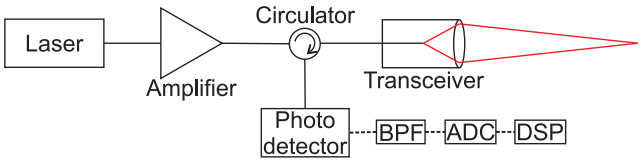

Figure 2.1: Schematic drawing of the lidar setup used in this project. Optical fibres are illustrated using solid lines, electrical wires with dashed lines, and the infrared laser light with red.

The basic outline of a monostatic Doppler lidar, as used in this project, is shown in Fig. 2.1. On the optical side it relies on a laser and an amplifier to provide the output light at an adequate power level; typically around 1 W. A circulator directs the light to the transceiver unit which focuses it into the atmosphere. A fraction of the light is reflected on the end-facet of the delivery fibre and travels back through the system together with light backscattered in the atmosphere collected by the telescope. This reflection is used as the very important reference or local oscillator (LO) as will be explained in Section 2.1.2. Alternatively to using the reflection as reference, one could tap light directly from the laser and direct it to the photo detector (PD). This has the advantage that by the use of a frequency shifting component, the lidar will be able to detect the sign of the Doppler shift, but it also requires control of the polarization of both signal and reference as well as elimination of the end-facet reflection.

Signal and reference are directed via the circulator to the PD which produces a time varying electrical signal. This signal is ultimately converted into a spectrum via a discrete Fourier transform (DFT) operation in a digital signal processor (DSP) unit e.g. a computer, but to reduce noise levels in the spectrum the signal is first band pass filtered. For the lidar used in this project, the bandpass filter (BPF) has a pass band from 100 kHz to 25 MHz. This is in the low end to reduce the influence of relative intensity noise (RIN) from the laser which can reduce the signal to noise ratio (SNR) considerably, and in the high end to avoid noise at higher frequencies to be aliased into the spectrum and degrade the SNR. An analog-to-digital converter (ADC) converts the analog signal into a digital signal.

2.1.1 Laser

Very early ranging lidar systems used powerful flash lamps as light sources, but after its invention the laser quickly became the undisputed light source of choice [12]. The CO_2 laser dominated because of its ability to produce stable single frequency output, in pulsed and CW operation, not too high atmospheric attenuation, and relative eye safety [12]. In recent years, however, the fibre laser has taken an increasingly dominating part, not least in commercial systems [7, 6, 9], because of e.g. its compactness, ease of use, spectral quality, and availability at suitable wavelengths. Also semiconductor lasers, however, have been demonstrated for use in wind lidars and might very well have a role to play in the future of lidars [18].

Among the criteria a wind lidar puts on a laser, is that there should be a reasonable trade-off between atmospheric transmission and backscatter coefficient. In the near infrared region the atmospheric transmission generally increases with the wavelength, but with strong absorption bands e.g. around 1400 nm and 1900 nm as seen in Fig. 2.2. The backscatter coefficient, on the other hand, favours shorter wavelengths. For lidars measuring hard targets at long ranges, transmission has the highest priority and therefore wavelengths of 2 μm or higher are favoured, but for lidars measuring dispersed targets at medium ranges up to a few hundred meters as is the case for the lidars considered in this thesis, the wavelength range around 1550 nm constitute a good compromise [19]. The choice of this wavelength range is strongly supported by the fact that fibre lasers based on Erbium doped silica fibres together with various optical components operating at these wavelengths have become readily available because of the low loss of silica optical fibres [20] and their resulting use within the optical communication industry. In fact this makes the 1550 nm region the obvious choice of wavelength for wind lidars in general. Furthermore this region has the advantage of being relatively eye-safe (see Fig. 2.2 right axis) which becomes important if the lidar is operating unguarded in a location where untrained personnel might have access to it.

As will be explained in Section 2.1.2 the lidars considered in this project rely on self-heterodyne detection where the backscattered light is mixed with a copy of the emitted light resulting in a beat spectrum in the radio frequency (RF) part of the electromagnetic spectrum and with a peak at the frequency corresponding to the difference in frequency between the two optical fields. In the absence of a wind signal the width of this peak depends on the phase correlation between the two fields and will in theory be a delta spike if the fields are fully correlated [21]. If, however, the signal is delayed compared to the refer-

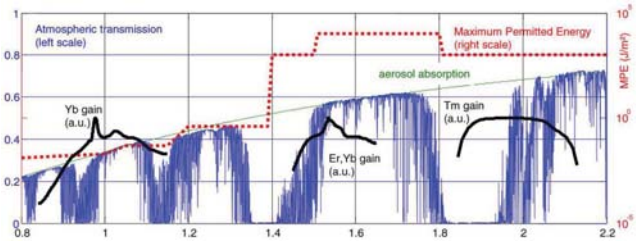

Figure 2.2: Transmission spectrum of the atmosphere (blue) together with maximum permitted energy for 100 ns pulses (red) and laser gain curves for Yb, Er-Yb and Tm fibre lasers. It is seen how the region around 1550 nm offers a good compromise between atmospheric transmission and eye-safety. Figure reproduced from [19].

ence, as is the case in a lidar measurement where the signal is emitted into the atmosphere, the correlation deteriorate and the peak broadens with a decrease in SNR as result. In a wind speed measurement the peak is further broadened by e.g. turbulence, and it is important that the width is not dominated by the laser [2]. The width due to beating of the laser with a delayed copy of itself corresponding to two times the maximum target range should thus be smaller than the width originating from turbulence. Furthermore, as the RF spectrum is often calculated using a DFT, the spectral width should be smaller than the bin width which for a CW lidar often is of the order of a few hundred kilohertz. These demands are in general met by fibre lasers.

2.1.2 Heterodyne detection

The frequency shift induced by the wind is for a laser operating around 1550 nm typically up to a few tens of megahertz. Compared to the carrier frequency of the laser which is around 192 THz this is a very little change and if converted to wavelength it amounts to only about $0.1 - 0.2$ pm, which is not feasible to measure using a standard optical spectrum analyzer (OSA). Techniques, so-called direct detection schemes, for measuring the Doppler shift optically do exist though; e.g. making use of a sharp BPF with the zero-Doppler shift placed on one of the steep flanks and thus converting the frequency shift into an intensity modulation; a reference intensity is then simultaneously measured at the zero-Doppler shift wavelength. In another scheme a Fabry-Pérot interferometer is used and the Doppler shift is found by mea-

suring the displacement of the fringes in the resulting fringe pattern [22, 23]. The demands for both these techniques regarding calibration and stability are very high, though, and a more simple technique to use is that of heterodyne or coherent detection. In heterodyne detection two optical fields of different frequencies are combined on a PD and this results in a beat frequency equal to the frequency difference

The two optical fields are described by

$$\begin{aligned} E_s(t) &= \frac{1}{2}A_s\left[\exp\left[-i\left(\omega_s t+\phi_s\right)\right]+\exp\left[i\left(\omega_s t+\phi_s\right)\right]\right], \quad (2.2)\\ E_{LO}(t) &= \frac{1}{2}A_{LO}\left[\exp\left[-i\left(\omega_{LO} t+\phi_{LO}\right)\right]\right.\\ &\quad \left.+\exp\left[i\left(\omega_{LO} t+\phi_{LO}\right)\right]\right], \quad (2.3)\end{aligned}$$

where E_s is the signal field and E_{LO} is the reference field called LO, A is the amplitude of the fields and ϕ the phase, and $\omega = 2\pi\nu$ is the angular frequency. The current generated by the PD is proportional to the input intensity i.e.

$$\begin{aligned} I(t) &\propto \left|E_s(t)+E_{LO}(t)\right|^2 = \left[E_s(t)+E_{LO}(t)\right]\left[E_s^*(t)+E_{LO}^*(t)\right]\\ &= \frac{1}{2}A_s^2+\frac{1}{2}A_{LO}^2+\frac{1}{4}A_s^2\left[\exp\left[-i2\left(\omega_s t+\phi_s\right)\right]+\text{c.c}\right]\\ &\quad +\frac{1}{4}A_{LO}^2\left[\exp\left[-i2\left(\omega_{LO} t+\phi_{LO}\right)\right]+\text{c.c}\right]\\ &\quad +\frac{1}{2}A_s A_{LO}\left[\exp\left[-i\left(\left(\omega_s+\omega_{LO}\right)t+\left(\phi_s+\phi_{LO}\right)\right)\right]+\text{c.c}\right]\\ &\quad +\frac{1}{2}A_s A_{LO}\left[\exp\left[-i\left(\left(\omega_s-\omega_{LO}\right)t+\left(\phi_s-\phi_{LO}\right)\right)\right]+\text{c.c}\right], \quad (2.4)\end{aligned}$$

where c.c denotes the complex conjugate. No photo detector, however, is fast enough to resolve the fast oscillations of the optical fields and certainly not their sum frequencies either. These terms therefore average out to a DC term and the current is thus given as

$$I(t) \propto A_s A_{LO}\cos\left(\omega_{\text{diff}} t+\phi_{\text{diff}}\right)+\text{DC}, \quad (2.5)$$

where ω_{diff} and ϕ_{diff} are the frequency and phase differences between signal and LO. To arrive at this expression the identity $\cos\theta = \frac{e^{-i\theta}+e^{i\theta}}{2}$ has been used. If the frequency difference is small enough the spectrum can then be monitored with an electrical spectrum analyzer (ESA) or perhaps using a DFT. In lidars the LO is often created by using a small fraction of the signal before it is emitted into the atmosphere, a technique called self-heterodyne

detection, and the frequency difference is as starting point zero. Any wind induced Doppler shift is therefore seen as a peak not centered around zero hertz in the spectrum. Since the typical Doppler shift in wind speed measurements is of the order of megahertz, this is easily measured with standard semiconductor photo detectors.

There are certain constraints regarding the self-heterodyne technique, though. First of all there must be a spatial overlap between the signal and LO and secondly they should preferably be in the same polarization state as else the beat signal strength will decrease by a factor of $\cos(\theta)$ where θ is the angle between the polarization states of E_s and E_{LO} [24]. The former demand is easily met by propagating the backscattered signal and the LO through the same optical single-mode fibre (SMF) leading to the PD. The latter can be ensured either by using polarization maintaining components or by using the Fresnel reflection from the fibre end-facet as LO. This is the solution chosen for the lidar used in this project, see Fig. 2.1. The atmosphere is likely to induce little or no depolarization of the signal as many of the aerosols consist of homogeneous spherical particles which backscatter linearly polarized light into the same polarization state [14].

Noise in heterodyne detection

In heterodyne detection several terms contribute to the total noise in the measurement. Dark noise is the noise generated by the detector when no light is incident on the detector, and it depends e.g. on the temperature and the load resistance. A second term is the RIN which originates from intensity fluctuations in the laser output due to relaxation oscillations in the laser. These fluctuations are usually relatively slow for fibre lasers implying that RIN mainly contributes in the low end of the spectrum (around 1 MHz), but the spectral density power of the RIN grows with the square of the LO power. Hence, it can easily become dominating and impede the sensitivity at low frequencies and thus wind speeds. The effect of RIN can be suppressed either by use of a dual-channel balanced photo detector (BPD) or in the laser itself through an active feedback system [25]. For semiconductor lasers the RIN peak is usually located around 1 GHz and is therefore less severe for wind lidar measurements [19]. Shot noise is randomly generated electrical carriers in the PD and are in essence due to the quantum nature of the carriers. The power spectral density of the shot noise grows linearly with the LO power and it can be shown that the best possible SNR is achieved when the noise floor is dominated by shot noise. In heterodyne detection it is thus important to have a sufficiently high

LO power [26].

2.1.3 Probe length

A lidar measures the wind along the laser beam which in principle stretches infinitely. However, the measurement is weighted by the intensity distribution along the beam, and thus a spatial confinement of the measurement can be obtained by focusing the beam. Assuming a Gaussian beam, the mean heterodyne signal power as function of distance from the waist is

$$S\left(z\right) = \frac{w_0^2}{w\left(z\right)^2}, \tag{2.6}$$

where w_0 is the beam radius at the waist [15]. Along the direction of the beam the waist radius follows

$$w\left(z\right) = w_0\sqrt{1 + \left(\frac{\lambda z}{\pi w_0^2}\right)^2}, \tag{2.7}$$

where λ is the laser wavelength. Using this expression in Eq. (2.6) we arrive at

$$S\left(z\right) = \frac{1}{1 + \left(\frac{\lambda z}{\pi w_0^2}\right)^2}, \tag{2.8}$$

which is recognized as a Lorentzian with a full width at half maximum (FWHM) value of $2\frac{\pi w_0^2}{\lambda}$ equal to two Rayleigh lengths, i.e. the distance from the waist where the beam area has doubled [27, 26, 28]. This range is often referred to as the *probe length* and is used to define the spatial resolution of a CW lidar. The probe length increases with focus distance though, and as the focus becomes less tight, this limits the range, and e.g. for the lidar used in this project a focus at 200 m results in a probe length of 52 m approaching the limit of what can be accepted. The tails of the Lorentzian weighting function will, of course, stretch further than the probe length and this can become a problem in case they stretch into an object with a high backscatter coefficient, e.g. a cloud, as this can lead to range ambiguities [29].

For a pulsed lidar the pulses themselves lead to a spatial confinement of the measurement. At a given point in time, t_0, after a pulse of length T_p is emitted, the lidar will receive light which has been scattered over a range of $cT_p/2$ in space. In the heterodyne detection scheme, however, we need to sample data over a certain period, T_{sample}, and during that period the pulse will propagate further. The range contributing to the measurement thus becomes

$L = c\left(T_{\text{sample}} + T_p\right)/2$ and this is known as the range gate. However, not all points within the range gate contribute with the same weight as the very edges of L will only contribute during the time of one sampling whereas the centre will contribute for the full pulse duration. This can be described as the convolution between the sample window and the pulse, and assuming that both are rectangular and of equal length this leads to a spatial weighting function proportional to the contribution time of a given point

$$W(z) \propto T_{\text{contr.}}(z) = \begin{cases} T_p - \frac{2}{c}\left|z - g_c\right| & \text{for } z \in \text{range cell}, \\ 0 & \text{for } z \notin \text{range cell}. \end{cases} \tag{2.9}$$

This is a triangular function centered around the range cell centre g_c, and with a FWHM value of $\frac{cT_{\text{pulse}}}{2}$ [2].

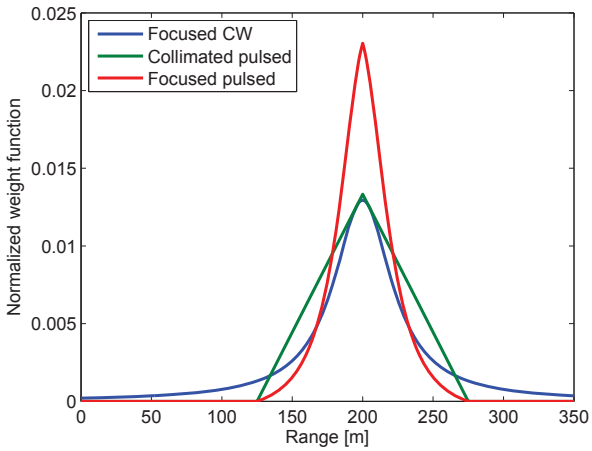

Figure 2.3: Normalized weight function for a focused CW, a collimated pulsed, and a focused pulsed lidar with the focus and the centre of the range cell set to 200 m. The confinement of the focused pulsed lidar is clearly tighter with a FWHM of 36 m compared to 52.5 m and 75 m of the other two. Also seen is how the tails of focused CW stretch from 0 m and far beyond the 350 m range plotted here.

Eq. (2.9) applies for a pulsed wind lidar with a collimated beam. If, however, a focused beam is used, the spatial confinement can be made even narrower. This is illustrated in Fig. 2.3 where the spatial weighting function of a focused CW, a collimated pulsed, and a focused pulsed lidar with the focus

and the centre of the range cell set to 200 m is shown. The focused system is based on one of the lidars used in this project (see Sec. 7.1) and is characterized by an output focal length of 28 cm, and for this range it has a probe length of 52.5 m. The pulses in this simulation are 500 ns leading to a FWHM of the spatial weight of 75 m. The confinement of the focused pulsed system is given by the product of the two weight functions and has a FWHM of 36 m. So by using a focused beam the range gate in this example has effectively been halved.

2.2 Frequency stepped pulse train modulated lidar

The frequency stepped pulse train (FSPT) modulated lidar is a hybrid lidar combining the respective advantages of conventional pulsed and CW lidar systems, i.e. inherent range gating with a high duty cycle. The concept was first presented in [30], and the first proof-of-principle given in [31], but for a hard target measurement and not a real wind speed measurement. An in-depth analysis of the expected properties of the system has been given in [2]. The FSPT is, as the name suggests, a succession of laser pulses closely spaced in time, but in the spectral domain each pulse is separated from its neighbours by a fixed frequency $\Delta\nu$. The principle is illustrated in Fig. 2.4 and a means for generating such a signal is the focus of Chapters 5 and 6. The FSPT output is thus nearly constant in time but pulsed in frequency and therefore has the potential to encompass and combine the desired features of pulsed and CW lidars when used as a lidar light source.

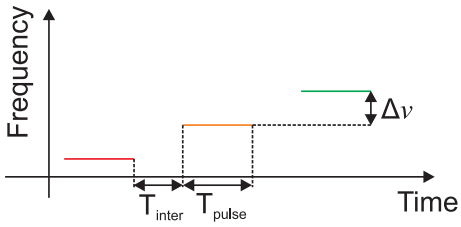

Figure 2.4: Frequency-time representation of the FSPT. T_{inter} is the time between pulses and if this is reduced the output approaches CW in time but is still pulsed in frequency.

The idea is to use the FSPT as both signal and LO in the lidar. Signal light backscattered in the atmosphere is then delayed compared to the LO by a time,

τ, corresponding to the distance, L, traveled by the signal to the place of the scatter event and back

$$\tau = \frac{2L}{c}. \tag{2.10}$$

Here c is the speed of light. In this way light scattered near the transceiver will beat against a LO pulse of the same frequency whereas light scattered farther away experiences a longer delay and the LO frequency will have changed. In the beat spectrum the frequency corresponding to zero Doppler shift therefore changes from zero hertz for signal pulses not delayed compared to the LO pulses to one $\Delta\nu$ for pulses delayed by one pulse length, and two $\Delta\nu$ for pulses delayed two pulse lengths and so on. These zero Doppler shift frequencies constitute the centres of separate frequency slots defined by the frequency step through

$$\nu_i = \left(i - \frac{3}{2}\right)\Delta\nu, \tag{2.11}$$

$$\nu_i' = \left(i - \frac{1}{2}\right)\Delta\nu, \tag{2.12}$$

where the i^{th} slot stretches from ν_i to ν_i'. Spatially each frequency slot corresponds to a specific range cell, as for the pulsed lidar, stretching from x_i to x_i'

$$x_i = \left[(i-2)\,T_p + (i-1)\,T_{\text{inter}}\right]\frac{c}{2}, \tag{2.13}$$

$$x_i' = \left[iT_p + (i-1)\,T_{\text{inter}}\right]\frac{c}{2} = x_i + cT_p, \tag{2.14}$$

where T_p is the pulse length and T_{inter} is the interpulse time during which there will be no contribution to the measurement.

The wind signal, $\nu_{wind,i}$, from the i^{th} range cell will in the beat spectrum be described by

$$\nu_{wind,i} = \nu_D\left(x_i : x_i'\right) + (i-1)\,\Delta\nu, \tag{2.15}$$

where ν_D is the wind induced Doppler shift and the last term is the centre of the frequency slot. If $\Delta\nu$ is chosen such that it exceeds the maximum induced Doppler shift, the range cells are uniquely mapped into different frequency slots and as seen from Eq. (2.15) the off-set of the zero Doppler shift frequency enables the FSPT modulated lidar to detect the sign of the Doppler shift. The off-set also means that two pulses can be placed arbitrarily close in time without this leading to range ambiguities due to two pulses contributing at

the same time in the same frequency range. The LOS wind speed is calculated from

$$v_{LOS,i} = \frac{\lambda \left[\nu_{wind,i} - (i-1)\,\Delta\nu\right]}{2}. \tag{2.16}$$

Fig. 2.5 illustrates the envisioned FSPT modulated lidar spectrum with wind spectra in first three frequency slots. Note that the first frequency slot only stretches over $\Delta\nu/2$ and the reason for this is easily found in Eqs. (2.11) and (2.12) which state that the first slot extends from $-\Delta\nu/2$ to $\Delta\nu/2$. However, it is not possible to measure negative frequencies and these are instead "wrapped around" 0 Hz. Therefore the lightwave synthesized frequency sweeper (LSFS) modulated lidar in its basic form is not capable of resolving the sign of the Doppler shift in the first frequency slot. One way to work around this would be to introduce a frequency off-set to the LO of at least $\Delta\nu/2$ as this will move the center of the frequency slot away from 0 Hz.

In addition to the sign issue the center of the first range cell will be located at the transceiver limiting the short range sensitivity (visual in Fig. 2.6(a)). This can in similar manners be remedied by introducing a time delay to the LO.

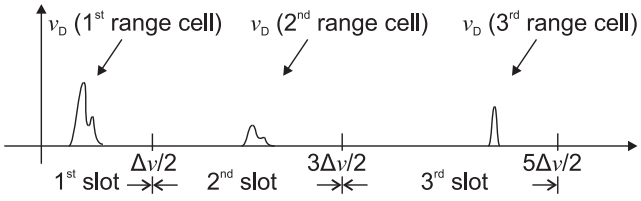

Figure 2.5: Envisioned FSPT modulated lidar spectrum with wind signals originating from three different ranges in three separate frequency slots. ν_D is the wind induced Doppler shift and $\Delta\nu$ is the constant frequency shift separating each pulse. Figure adopted from [2].

The FSPT modulated lidar is not necessarily completely immune to range ambiguities and this has to do with spatial overlapping of the range cells. As seen from Eqs. (2.13) and (2.14) this will happen if $T_p > T_{\text{inter}}$. The range cells will be weighted by the same triangular function as the conventional pulsed lidar though and this helps somewhat to separate the range cell. This situation is illustrated in Fig. 2.6(a) in the extreme case where T_{inter} is set to zero, the beam assumed to be perfectly collimated, and the pulse length is 500 ns. It is seen how one range cell actually stretches to the middle of the

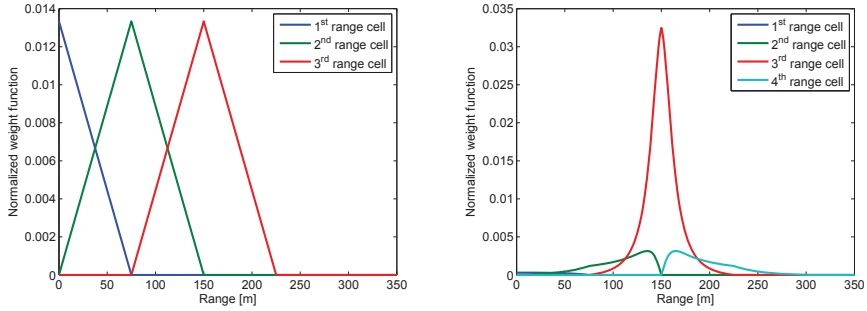

(a) (b)

Figure 2.6: (a) Normalized weighting functions of the first three range cells in the extreme case of a collimated FSPT modulated lidar with $T_p = 500$ ns and $T_{\text{inter}} = 0$ s. (b) Normalized weighting functions of the first four range cells of a focused FSPT modulated lidar. The focus is in the middle of the third range cell at 150 m.

neighbouring cell, but due to the triangular weighting, the overlap becomes less severe. Of course, the spatial confinement of given range cell can be increased by the use of a focused beam and this is illustrated in Fig. 2.6(b) where the focus is in the middle of the third range cell at 150 m. It is clearly seen how the focus narrows the range cell, but also how this comes at the expense of the other range cells which are heavily attenuated, and that the range ambiguity is by no means overcome.

For generating an FSPT modulated signal a configuration based on fibre optical components called the LSFS is suggested. This configuration will be the focus of Chapters 5 and 6.

2.3 Summary

In this chapter a brief introduction to wind lidars in general has been given explaining the difference between focused and range gated systems. They can both be used to obtain a spatial confinement of the measurement, but leading to different spatial weighting functions. The requirements put on the laser in order to operate as light source in a lidar source are explained and the heterodyne detection process described.

Finally the FSPT modulated lidar is introduced as a hybrid between conventional CW and pulsed lidars. The FSPT modulated lidar is expected to be

able to combine the inherent range gating of the pulsed system with the high duty cycle of the CW lidar.

CHAPTER 3

Blade-mounted lidar system

Lidars have since 2003 [32] been mounted on wind turbines a number of times, e.g. in [33] with the aim of optimizing the power output and as a nice side effect to reduce loads and thereby maximizing the expected lifetime of the turbine [16]. In these implementations the lidar is used to measure the wind far, perhaps 200 m, from the turbine in order e.g. to correct the yaw in case the wind changes. Another important parameter to optimize for the turbine would be the blade pitch i.e. the angle between the blade and the effective wind flow, and one can imagine a system operating in real-time optimizing the pitch control based on information of wind approaching the turbine. The wind, however, can change on time and length scales of seconds and meters e.g. due to turbulence and it is therefore necessary to measure it close to the blade, and for such a task a continuous wave (CW) lidar seems ideal with its short focus range and fast data acquisition

One can envisage different implementations of a blade-integrated lidar with different advantages and disadvantages; including one with the lidar staring horizontally into the wind and one staring along the chord of the blade. Here we will focus on the latter and Fig. 3.1 shows a sketch of this together with the two velocity components v_{blade} and v_{wind} which the line-of-sight (LOS) speed is a sum of. The speed measured by the lidar in this scenario as function of blade rotation angle, ϕ, is

$$v_{\mathrm{meas}}(\phi) = \sqrt{v_{\mathrm{blade}}^2 + v_{\mathrm{wind}}(\phi)^2} \cdot \cos(\beta - \theta), \tag{3.1}$$

where $(\beta - \theta)$ is the pitch error, i.e. the difference between the optimum pitch angle, β, and the actual pitch angle θ. The square root represents the length of the resulting wind vector and note that only if the lidar is aligned with the

wind vector the cosine becomes 1. This implies that the pitch error can be minimized by maximizing the measured lidar speed.

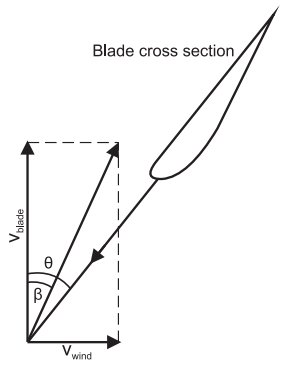

Figure 3.1: Sketch of a possible scenario with the lidar staring along the chord of the turbine blade.

3.1 Risk analysis

In this section examine some of the areas which pose possible technical risks for a blade-mounted lidar system and thus need to be evaluated before possibly proceeding with an actual implementation of a blade-mounted lidar. These risks are

- Reflections from the ground potentially leading to false signals and saturation of the system
- Misalignment between the receiver optics and the signal due to movement of the receiver which will lead to reduced sensitivity
- Spectral broadening of the signals due to movement of the receiver. Also this results in reduced sensitivity

3.1.1 Ground returns

Unless the staring direction of the lidar is perfectly aligned with the rotational axis of the turbine the lidar will at some time during a turbine revolution stare directly into the ground. Reflections from the ground, or *ground returns*

can potentially lead to false peaks in the measured spectra and, if the reflections are strong, even saturate the lidar with a loss of data as a consequence. Obviously ground returns depend on the focus length of the system, the staring angle with respect to the ground, and the reflection coefficient of the ground. It is the scope of this section to assess the potential risk that ground returns pose on the measured wind speed.

In a lidar measurement the received signal power depends, among other things, on the area of the laser beam and the backscatter coefficient, $\beta(\pi)$, of the scattering object so that

$$P_s \propto \frac{\beta(\pi)}{A_{\text{beam}}} \tag{3.2}$$

The beam $1/e^2$ radius of a Gaussian beam is calculated using

$$w(z) = w_0(\xi)\sqrt{1+\left(\frac{\lambda z}{\pi w_0(\xi)^2}\right)^2} = \sqrt{w_0(\xi)^2+\left(\frac{\lambda z}{\pi w_0(\xi)}\right)^2}, \tag{3.3}$$

where the beam radius at the waist $w_0(\xi)$ is a function of distance from the lens ξ, λ is the laser wavelength, and z is the distance from the waist along the beam [28].
The radius at the beam waist as function of distance, ξ, from the focusing lens can found by solving Eq. (3.3)

$$w_0(\xi) = \sqrt{\frac{w(0)^2 - \sqrt{w(0)^4 - 4\left(\frac{\lambda\xi}{\pi}\right)^2}}{2}}, \tag{3.4}$$

where $w(0)$ is the radius at the telescope lens.

The backscatter coefficient of the ground of course depends on a variety of factors and is in general unknown. However, to give an estimate of how severe the expected ground returns will be we can compare against a situation of an unfocused lidar staring into a wall at short range. This somewhat unorthodox construction does in fact arise in the laboratory when working with lidars and is known not to cause any problems regarding saturation. We assume that the backscatter coefficient of the ground is the same as that of the wall ($\rho_g = \rho_w$) and using the fact that the ratio of the beam areas must equal the inverse ratio of the SNRs

$$\frac{A_g}{A_w} = \frac{SNR_g}{SNR_w}. \tag{3.5}$$

The size of the aperture of the blade-mounted lidar is expected to be smaller than that of a standard ZephIR and must be taken into account when calculating

the beam areas. For the wall test we can use (using the $1/e^2$ width at the lens as the beam diameter)

$$A_w = \pi R_{\text{core}}^2 \left(1 + \left(\frac{\lambda f_w}{\pi R_{\text{core}}^2}\right)^2\right), \tag{3.6}$$

where R_{core} is the fibre core radius and f_w is the focal point of the lidar, and it has been assumed that the delivery fibre end-facet acts as the waist of a focused Gaussian beam. For the blade-mounted system we calculate the distance, D_f, from the fibre to the focusing lens to achieve the desired focus length, ξ, using the so-called thin-lens equation [34]

$$D_{fl} = \frac{f_{bm} \cdot \xi}{f_{bm} - \xi}, \tag{3.7}$$

where f_{bm} is the focal point and the beam diameter at the lens can then be found as

$$w_l(\xi) = R_{\text{core}} \sqrt{1 + \left(\frac{\lambda D_{fl}}{\pi R_{\text{core}}^2}\right)^2}. \tag{3.8}$$

The radius at the waist is

$$w_{0,g}(\xi) = \sqrt{\frac{w_l^2 - \sqrt{w_l^4 - 4\left(\frac{\lambda\xi}{\pi}\right)^2}}{2}}, \tag{3.9}$$

and finally the beam area at the ground can be found as

$$A_g(\xi) = \pi w_{0,g}(\xi)^2 + \pi \left(\frac{\lambda \cdot (D_g - \xi)}{\pi w_{0,g}(\xi)}\right)^2. \tag{3.10}$$

Notice that at long focus ranges the thin-lens equation is no longer valid. However, in this case where the blade-mounted lidar is expected to operate with a short focus distance of around $5 - 20$ m the thin-lens equation is appropriate.

Staring direction

With a lidar mounted on the turbine blade in such a way that it stares in the direction of the blade pitch we can calculate the distance from the transceiver to the ground, D_g, and hence also the ground returns as function of blade rotation angle (see Fig. 3.2).

$$D(\phi) = h + R\cos\phi \tag{3.11}$$

$$D_{gr}(\phi) = \frac{D(\phi)}{\sin\phi}, \tag{3.12}$$

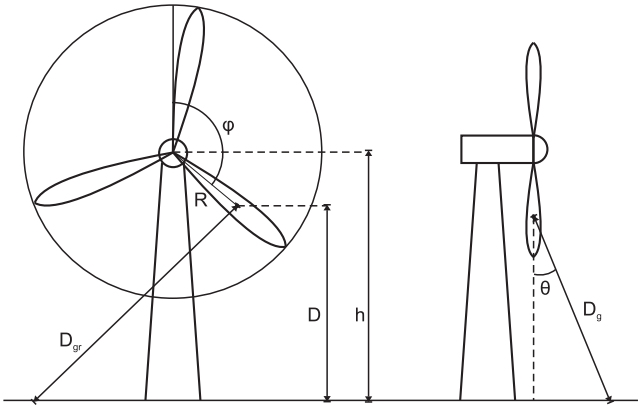

Figure 3.2: Sketch of a wind turbine with a lidar mounted on the blade and how it sometimes stares into the ground.

where D_{gr} is the distance from the transceiver to the ground in the rotor plane. Taking the pitch angle into consideration the distance to the ground along the staring direction becomes

$$D_g\left(\phi,\theta\right)=\frac{D_{gr}\left(\phi\right)}{\cos\theta}. \tag{3.13}$$

We can now use Eqs. (3.6) and (3.10) to calculate the respective areas and and plot their ratio as function of rotation angle.

Fig. 3.3 shows the ratio of the areas as the distance from the transceiver to the ground, D_g, as function of rotation angle and for three different pitch angles. For the calculations the following parameters have been used

- $h = 57$ m
- $R = 30$ m
- Focus$= 5$ m

For rotation angles higher than $180°$ D_g the lidar effectively points upwards and the distance consequently goes toward infinity and A_g/A_w to zero. The D_g has a minimum at around $120°$ resulting in a maximum SNR ratio of around 0.05. Even though one can easily imagine situations with higher reflection coefficients or a smaller the beam area at the ground, it is fair to conclude that ground returns are unlikely to cause saturation of the lidar and thereby loss of valuable data.

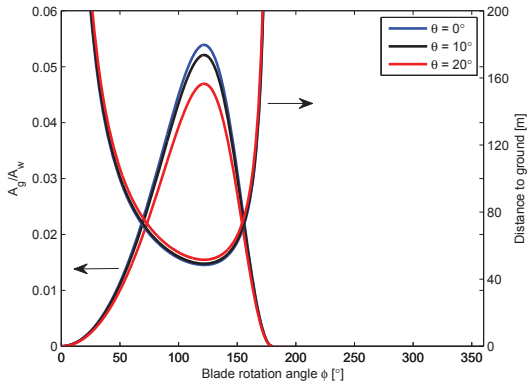

Figure 3.3: Ground return SNR and distance from the transceiver to the ground in the lidar staring direction as function of turbine rotation angle for three different pitch angles.

The second concern regarding ground returns was the possibility of false peaks in the measured spectra. Obviously these will only appear when the lidar stares into the ground as shown above and the relative speed of the ground measured by the lidar is

$$v_g = v_{\text{blade}} \cdot \cos\theta, \tag{3.14}$$

v_{blade} is the speed of the turbine blade in the rotor plane and θ is the angle between the staring direction and the motion of the lidar, hence v_g is the speed of the relative motion along the LOS. This is the minimum speed a blade-mounted lidar will measure when assuming constant turbine rotational speed and pitch angle, since it is the same as would be measured in a case of no wind but with the turbine still rotating. This is because in both cases only the lidar is moving and the fact that the scattering event in the two cases takes place at different distances from the telescope does not change the speed measured.

3.1.2 Lag angle

As the transceiver unit of the lidar is moving there is a potential risk that by the time a photon returns after a scattering event the transceiver has moved so far that it can no longer receive the photon. By using the concept of a back propagating local oscillator (BPLO) we can solve the problem by calculating how far, not the transceiver itself, but the focus point moves during the time-

of-flight (TOF) from the transceiver to the focus and back [15]. The BPLO is defined as the spatial mode into which light must scatter in order to be collected by the transceiver and contribute in the heterodyne beating process. The displacement depends on the focus distance of the lidar and the speed of the transceiver. The TOF for light going from the focus to the receiver and back is

$$t_{TOF}(\xi) = 2\frac{\xi}{c}, \tag{3.15}$$

where c is the speed of light. During one TOF the focus will move and assuming that the beam is parallel to the axis of rotation of the turbine and that during the short time span of t_{TOF} the movement can be approximated by a linear function

$$d_{TOF}(\xi) = v_{\text{beam}} \cdot t_{TOF}(\xi) \tag{3.16}$$

According to [15] the signal power, S, of a lidar signal is proportional to the overlap between the transmitted beam and the BPLO

$$S \propto \iiint\limits_{\text{all space}} \beta(\pi)\, I_T(x,y,z)\, I_{BPLO}(x,y,z)\ \mathrm{d}x\mathrm{d}z\mathrm{d}z, \tag{3.17}$$

where β is the backscatter coefficient and I_T and I_{BPLO} is the intensity of the transmitted beam and the BPLO, respectively. Restricting ourselves only to look at the focus plane of the beam Eq. (3.17) reduces to

$$S \propto \iint\limits_{-\infty}^{\infty} \rho(\pi)\, I_T(x,y)\, I_{BPLO}(x,y)\ \mathrm{d}x\mathrm{d}z, \tag{3.18}$$

$I_T(x,y)$ and $I_{BPLO}(x,y)$ are both 2D Gaussians and assuming $\rho(\pi)$ to be constant the double integral can be solved analytically to give

$$S(\xi) \propto \rho(\pi)\, I_T I_{BPLO} \frac{\pi}{\sqrt{2}} w_0^2 \exp\left[-\frac{d(\xi)^2}{2w_0^2}\right], \tag{3.19}$$

where I_T and I_{BPLO} are the centre intensities which can be calculated using Eq. (3.4), w is the width of the intensity profiles and d is the displacement between the transmitted beam and the BPLO. It is seen that the signal power as function of the displacement is itself a Gaussian.

Assuming the transceiver is mounted on the turbine wing 30 m from the centre of rotation and the time for a full rotation is 3 s the decrease in signal strength due the movement of the transceiver can be calculated from Eq.

(3.19). Fig. 3.4 shows the resulting signal strength compared to a perfect overlap between the transmitted beam and the BPLO ($S(\xi)/S(0)$), and it is seen that for the given parameters the loss in signal strength is minuscule. Even with a focus length of 1 m and a resulting very tight focus the loss is less than 0.01%

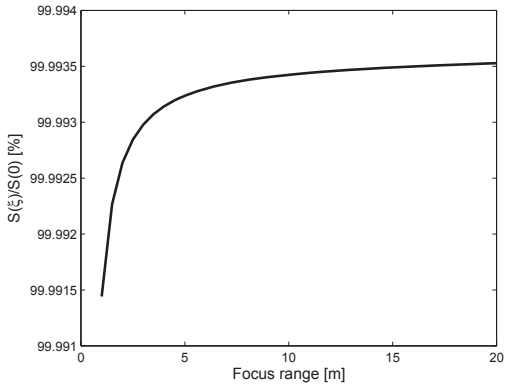

Figure 3.4: Relative signal power versus focus range.

3.1.3 Speckle bandwidth

Scanning the lidar beam through the atmosphere or staring at an angle compared to the direction of the wind flow will lead to a motion of the scattering particles across the beam, and this will in turn lead to spectral broadening of the signal even if the flow it self is perfectly homogeneous. This is essentially caused by the time a scattering particle is illuminated by the lidar beam effectively being decreased by the motion of the particle. In the measured spectrum the spectral width of the signal is inversely proportional to the time it takes to sweep through the beam waist diameter [35].
The cross-section of the beam in the focus point of the beam can be described by a centered Gaussian

$$I(x) = I_0 \exp\left[-\left(\frac{x}{w_0}\right)^2\right], \tag{3.20}$$

where I_0 is the centre intensity and w_0 is the beam waist radius ($1/e^2$-width). The time for the beam to sweep through the beam waist is

$$\tau(\xi) = \frac{w_0(\xi)}{v_{\text{beam}}}, \tag{3.21}$$

where v_{beam} is the sweeping speed of the beam. Assuming the speed is constant the current, and thus the voltage, generated by the detector, will also be a Gaussian as function of time. However, in the heterodyne detection it is the electric field of the light, and not the intensity, which is converted into a voltage, hence the detected Gaussian is a factor of $\sqrt{2}$ wider than $w_0(\xi)$

$$V(t,\xi) = \sqrt{I_0}\exp\left[-\left(\frac{t}{\sqrt{2}\tau(\xi)}\right)^2\right] = \sqrt{I_0}\exp\left[-\left(\frac{v_{\text{beam}}\cdot t}{\sqrt{2}w_0(\xi)}\right)^2\right]. \tag{3.22}$$

In frequency the detector output becomes

$$V(\nu,\xi) = \sqrt{2\pi I_0}\frac{w_0(\xi)}{v_{\text{beam}}}\exp\left[-\left(\frac{\sqrt{2}\pi w_0(\xi)}{v_{\text{beam}}}\nu\right)^2\right], \tag{3.23}$$

and hence the $1/e^2$-width (half width) is

$$\Gamma = \frac{v_{\text{beam}}}{\pi w_0(\xi)}, \tag{3.24}$$

and the full spectral width thus becomes

$$\Delta\nu = 2\Gamma = \frac{2v_{\text{beam}}}{\pi w_0(\xi)}. \tag{3.25}$$

Notice that this analysis assumes a large number of individual scatterers; an assumption which possibly breaks down in the case of a very tight focus and small probe volume or a very clean atmosphere [36].

The sweep time is minimized and thus the sweep speed maximized if the sweep direction is perpendicular to the staring direction, i.e. if the lidar is staring straight ahead from the turbine. In that situation the sweep speed is

$$v_{\text{beam}} = \frac{2\pi\cdot D_{\text{trans}}}{t_{\text{rot}}}, \tag{3.26}$$

where D_{trans} is the distance from the transceiver to the centre of rotation and t_{rot} is the time for one turbine rotation. The resulting speckle bandwidth as function of focus range is shown in Fig. 3.5 and it is seen that it rapidly drops. For a focus range of 6 m the bandwidth is 184.1 kHz which is less than the bin width in spectra. Hence, for ranges longer than 6 m spectral broadening is not expected to be a problem.

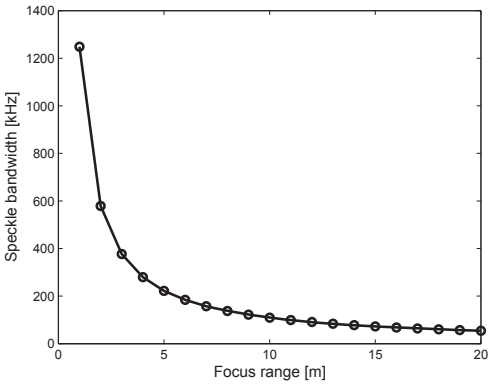

Figure 3.5: Speckle bandwidth as function of focus range.

3.2 Extended circulator port

Usually in a lidar system the distance from the laser to the telescope is short since this reduces propagation losses and non-linear effects such as stimulated Brillouin scattering (SBS). In the envisioned blade mounted lidar system, however, the laser and data processing unit will be placed in the nacelle of the turbine and light will be transmitted to the telescope through optical fibres, and it is thus important to consider the different implications of this and one of these is the placement of the circulator compared to the telescope.

It might be tempting to place the circulator which directs light from the laser to the telescope and from the telescope to the detector near the laser and extend the delivery fibre so it reaches all the way from the nacelle to the telescope. The alternative is to extend the fibres leading from the laser to the circulator and from the circulator to the detector, but this requires twice as much fibre. In the ideal case a lidar spectrum will consist only of the beating between the local oscillator (LO) and the Doppler shifted wind signal with the noise floor dominated by the LO shot noise. However, in reality noise originating from different sources will be present, and among these noise due to cross-talk in the circulator. Light leaking directly from port 1 into port 3 will interfere with the LO (neglecting the wind signal) giving rise to excess noise. If the difference in distance traveled by the cross-talk and the LO is small chances are that the two contributions will still be in phase adding only to the noise near the difference frequency (0 Hz for a CW lidar), but as the path

difference grows the cross-talk and LO will get more and more out of phase and the noise grows.

The detected beat spectrum can be described as a sum of a coherent, S_C, and an incoherent, S_I contribution

$$S(\omega) = S_C(\omega) + S_I(\omega), \tag{3.27}$$

where

$$S_C(\omega) = aI_1I_2 \exp\left[-\frac{\tau_d}{\tau_c}\right] \delta(\omega), \tag{3.28}$$

and

$$S_I(\omega) = \frac{aI_1I_2\tau_c/\pi}{1+\omega^2\tau_c^2}\left[1 - \left(\cos(\omega\tau_d) + \frac{\sin(\omega\tau_d)}{\omega\tau_c}\right)\exp\left(-\frac{\tau_d}{\tau_c}\right)\right], \tag{3.29}$$

[21]. Here a is an instrumental factor, I is the intensity of the two contributions, τ_c is the coherence time of the laser, τ_d is the time delay of the LO compared to the cross-talk part (representing the path difference) and ω is the frequency difference. From Eqs. (3.28) and (3.29) it is seen that when $\tau_d \ll \tau_c$ the coherent contribution dominates, but as the delay grows so does the incoherent contribution eventually dominating.

It can be shown that in the low frequency limit the incoherent noise grows approximately quadratically with delay length

$$S_I(\omega) \propto \frac{\tau_d^2}{\tau_c}\left(\frac{\tau_c - \tau_d}{2\tau_c}\right) \approx \frac{\tau_d^2}{\tau_c}. \tag{3.30}$$

To mimic a real lidar system the setup shown in Fig. 3.6 has been used. The arm on circulator port 2, which would normally lead to the telescope, is gradually increased using 1 m and 5 m fibre patch chords. To ensure the same power level on the detector for all measurements an inline powermeter is used while the power can adjusted using the laser to compensate for the increase in loss due to longer fibre and/or more uniters. As LO the Fresnel reflection from the end facet of a fibre polished in an angle of 4 degrees is used. For the "0 m delay" the circulator is simply bypassed connecting the laser directly to the inline powermeter.

The measurements presented are difficult to carry out with high accuracy. Especially for long delay lines the noise level tends to fluctuate a lot as the beating varies between constructive and destructive interference. This is due to external influences such as vibrations or temperature variations changing the phase of the light. It has therefore been attempted to capture the maximum

value of the noise for every measurement. This can be done by first heating part of the fibre on port 2 by holding it in the hand and then carefully place it on the table. As the temperature of the heated part tends toward the surrounding temperature again the noise will fluctuate between the maximum and minimum values with a period of a few seconds making it possible to do the measurement at or very near the peak value.

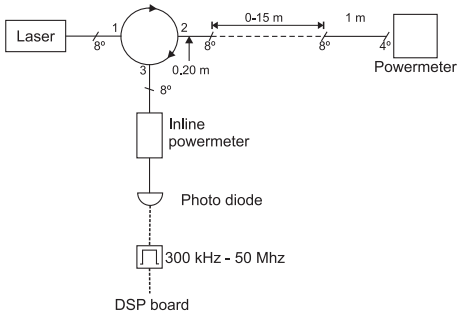

Figure 3.6: Block diagram of the experimental setup for measuring the noise due to cross-talk in the circulator.

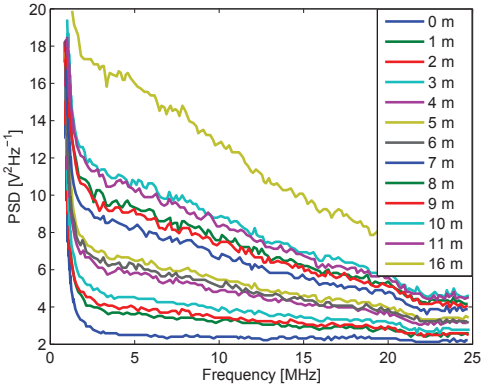

Figure 3.7: Raw spectra of the excess noise due to different extensions of the circulator port.

Fig. 3.7 shows the measured spectra for the different extension lengths used and it is clearly seen how the noise grows as the port 2 is extended. The excess noise due to the extended fibre is calculated as the difference between

the respective delay spectrum and the 0 m delay spectrum. In Fig. 3.8 the excess noise is plotted as function of fibre extension length for four different frequencies (5 MHz, 10 MHz, 15 MHz, and 20 MHz). Eq. (3.29) has been fitted to the excess noise with a and τ_c as the free parameters and the results are also plotted in Figure 3.8. The green curves represent the the best fit to the individual data series, whereas the red curves represent a mean of the values of a and τ_c found for the four frequencies. This is done because a and τ_c are actually constants and should not change with the frequency. In general the fits are too low for short extension lengths and too high for long lengths and during the work several pairs of the fitting parameters (a and τ_c) were found all giving approximately the same quality of fit. The mean values of the fitted parameters are $a = 0.0475 \ \frac{\mathrm{V^2 m^4}}{\mathrm{W^2 s^2}}$ and $\tau_c = 5.00 \cdot 10^{-5}$ s. A possible explanation for the poor fits other than the challenges which lie in the measurement could be the procedure for extending the fibre. When extending the fibre standard fibre optical uniters are used, and it must be expected that they will add to the phase noise due to the interface introduced between the two fibres.

The results presented here represent measurements which are difficult to carry out with high accuracy because the experimental setup is in essence an interferometer which is extremely sensitive to external influences such as vibrations or changes in temperature which leads to large variations in the excess noise as function of time. Nevertheless they all show a clear increase in the noise level with increasing delay length, and they all support the important conclusion that circulator port 2 should be kept as short as possible in order to keep noise floor low and dominated by shot noise.

3.3 Summary

Lidars mounted in the wings of wind turbines for control of the pitch angle have the potential of increasing the efficiency and at the same time reduce loads on the turbine. A theoretical study examining the possibility of such a system seen from a lidar perspective has been carried out. The effect of various phenomena such as ground returns, lag angle, and speckle bandwidth on the performance of the lidar has been investigated and it is found that all three are expected to have negligible impact. Finally the influence of light leaking from the input port on the circulator directly to the output port as the fibre connected to port 2 is extended, has been investigated, and it is concluded that the delivery fibre must be kept as short as possible.

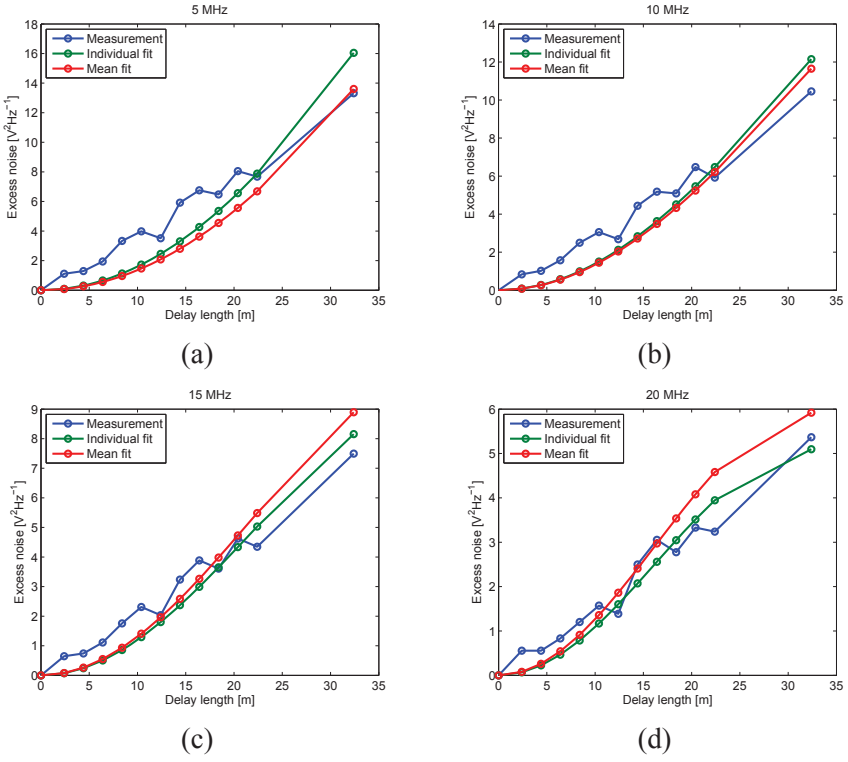

Figure 3.8: Excess noise as function of delay length for four different frequencies 5, 10, 15 and 20 MHz. Shown is also fit of Eq. (3.29) to the measured data. Note that the delay length is twice the extension length because the light travels back and forth.

CHAPTER 4

Wind tunnel trial

In the previous chapter it was concluded that the foreseen technical risks are not expected to hinder the feasibility of a blade-mounted lidar system. There are still issues that needs to be resolved before a lidar can be installed in a blade though, for example how will it cope with the very high wind speeds expected, and can a smaller aperture size transceiver be used in order to reduce costs? To study this a series of experiments were performed in a high performance wind tunnel with a short-range, small aperture lidar and covering a wide range of wind speeds up to 75 m/s. Furthermore, the trial is a chance to investigate the capability of the lidar to measure the wind flow within a wind tunnel in addition to fundamental phenomena such as line-of-sight (LOS) speed and speckle broadening. Experiments were carried out at different ranges and at various angles to the flow. These experiments are described in this chapter.

4.1 Experimental setup

The test setup consists of a lidar with a mobile telescope placed within a wind tunnel. During the tests the telescope is placed on a horizontally mounted crossbar in the test section of the wind tunnel, see Fig. 4.1. The lidar base unit, with photo detector and data processing unit, is placed outside the tunnel and an optical cable fed through a hole in the tunnel wall connects the two units. The crossbar can be moved up and down, and the telescope can furthermore be rotated around it allowing different angles between the laser beam and the wind flow to be tested.

Besides the lidar the wind tunnel is equipped with two different systems for measuring the wind speed, and these are both used as reference to the lidar measurements. One is a Pitot tube, which works by measuring the pressure

of the moving air compared to stationary air [4], located in the middle of the test section (see Fig. 4.1), and another is a system of pressure sensors at the walls of the tunnel (henceforth referred to as 'System'). Both the Pitot tube and System gather data at a rate of 5 Hz whereas the lidar samples at 50 Hz, but in the measurements reported here, the lidar was configured to average the speed over a 1 second period, and these data were reported at 1 Hz rate.

4.1.1 Wind tunnel

The wind tunnel is a closed loop with an overall dimension of 37×14 m. The test section, in which the lidar transceiver is mounted, is 7 m long with a cross-section of 1.35×2.7 m. The flow is driven by a 1 MW fan and speeds of up to 105 m/s with laminar flow can be reached [37]. If turbulent wind is needed, a metal grid can be mounted at the entrance of the test section to distort the flow.

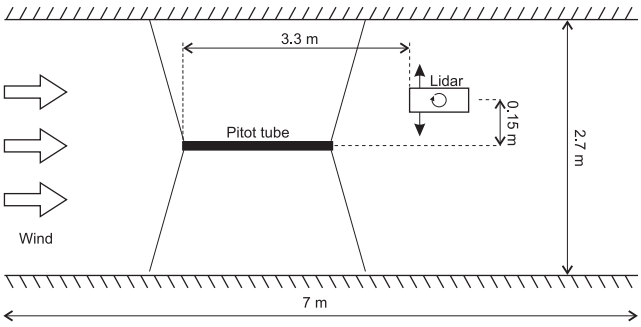

Figure 4.1: Sketch of the lidar and the Pitot tube in the wind tunnel. The lidar can be moved up and down as well as rotated around its centre to change the staring direction.

4.1.2 Lidar

The lidar used in the tests is a continuous wave (CW) Doppler lidar model *ZephIR 300* from Natural Power, but with modifications regarding the transceiver unit and the electrical filtering. These modifications have been made because the tight confinements in the tunnel requires a very short focus length of the beam, and the potentially very high wind speeds in the tunnel exceed the speeds the lidar was built to measure. The transceiver unit is a telescope with

a two inch diameter lens and manually adjustable focus. All measurements are obtained with the beam staring in a fixed direction and with fixed focus range, but with the possibility of changing these in between measurements. The telescope is connected to the lidar base unit only through a 35 m fibre optical duplex cable and can therefore easily be moved around. On the electrical side the lidar is equipped with a $300\ \mathrm{kHz} - 50\ \mathrm{MHz}$ bandpass filter which allows for the measurement of wind speeds from $0.2 - 39$ m/s. A second bandpass filter ($50 - 100$ MHz) is used to permit operation at higher speed ($39 - 78$ m/s). It is necessary to manually switch between the standard low speed configuration and the high speed configuration.

4.2 Results

In this section the wind speeds measured during the trials are presented. Comparisons between the lidar and the two reference systems are made to evaluate the performance of the lidar.

4.2.1 Initial tests - low and high speeds

The lidar used in these wind tunnel tests is capable of measuring LOS wind speeds ranging from $0 - 78.25$ m/s. However, to cover this wide span of wind speeds two different hardware (electrical) configurations are used and these are initially tested individually.

The laser beam is staring horizontally into the wind flow, as shown in Fig. 4.1, and is focused at a distance of 3.3 m, very close to the location of the pitot tube sensor, just a few centimetres above the aperture. This results in a beam waist radius of 164 μm and a probe length of 10.8 cm. The wind speed is increased from 5 m/s to 35 m/s in steps of 5 m/s. Each step is 7 minutes long, but due to the time it takes to stabilize the wind speed at the pre-set value only data representing the last 2 minutes of each step is used for further analysis. In Fig. 4.2 is shown an example of these measurements. All three systems show good agreement on the average wind speed for every step, but it is clearly seen that the Pitot tube measurements are much less stable for low wind speeds than the System and lidar measurements.

Fig. 4.3(a) shows the average of the speeds measured by the lidar over 2 minutes for each step plotted against the average speed recorded by the reference Pitot tube in the same time intervals. Since the Pitot tube samples data five times as fast as the lidar each average represents five times as many points. Shown is also a linear least squares fit to the data points (notice that the fit has

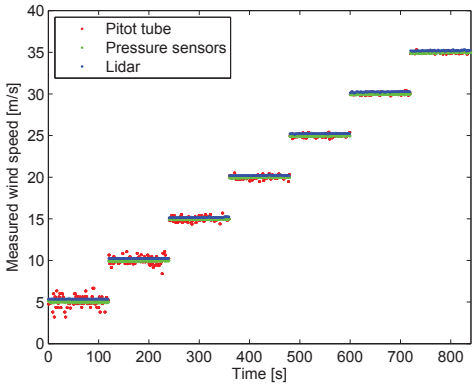

Figure 4.2: Wind speeds measured by the lidar, Pitot tube and System. Each step represents 2 minutes of data and the transition periods, during which the speed increases, have been removed.

been forced through the point $(0, 0)$). A very good correlation between the two data series is found with a slope of the fit of 1.0084 and a coefficient of determination (R-value as defined by the Matlab package *"ezfit 2.40"* [38]) of 0.9999. Thus, a disagreement between the measured wind speed of the lidar and the Pitot of 0.84% is observed with the lidar measuring a slightly higher wind speed. We also tried fitting to an affine function but with no significant difference.

Fig. 4.3(b) is the equivalent of Fig. 4.3(a) but this time with data recorded by System as the reference. Again very good agreement between the two data series is found with a slope of 1.0106 and an R-value of 0.9998.

Next, the lidar is switched to the high speed configuration and the wind speed is stepped from $40 - 75$ m/s in steps of 10 m/s except for the last step which is obviously only 5 m/s. The correlations between the measurements are again excellent with slopes of the correlation plots 1.0034 and 1.0050 and R-values of 1.0000, see Appendix A. Once again, the lidar estimates the wind speed a bit higher than the two reference systems. Based on these measurements it is concluded that the lidar has no difficulty measuring wind speeds up to 75 m/s and performs equally well in this range as in the low speed range.

Sometimes the power level returning to the lidar is too low for a trustworthy wind speed estimation and the lidar returns no wind speed. This phenomenon, which among other things depends on the backscatter coefficient of

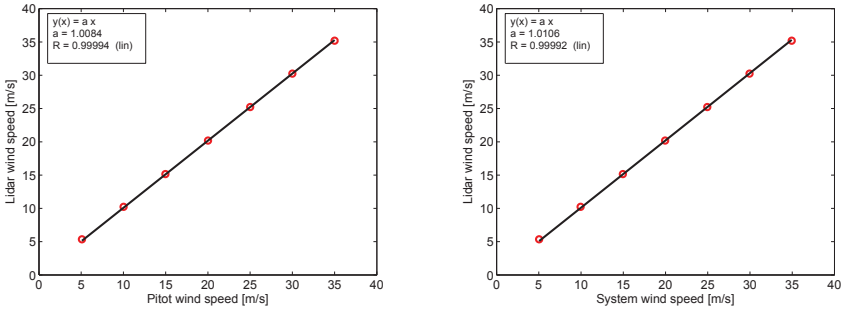

(a) (b)

Figure 4.3: Plot of the mean wind speeds in the initial low speed test measured by the lidar against the wind speeds measured by the reference Pitot tube (a) and System (b). Also shown is the fitted expression and the quality of the least squares fit expressed through the coefficient of determination R value.

the atmosphere being probed, occurred during this test, resulting in e.g. the 75 m/s average measurement consisting of only 65 points instead of the intended 120. The lidar measurements, however, appear so stable that the less than optimum number of points does not seem to impact the measured average wind speed.

4.2.2 Range of speeds

As was clearly seen in Fig. 4.2 the Pitot tube data fluctuates more than both the lidar and System data especially for low wind speeds. Therefore the population standard deviation of each data series is calculated and Fig. 4.4(a) shows the resulting standard deviations as function of wind speed for both the lidar, the Pitot tube and System and for both the low and high speed test . As expected from Fig. 4.2 the standard deviation of the Pitot tube measurement is considerably higher for 5 m/s than the lidar and Systems measurements. However, it falls with increasing wind speed and approaches the level of the lidar and System. The System standard deviation shows a similar behaviour, but at a lower level, whereas the lidar standard deviation increases slightly with the wind speed and the curve is less smooth.

As can be seen from the plot of the standard deviation in Fig. 4.4(a) the three measurement systems do not measure a constant wind speed all the time even in supposedly stable conditions. An example of this is shown Fig. 4.4(b) where the measured speeds are plotted against time for the pre-set speed of

50 m/s. As expected from the standard deviation plot the Pitot tube measurement is much less stable than the others with a maximum spread of more than 0.5 m/s. The lidar measurement is more stable with a maximum spread of no more than 0.2 m/s, and System even more so with a maximum spread of about 0.1 m/s. For all three measurements a slight increase in measured speed during the two minutes of measurement of perhaps 0.1 m/s is seen suggesting that the wind tunnel is not fully stable. A tendency which is also seen at other speeds.

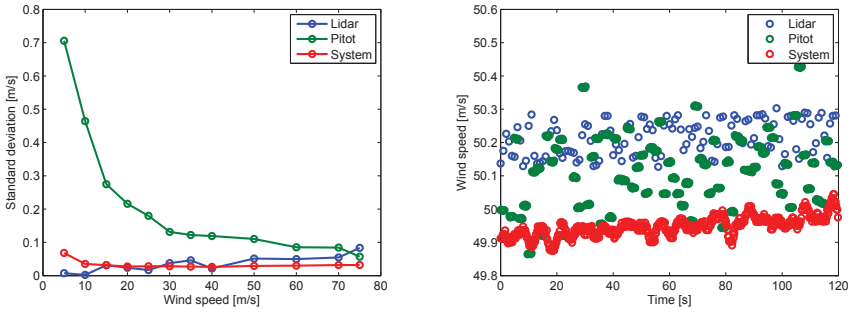

(a) (b)

Figure 4.4: (a) Standard deviation as function of pre-set wind speed. (b) Plot of the measured speeds as function of measurement time for the three reference systems. The Pitot tube measurement is clearly the most unstable, whereas System is the most stable. Most easily seen for System but also noticeable for the Pitot and lidar measurements is an increasing tendency in the measured speed with time.

Fig. 4.5(a) shows the difference between the highest and the lowest measured speed for each pre-set speed. The span in the Pitot tube measurements is seen to be high in the beginning (3.5 m/s) but it rapidly decreases and seems to tend toward a constant level of about 0.5 m/s. System also measures a large relative span at low speeds but at 15 m/s it suddenly drops and at higher speeds the span is more or less constant. The behaviour of the lidar is almost opposite. The span is low in the beginning but then at 15 m/s it increases dramatically. After that a gradual increase with wind speed is seen. A part of the explanation for the difference in behaviour could be the wind tunnel itself. The wind tunnel is known not to be fully stable for speeds lower than approximately 15 m/s [39], and because of the higher sampling rate the Pitot tube and System can perhaps better resolve the resulting instabilities. This of course does not explain the sudden increase at 15 m/s seen for the lidar.

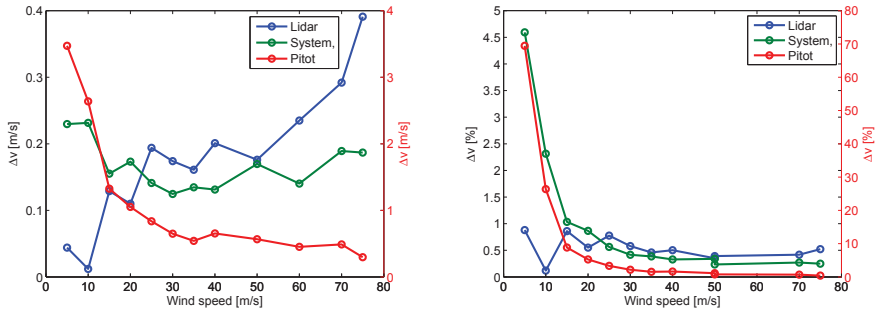

(a) (b)

Figure 4.5: Plot of the difference between highest and lowest measured wind speed at each pre-set speed in $[\mathrm{m/s}]$ (a) and relative to pre-set speed (b). Notice the two different $\Delta\nu$-scales. Lidar and System belong to the scale at the left hand side of the figure and Pitot belongs to the scale at the right.

4.3 Probe volume

When changing the focal range of the telescope the probe volume of the lidar is also altered. Shorter focus length means a tighter focus and hence a smaller probe volume and vice versa. A very small probe volume can result in a very limited number of scattering events contributing to the return signal and this affects the underlying statistics [40]. In some of the tests performed during this campaign the probe volume is so small that there is a high risk that only very few scatterers contribute to each measurement, but unfortunately a detailed analysis of this phenomenon has not been possible because of the way the lidar process the data. On the other hand, with a long probe volume the measurement is less localized. The probe volume depends on the beam waist radius and the Rayleigh range. The amount of backscattered light collected by the telescope is inversely proportional to the beam area; hence the collected light mainly originates from near the beam waist. The Rayleigh range defines the range from the waist, significantly contributing to the backscatter [15]. This is defined as the distance from the waist where the beam area has doubled and can be calculated as

$$z_R = \frac{\pi w_0^2}{\lambda}, \tag{4.1}$$

where w_0 is the beam waist radius and λ is the wavelength of the light. Since probing takes place on either side of the waist, the probe length is given as two times the Rayleigh range.

In this section the influence of the probe volume on the wind speed estimation is investigated through a comparison of measurements done using relatively long and short focal ranges.

4.3.1 Short range

In this experiment the laser beam is focused at only 1.3 m resulting in a very tight focus with a beam waist radius of approximately 65 μm and a probe length of 16.8 mm. The lidar is set for low wind speeds and the tunnel is preset to step through 10, 20 and 30 m/s. This time the lidar estimates lower wind speeds than the Pitot tube, but higher than System with slopes of the fits of 0.9979 and 1.0187, respectively. The fit is a bit worse for the Pitot tube than for System but still with a high R value of 0.9987. We therefore conclude that the lidar has no problems correctly estimating the wind speed despite the short range, resulting in a very tight focus and a reduced number of contributing scatterers.

4.3.2 Long range

Next, the focus of the beam is changed to 5.9 m which is about the longest possible while keeping the focal point within the test section of the wind tunnel. The focus now broadens significantly to a beam waist radius of 294 μm and a probe length of 34.7 cm. As a consequence, there is a possibility that part of the probe volume stretches outside the test section of the wind tunnel and into the contraction zone. The contraction zone is the section just upstream from the test section and where the flow is speeded up through a narrowing of the tunnel cross-section. Once again, we observe that the lidar estimates the wind speed a slightly lower than the Pitot tube, but slightly higher than System. The problem foreseen of the probe volume stretching out of the test section does not seem to be influencing the result. In conclusion, for the focal ranges obtainable within the wind tunnel, neither short nor long, result in erroneous measurements and either can be used without problems.

4.4 Line-of-sight speed

It is well known that the lidar only measures the wind speed in the direction of the laser beam; hence, any mismatch between the direction of the flow and the laser beam results in a decrease in the measured speed. In addition

the mismatch in directions might lead to spectral broadening of the signal, resulting in a broader but lower spectral peak seen by the lidar, increasing the risk of the peak not being detected at all. As discussed in Section 3.1.3, the broadening effect is in essence due to the fact that the particles, from which the light scatters, move across the beam and therefore spend less time in the probe volume, effectively reducing the sampling time. The spectral broadening is inversely proportional to the time it takes for the particle to pass through the beam.

In the following experiments these effects are investigated by tilting the beam a certain angle compared to the flow.

4.4.1 Low angle of attack

The telescope is again focused at 3.3 m, but this time tilted $9.2°$ downwards from horizontal, see Fig. 4.6. The wind speed is stepped from $10 - 70$ m/s in steps of 10 m/s.

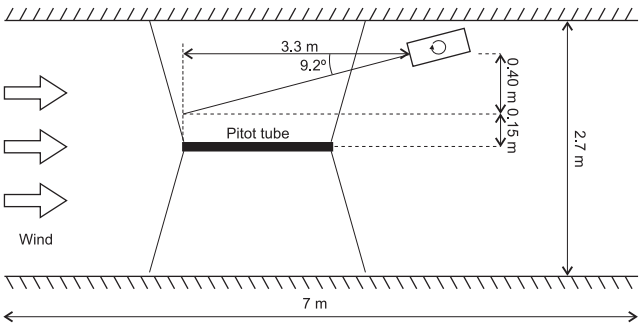

Figure 4.6: Sketch of the setup with the laser beam tilted compared to the air flow.

Figs. 4.7(a) and 4.7(b) show the correlation plots after lidar measurements have been corrected for the direction mismatch using the simple expression

$$v_{\text{flow}} = \frac{v_{\text{meas}}}{\cos\theta}, \tag{4.2}$$

where v_{flow} is the speed in the direction of the flow, v_{meas} is the speed measured by the lidar and θ is the angle between the flow and the laser beam. As can be seen from the figures it has not been possible to retrieve data from the lidar from the 40 m/s experiment because this speed is very close to the

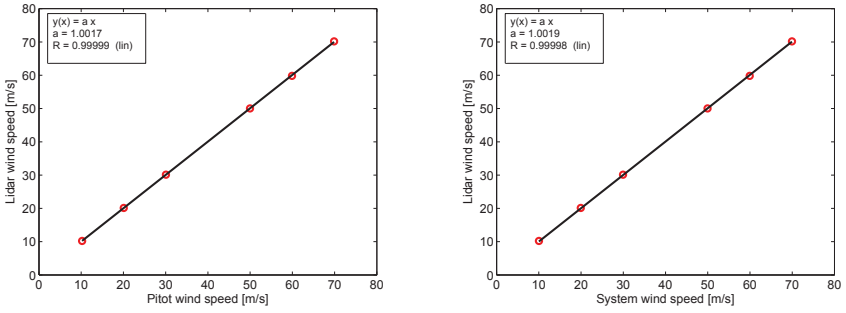

(a) (b)

Figure 4.7: Plot of the mean wind speeds in "low angle of attack test" measured by the lidar after correction for the angle of attack against the wind speeds measured by the reference Pitot tube (a) and System (b).

boundary between the low and the high speed configuration of the lidar when the direction mismatch is taken into account. Furthermore, there were again some fall outs in the lidar measurements and for example the 70 m/s average is based on only 9 data points. The correlation plots never the less are very good, once again, with extremely high R-values. Fig. 4.8 shows an example of the fall outs experienced in this test. These are the measurements taken at a wind speed of 30 m/s and the lidar graph has 75 points meaning that 45 out of 120 points are missing. The fall outs are fairly evenly distributed over the two minutes and seem not to affect on the valid data points.

There can be several reasons for the high number of fall outs and one is spectral broadening as described above. Another and perhaps more likely explanation is simply that the level of backscatter in the tunnel was low during the test due to the air being too clean and combined with a small probe volume this can lead to a considerable number of fall outs. Finally, the lidar uses a noise flattening algorithm, optimized for use in the fluctuating wind flows experienced in the real atmosphere, and frequency components not changing over a certain are regarded as noise and corrected for. Operation in the very stable flows in the tunnel therefore might have led to a reduction in sensitivity over the duration of an experiment.

4.4.2 High angle of attack

The angle of the telescope is now changed to 66.5° from horizontal, see Fig 4.9. In order to have the probe volume close to the middle of the test

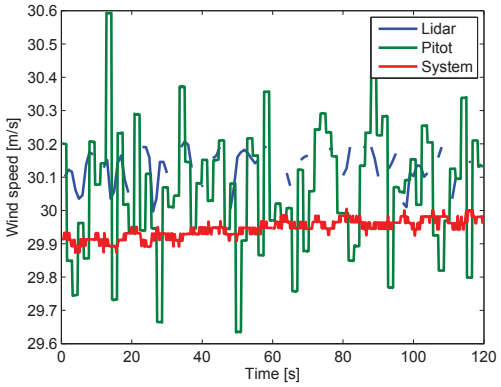

Figure 4.8: Plot of wind speed as function of time. The fall outs among the lidar measurement are clearly seen. The lidar graph consists of 75 points.

section the telescope is raised to near the top of test section while the focus range is set to 1.05 m, which results in a waist radius of 52 µm and a probe length of 1.1 cm. In Section 4.3.1 it was validated that can measure at a focus length of 1.3 m. However, with the even tighter focus used in this test the probe volume is approximately halved compared to the test presented in Sec. 4.3.1 thus testing the lidar further. The tight focus and high angle of attack should furthermore give an indication of whether spectral broadening should be a concern.

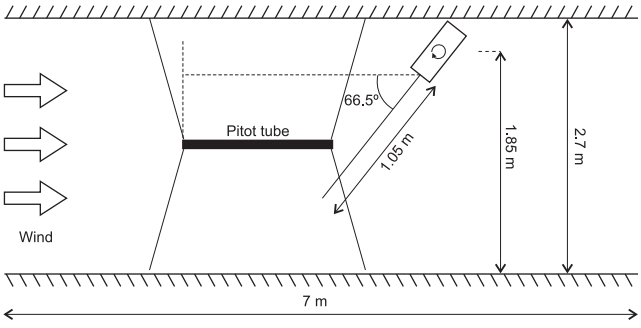

Figure 4.9: Sketch of the setup with the laser beam tilted 66.5° compared to the air flow.

Because of the high number of fall outs in the previous test the wind tunnel is this time seeded with a bit of smoke to increase the backscatter coefficient.

Fig. 4.10 shows the line-of-sight wind speed measured by the lidar. Note that the slope of the fit is very close to the numerical value of $\cos 66.5^\circ \approx 0.3987$ as expected. After correction for angle of attack according to Eq.

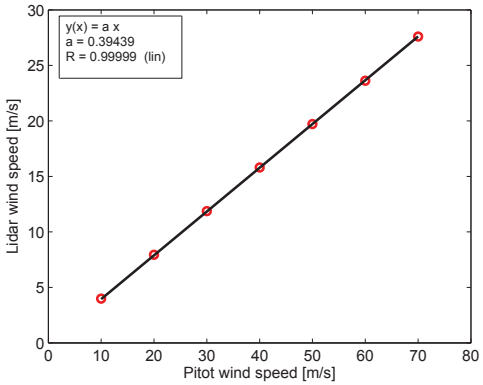

Figure 4.10: Plot of the lidar measured wind speed as function of the Pitot tube measured wind speed. The lidar is tilted 66.5° compared to the air flow and thus measured a lower speed.

(4.2) the slopes of the correlation plots are 0.99027 and 0.99016 and the R values are 1 and 0.99999 for Pitot and System, respectively.

Because the wind in this test moves across the beam any scattering particle spends less time within the probe volume and this gives rise to a broadening of the spectrum of the return signal as described in Section 3.1.3. The spectral width of the return signal is inversely proportional to the time it takes for a particle to move through the probe volume and is given as

$$\Delta\nu = \frac{2v_{\mathrm{part}}}{\pi w_0\left(\xi\right)}, \tag{4.3}$$

where v_{part} is the speed of the scattering particle in the direction perpendicular to the beam and w_0 is the waist radius. This equation is identical to Eq. (3.25), except that v_{part} is used instead of v_{beam}, since in this experiment the beam is stationary. Another issue which must be taken into account is that the beam waist is effectively increased when the scattering particles, as is the case here, do not pass straight through the beam, i.e. the direction of the particles is not

perpendicular to the beam. The field distribution through the focus at a given angle, θ, compared to the beam direction (see Fig. 4.11(a)) is

$$V(z,x) = \sqrt{I_0}\exp\left[-\frac{x^2}{2w_0^2+2\left(\frac{\lambda z}{\pi w_0}\right)^2}\right] \Leftrightarrow \tag{4.4}$$

$$V(r,\theta) = \sqrt{I_0}\exp\left[-\frac{r^2\sin^2\theta}{2w_0^2+2\left(\frac{\lambda r\cos\theta}{\pi w_0}\right)^2}\right]. \tag{4.5}$$

For small angles the cross-section is no longer Gaussian, but as seen in Fig. 4.11(b) for the value of θ used it is an excellent approximation. Using Eq. (4.5) the effective beam waist is found to be 57 µm, 5 µm larger than the transverse beam radius, and Eq. (4.3) reduces to

$$\Delta\nu = 11163\ \mathrm{m}^{-1}\cdot v_{\mathrm{part}}. \tag{4.6}$$

To get a measure of the signal spectral width as function of wind speed all

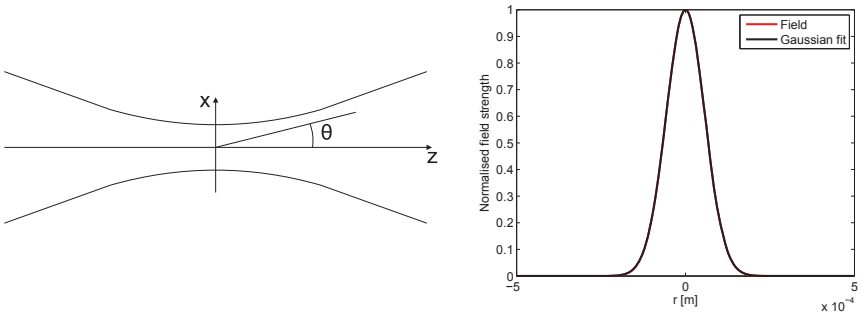

(a) (b)

Figure 4.11: (a) Sketch of a focused Gaussian beam near the waist. (b) Plot of the field distribution through the waist at an angle $\theta = 66.5°$ and a least squares fit of a Gaussian to this.

the spectra at each wind speed are ensemble averaged and to each of the resulting average spectra a Gaussian distribution with no off-set is fitted. All the individual spectra are initially processed by the internal lidar software and in this process the noise floor is removed. Therefore the fitted Gaussian has no off-set. The widths of the fitted Gaussians are plotted as function of the wind speed perpendicular to the beam in Fig. 4.12 and shown is also a linear fit to

the data points together with the theoretically predicted curve. As expected from theory the data points approximates a straight line, and the slope of the fit, 11117 m^{-1}, is in good agreement with the value predicted in Eq. (4.6). There is, however, also an offset of 220 kHz which is the equivalent of 1.13

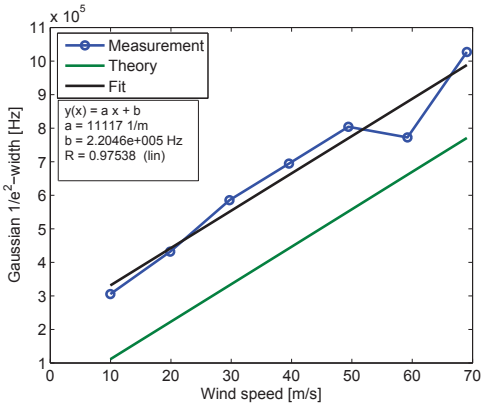

Figure 4.12: Plot of the spectral bandwidth as function of wind speed. The slope of the measured curve is very close to that of the theoretically predicted curve but there is an offset between them.

bin widths. This offset is possibly best explained by the digital sampling of the signal. Because the signal is sampled over a finite period of time the measured spectrum is in fact a convolution between the true wind spectrum and the absolute square of the Fourier transform of the window function. In this case the window function is a rectangular which has a discrete Fourier transform

$$W(\nu) = \mathfrak{F}\{w(n)\} = \frac{\sin(2\pi\nu L/2)}{\sin(2\pi\nu/2)} \exp\left[-i2\pi\nu(L-1)/2\right], \qquad (4.7)$$

where ν is the frequency and L is the length of the sampled sequence. To estimate the influence of finite sampling time on the measured bandwidths a numerical simulation has been performed as follows: First the theoretical signal bandwidth as function of wind speed is calculated using Eq. (4.3) and wind spectra are then simulated as Gaussians with widths equal to the theoretical bandwidth. These are then numerically convolved with the absolute square of the Fourier transform of the window function and finally a new Gaussian is fitted. Fig. 4.13(a) shows the width of the fitted Gaussians (*Convolution*) together with the pure spectral bandwidth (*Theoretical*) and the difference be-

tween the two (*Off-set*). As expected the convolution is wider than the theoretical bandwidth, and for low wind speeds where the spectral bandwidth is narrow it is relatively more dominant than for high wind speeds. The off-set between the two is seen to be more than 400 kHz at 10 m/s, but it decreases fast and at 30 m/s it has dropped to 253.5 kHz which is comparable to what is seen in Fig. 4.12 and at 60 m/s it is 220 kHz the same as in Fig. 4.12. Intuitively, however, one would expect the off-set to vanish as the spectral bandwidth becomes broader and dominates in the convolution and this is exactly what is seen when the convolution is calculated analytically. The convolution can be found as the Fourier transform of the product of a Gaussian and the rectangular window in the time domain which is the same as

$$\begin{aligned}
&\frac{1}{\sqrt{2\pi}} \int_{-t_0/2}^{t_0/2} \exp\left[-\left(\frac{v_{\text{part}} t}{\sqrt{2} w_0}\right)\right] \exp\left[-2\pi i \nu t\right] \mathrm{d}t = \\
&\frac{w_0}{2 v_{\text{part}}} \exp\left[-\left(\frac{\sqrt{2}\pi w_0 \nu}{v_{\text{part}}}\right)^2\right] \cdot \\
&\left[\text{Erf}\left(\frac{t_0 v_{\text{part}}^2/2 - 2i\pi w_0^2 \nu}{\sqrt{2} v_{\text{part}} w_0}\right) + \text{Erf}\left(\frac{t_0 v_{\text{part}}^2/2 + 2i\pi w_0^2 \nu}{\sqrt{2} v_{\text{part}} w_0}\right)\right]. \quad (4.8)
\end{aligned}$$

Fig. 4.13(b) shows the width of the fit to the analytically calculated convolution. The width shows the same general trend as in the numerical calculation but as expected the difference decreases with wind speed and at 60 m/s it is zero. An explanation for this disagreement between the numerical and analytical calculations has not been found.

Other possible explanations for the offset between measurements and theory seen in Fig. 4.12 include a not perfectly Gaussian beam, the potentially low number of individual scatterers due to the very tight focus, or that the flow is not totally stable as was indicated in Fig. 4.4 and an indication of this can also be found in [37]. However, these explanations have not been investigated in detail.

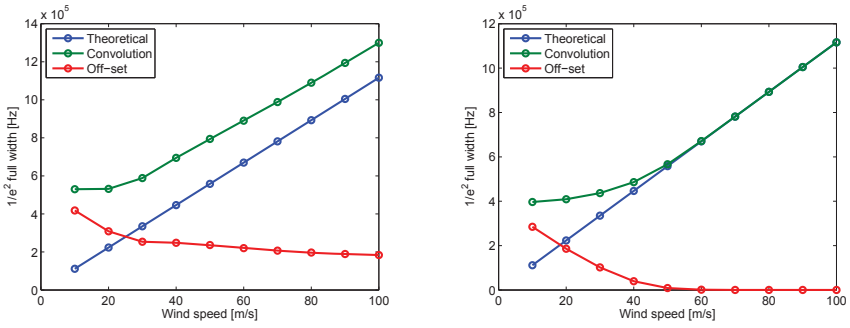

Figure 4.13: (a) Numerical calculation of the difference between the widths of the actual wind signal and the signal broadened due to windowing. (b) Analytical calculation.

4.5 Turbulent flow

In the final test the wind tunnel is fitted with a large grid to distort the wind flow and create turbulence. This will result in spectrally broader return signals.

The laser beam is returned to a horizontal position and the focus length is reset to 3.3 m. Figs. A.4(a) and A.4(b), which can be found in Appendix A, show the resulting correlation plots and again very good agreement is seen.

In Fig. 4.14 the standard deviation of each of the three data series is plotted as function of wind speed. For the Pitot a similar behaviour as in Fig. 4.4(a) is seen with a decreasing standard deviation as function of wind speed. For System the standard deviation is close to constant but with a slight increase with wind speed. The lidar standard deviation is the lowest of the three for speeds up to 40 m/s, but then a sudden increase is seen.

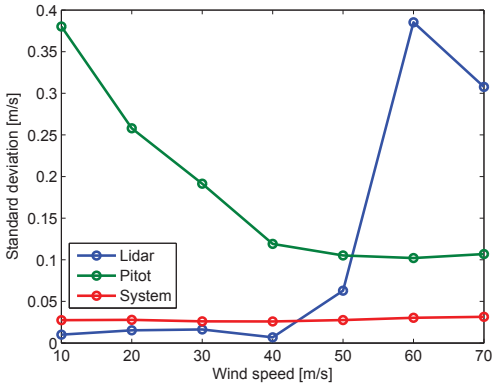

Figure 4.14: Standard deviation in measured wind speed as function of pre-set wind speed for the turbulent air flow.

More can be learned about the turbulence by studying the raw spectra of the lidar. The lidar generates 50 spectra per second and each two minute sequence of data should thus ideally contain 6000 spectra. If, however, a spectrum does not contain a valid wind signal it is discarded and thereby lowering the number of spectra. Interesting in relation to turbulence is the width of the spectra, and one way to asses this, is fitting a Gaussian to each individual spectrum and subsequently average all the resulting Gaussians. Going to the other extreme would be to first average all the spectra and then fit a Gaussian. The latter method leads to a broader spectrum as it effectively equals averaging

over longer time and thus a wider range of wind speeds are likely to occur. If the turbulence is homogeneous over the full probe volume the Lorentzian weighting function of the beam cancels out by use of the latter method and what is left is the probability density function of wind speeds in the probe volume. One can, naturally, choose a method in between the two described above e.g. by averaging ten spectra at a time and then finally average the resulting ideally 600 Gaussians. Fig. 4.15(a) shows the development in the width (standard deviation) of the spectrum when increasing the number of spectra which are averaged before fitting. The pre-set speed here is 30 m/s. As expected the width quickly increases from a value around 0.841 m/s and then tends towards a value of about 0.875 m/s when all spectra are initially averaged.

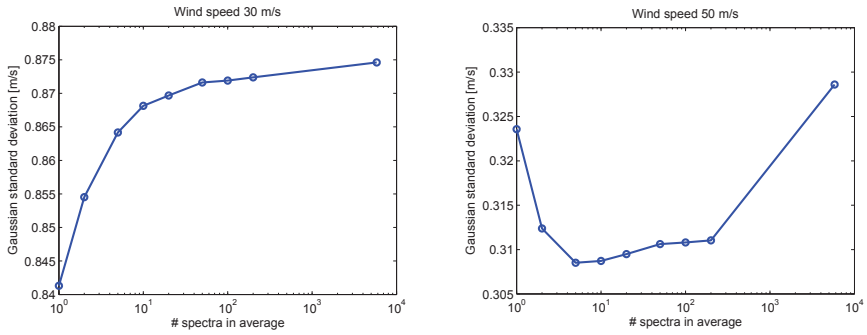

(a) (b)

Figure 4.15: Standard deviation of the fitted Gaussian as function of number spectra in the average at the pre-set speed of 30 m/s (a) and 50 m/s (b). Note the logarithmic abscissa axis in both figures.

As the wind speed increases this behaviour changes. Fig. 4.15(b) shows a similar plot, but for the pre-set speed of 50 m/s. It is first noted that the standard deviation is considerably smaller than was seen for 30 m/s, and secondly that it initially drops with the number of averaged spectra. At 5 spectra per average the width reaches a minimum and from there it slightly increases. An explanation for the narrower spectra seen at this wind speed could be found in the fact that instead of simply broaden with the increased turbulence the spectra tend to break up into several narrow spikes. Fig. 4.16(a) shows an example of this and it is clearly seen how the smaller of the two peaks is completely ignored in the fit. This tendency increases with the wind speed but can obviously be evened out if the number of spectra in the average is sufficiently high.

Fig. 4.16(b) is a plot of the width of the fitted Gaussian as function of

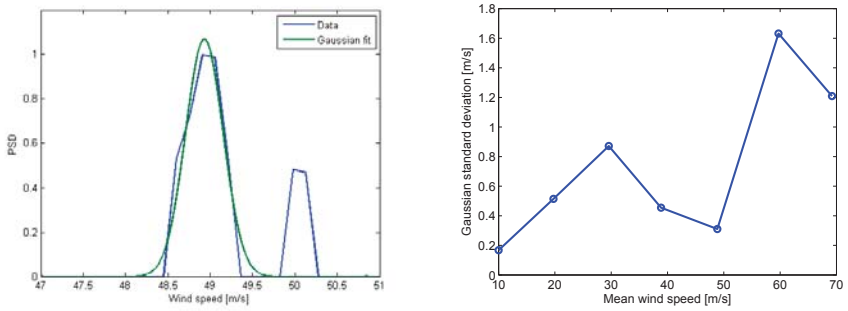

(a) (b)

Figure 4.16: (a) Example of lidar spectrum from turbulent wind flow. It is seen that the spectrum is broken into two peaks, but one of these is completely ignored by the Gaussian fit. (b) Standard deviation of the fitted Gaussian as function of mean wind speed. 100 spectra in each average.

the mean wind speed. The width grows linearly from $10 - 30$ m/s and this is expected since the turbulence increases, but then it drops before increasing dramatically in a way which to some extent looks like the behaviour seen in Fig. 4.14. The width at 60 m/s seems not far from following the linear trend seen for the lower wind speeds. Besides the break-up of the signal into several spikes as discussed above, at least two issues could influence the measured data and must be mentioned here. First, the 40 m/s wind speed is very close to the transition between the low- and high-speed configurations of the lidar. This means, as the low-speed configuration was used for the measurement, that only about half of the signal peak is present in the spectra and this complicates the fitting process. Secondly, for the speeds of 60 m/s and 70 m/s the number of valid spectra drops significantly from more than 5800 for the previous speeds to 723 and 411 respectively, hence any averaging effect becomes less pronounced. Due to the low number of spectra available for the 60 m/s and 70 m/s measurements the widths resulting from 100 spectra per average was chosen to be used in Fig. 4.16(b). This was done because as seen in Fig. 4.15(a) it has little impact on the width found for the lower wind speeds, but still gives a few fitted Gaussians to average for the high wind speeds.

4.6 Uncertainty of lidar measurements

As in all physical measurements the measurements presented in this report are subject to uncertainties, and that, of course, applies for all three measurement systems. For the lidar the following effects will contribute to the uncertainty: laser wavelength, bin width, alignment angle, and shot noise.

The LOS wind speed is calculated from the measured Doppler shift, $\Delta\nu_{\mathrm{D}}$, using

$$V_{\mathrm{LOS}} = \frac{1}{2}\Delta\nu_{\mathrm{D}}\lambda, \tag{4.9}$$

where λ is the wavelength of the laser, and any uncertainty on this will transfer to the wind speed. Another source of uncertainty is the finite resolution of the frequency axis or bin width. The frequency axis spans $0 - 50$ MHz and is divided into 256 bins, hence, each bin has a width of approximately 195.3 kHz which is the equivalent of 15.3 cm/s. In the special case of a signal occupying only one bin the speed cannot be known better than plus minus half a bin width. Shot noise is the dominant source of noise in the lidar spectrum and originates fundamentally from the fact that the light is quantized, i.e. consists of photons, and thus the number of photons reaching the detector within a certain time fluctuates. As a result the height of each bin varies from spectrum to spectrum and this affects the wind speed estimation which is based on the centroid or 'centre-of-mass' of the spectrum. The final source of uncertainty, the alignment angle, is not directly related to the lidar itself but to the physical setup of the measurement. Alignment angle refers to the uncertainty on the direction of the laser beam relative to the direction of flow. The relative uncertainty on the wind speed owing to wavelength, bin width, and alignment angle, can be calculated as

$$u_{\mathrm{rel}} = \frac{\Delta\lambda}{\lambda} + \frac{\Delta\mathrm{bin}}{\Delta\nu_{\mathrm{D}}} + \sqrt{2}\cdot\left(1 - \cos\Delta\theta\right), \tag{4.10}$$

where $\Delta\lambda$, $\Delta\mathrm{bin}$ and $\Delta\theta$ represent the uncertainty on the wavelength, half a bin width and the uncertainty on alignment angle, respectively. The factor of $\sqrt{2}$ originates from the fact that both the horizontal and the lateral direction should be taken into account when estimating the alignment angle uncertainty. Assuming that the alignment errors of the two directions are uncorrelated and of equal magnitude the relative uncertainty increases by a factor of $\sqrt{2}$.

The relative and absolute uncertainty as function of wind speed are shown

in Fig. 4.17 where it has been assumed that

$$\begin{aligned} \Delta\lambda &= \pm 1 \text{ nm} \\ \Delta\text{bin} &= 195.3 \text{ kHz} \\ \Delta\theta &= \pm 1^\circ. \end{aligned} \tag{4.11}$$

It is found that the relative uncertainty for wind speeds above 10 m/s is well

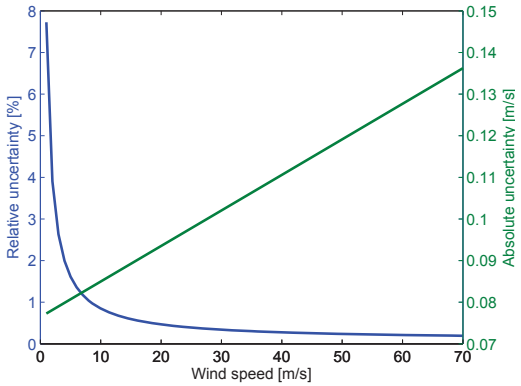

Figure 4.17: Relative and absolute uncertainty on the lidar measurement as function of wind speed.

below 1%. The absolute uncertainty is less than 14 cm/s, making the bin the dominant source of uncertainty.

The uncertainty due to shot noise further depends on the width and the height of the wind signal in the spectrum. To estimate this, the following procedure has been used: The normalised Doppler spectrum is simulated as a pure Gaussian with height h, width w, and an off-set of one. To each bin is added a noise term, representing shot noise, based on a random Gaussian distribution with a mean of one and variance as found in the measured 50 Hz spectra. A threshold equal to five standard deviations of the noise is applied, as this is comparable to the threshold applied by the *ZephIR*, and the centroid is calculated. This procedure is repeated for 10000 realizations of the noise spectrum and the standard deviation of the resulting 10000 centroids is taken as the uncertainty.

Fig. 4.18 shows an example of such a Gaussian with height 1 and FWHM of 16.5 bins and added noise. The dashed line represents the threshold. Fig.

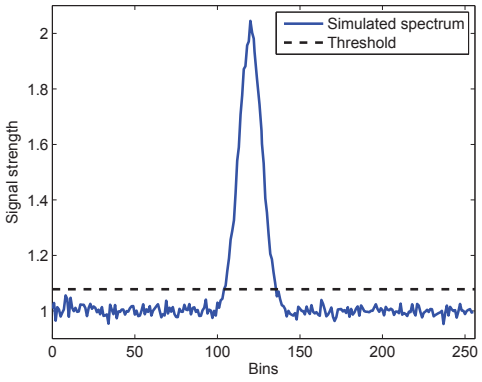

Figure 4.18: Simulated wind spectrum consisting of Gaussian with added random noise. The dashed line is the threshold of 5σ of the noise.

4.19(a) and Fig. 4.19(a) show the resulting absolute uncertainties as function of height and width of the Gaussian, respectively. As would intuitively be expected the uncertainty decreases with increasing signal strength, and only for very low signals does the uncertainty rise to around 1 cm/s. For the simulation of uncertainty as function of width of the signal a signal height of 1 has been used as this is typical for the spectra measured in this campaign. The uncertainty is seen to grow with increasing width up to around 1 cm/s for a width parameter of 10 bins equivalent of a FWHM of 16.6 bins. A width in that range may be realistic in real atmospheric conditions, but in these tests with very low turbulence a width parameter of around 1 is more realistic. For such a width, the uncertainty is found to be around 4 mm/s equivalent of 0.01% at a mean wind speed of 40 m/s. This means that the shot noise has very little impact on the total uncertainty which is well below 1% for any of the mean wind speeds used in this series of tests. Varying the height and width of the signal independently of course leads to the power in the signal not being constant, and a different approach would therefore have been to keep the area of the Gaussian constant while varying the height and width dependently.

4.7 Summary

In an experimental trial a lidar modified to meet the specifications of a blade mounted system was tested in a high performance wind tunnel. The

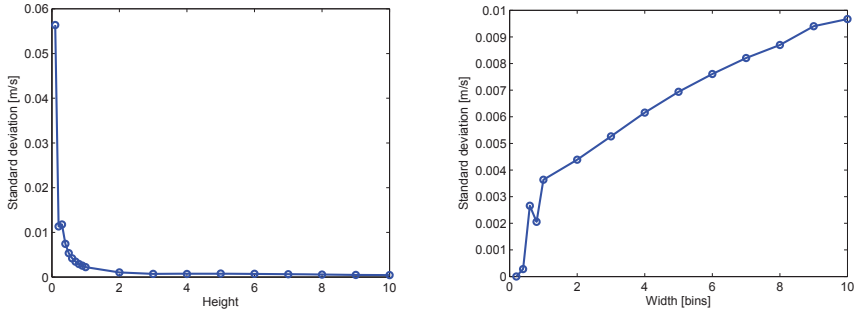

(a) (b)

Figure 4.19: Uncertainty as function of height (a) and width (b) of the simulated wind spectrum.

lidar was tested under various circumstances including very high wind speeds of up to 75 m/s and different LOS angles, and extremely high correlation with the reference systems was found in all the tests. Analysis of the uncertainties associated with the measurements suggests that the finite bin width is the main source of uncertainty. The tests supports the idea of integrating lidars in turbine wings, and furthermore suggests that short range CW lidars could have an important role to play as part of the instrumentation of wind tunnels in general.

Clearly, both the theoretical and the experimental study are only small initial steps toward a fully operational turbine integrated system, but they are nevertheless very encouraging

CHAPTER 5

Frequency stepped pulse train

Throughout the last decade there has been an increasing interest in frequency swept light sources due to their great potential within a variety of different applications including lidars. One promising version of such a light source is the lightwave synthesized frequency sweeper (LSFS) which is a fibre optical configuration that utilizes a frequency shifter inside a recirculation loop to obtain a linear frequency sweep of the consecutive laser pulses emitted. It was first described in the literature in 1990 [41] and has since been described in a number of publications covering a variety of potential applications, including wavelength division multiplexing (WDM) systems [42], medical imaging [43], chromatic dispersion measurements [44], and, of course, for use in remote sensing [30]. In the literature main emphasis has been put on minimizing the noise, maximizing the frequency sweep range and optimizing the output power stability; and through clever use of sweeping filters, polarization control, etc., sweeping ranges exceeding 1 THz and stable operation over several hours have been reported [45, 46, 47]. However, also the use of different types of optical amplifiers such as semiconductor optical amplifiers (SOAs) and Ytterbium doped fibre amplifiers (YDFAs) and their influence in the behaviour of the frequency stepped pulse train (FSPT) have been investigated [43, 48].

Most LSFSs reported in the literature operate at telecom wavelengths, i.e. around 1550 nm, and rely on an acousto-optic modulator (AOM) to shift the frequency of the light, and this with good reason. High quality optical components, including fibres, lasers, and amplifiers, at these wavelengths are readily available owing to their use within the optical communication industry. This also means that the LSFS can be realized in an all-fibre configuration, thus making the setup easy to handle and rendering tedious tasks such as alignment of mirrors superfluous. AOMs have a high extinction ratio typically in excess

of 50 dB and provide a high-precision frequency shift determined by the radio frequency (RF) frequency feeding the AOM. By the use of stable RF generators and laser sources, a spectrally very stable optical output can be obtained. The frequency shift induced by an AOM, however, is often of the order of tens or maybe a few hundreds of megahertz which is very small compared to the approximately 193 THz carrier frequency of a C-band laser. Hence, a considerable number of frequency shifts is necessary to obtain a sweep of even 1 nm. Theoretically the LSFS has successfully been described in [49] by assuming that the total power in the ring configuration is constant at all times. This model has been further developed in later publications in order to describe various changes to the basic configuration such as different signal wavelengths or sweeping bandpass filters (BPFs), while always relying on the constant power approximation [43, 45, 50]. The advantage of this model is its simplicity in that it makes cumbersome rate equations unnecessary and instead simple propagation equations, describing the development of signal and noise, coupled through the gain of the amplifier, are used. There is, however, also a drawback since any time dependencies are disregarded and therefore information on the shape of the individual pulses is lost.

In this chapter the LSFS and the resulting FSPT are described in both the temporal and spectral domain. Two different types of optical amplifiers are investigated for use in the LSFS and a model describing the output in time is presented and validated through measurements. Finally the time independent model is expanded to describe frequency noise and the model is compared against measurements. The work presented on the time dependent model and associated measurements was performed in collaboration with M.Sc.E. Anders Sig Olesen as part of his master project [51].

The work presented in this chapter has led to the publication of [52, 53].

5.1 Experimental setup

A schematic drawing of the basic LSFS is shown in Fig 5.1. The setup is an all-fibre ring configuration consisting of a 3 dB coupler, a commercial Erbium doped fibre amplifier (EDFA), a narrow BPF, an AOM (② in the figure), a delay line, and a polarization controller (PC). The ring is initially seeded by a pulse produced through modulation of the continuous output of a narrow linewidth fibre laser by an AOM (①) outside the ring. The 3 dB coupler directs half of the power of the seed pulse to the output where it is detected by a photo detector (PD), and the other half into the ring. Within the ring the EDFA is

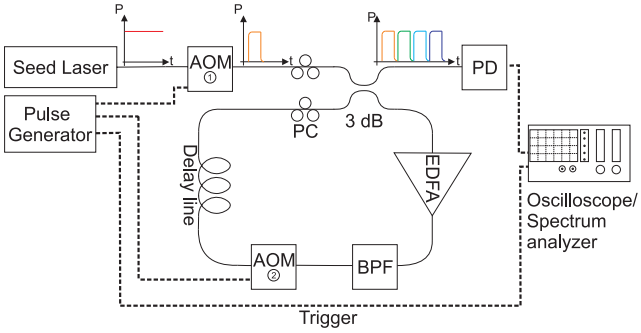

Figure 5.1: Sketch of the experimental setup of the LSFS. Optical fibres are illustrated using full lines and electrical wires using dashed lines. The inserts at the top from left to right are: CW seed laser power, initial pulse modulated by the input AOM and the resulting pulse train emitted from the LSFS. The relative frequency shift of the pulses are illustrated using different colours.

used to compensate for the transmission loss, the BPF is used for eliminating broad band amplified spontaneous emission (ASE) from the EDFA away from the signal frequency, and the AOM (2) shifts the carrier frequency of the light. The delay line, which is just a length of optical fibre, is used to adjust the length of the ring to match the desired pulse length and is chosen freely, though, in the lower limit the length is constrained by the switching time of the seed AOM. The PC is used to adjust the polarization of the light circulating in the loop. A practical way of ensuring a constant output polarization is to mount a polarization filter at the output of the ring (not shown in the figure) and use the PC to optimize the output power of every pulse. Back at the 3 dB coupler the power is again divided and one half is directed to the output whereas the other half is redirected into the ring where it is re-amplified, and the frequency is again shifted. It should be emphasized that even though seeded by a laser, the ring does not operate as a laser cavity since the frequency is shifted for each revolution.

To obtain a stable pulse train two parameters are important to optimize. First of all, the gain of the amplifier should match the loss in the ring experienced by the pulses, thereby ensuring all pulses have the same output power. This is achieved by tuning either the amplifier pump power or the filter center frequency or a combination of the two. Secondly, the pulse length should not be longer than the round trip time because pulses will then leak into each other and consequently obscure the spectrum. However, by carefully matching the

pulse length to the round trip time, an output which is nearly constant in time, and where each pulse has only one distinct signal frequency, is obtained.

What limits the operation is the build-up of ASE and the BPF in combination. The EDFA has build-in isolators ensuring uni-directional operation for both the signal and the ASE. In the forward direction, however, ASE builds up over time and deteriorates the signal to noise ratio (SNR), but as ASE is relatively broad banded, the build-up is impeded by the use of a BPF around the signal frequency. The narrower the filter the more ASE it eliminates, but the fewer frequency shifts are possible before the signal itself is attenuated. Once the noise reaches a certain level it is necessary to restart the operation. This is done by closing the AOM within the ring and thus terminating all light in the ring whereupon a new seed pulse can be generated and the entire process is repeated.

The components used in this study are all commercially available fibre connected components. As seed laser two different narrow-band CW fibre lasers from Koheras have been used. One has a wavelength of 1565 nm and the other 1548 nm, but both with a linewidth of less than 50 kHz. The amplifier is a 24 dB gain EDFA from Keopsys, and the BPF from Agiltron has a 3 dB width of 0.84 nm. The different optical fibres used as delay lines are all standard transmission single-mode fibre (SMF) from OFS Fitel Denmark. Both AOMs are from IntraAction and induce a frequency shift of 40 MHz, hence, each pulse is separated by 40 MHz from the previous pulse. It should be noted that in the practical case the AOMs put another limiting factor on the operation of the LSFS due to their finite closing time. The transmission through the AOM is reduced by 90% in 120 ns, but the time it takes to extinguish the last 10% of transmission is longer than 1 μs and the transmission in this regime falls off exponentially. In order to prevent the tail of exponential decay leaking into the following pulse it is necessary to set the pulse length a few microseconds shorter than the ring round-trip time. The resulting pulse train is monitored using an InGaAs PD and a LeCroy 300 MHz oscilloscope.

5.1.1 The acousto-optic modulator

As the name implies, the AOM is a device which utilizes sound for modulation of light and Fig. 5.2(a) shows the underlying principle. A piezo-electric transducer generates high frequency acoustic plane waves inside an optically transparent medium, often a crystal with suitable properties e.g. GaAs or TeO_2. Opposite the transducer sits an absorber which damps the acoustic waves to keep standing waves from arising inside the crystal. Through pe-

riodic compression and rarefaction of the crystal the acoustic waves generate a Bragg grating upon which light injected from the side of the crystal is diffracted. AOMs usually operate in the so-called Bragg regime where light is only diffracted into either the $+1$ or -1 order depending on whether the light moves with (leading to the -1 order) or against (leading to the $+1$ order) the acoustic waves. The diffraction process can be seen as an elastic collision between a photon, with wavevector, $\bar{k}_{l,\mathrm{in}}$, and a phonon, $\bar{k}_a$, in which a new photon, $\bar{k}_{l,\mathrm{out}}$, is created. This requires conservation of both momentum and kinetic energy, but because $\bar{k}_a$ is much smaller than $\bar{k}_{l,\mathrm{in}}$ and $\bar{k}_{l,\mathrm{in}}$ the latter two can be assumed to be of equal length leading to an isosceles wavevector diagram as shown in Fig. 5.2(b) [54]. From the figure it is seen that the diffraction or Bragg angle, α_B is

$$\alpha_B = \sin^{-1}\left(\frac{k_a}{2k_l}\right) = \sin^{-1}\left(\frac{\lambda}{2\Lambda}\right), \tag{5.1}$$

where k_l and k_a are the wavenumbers of the optical and the acoustic waves, respectively [55]. By designing the AOM such that light is coupled in and subsequently collected at the angle α_B the transmission through the device can be controlled by turning the acoustic field on or off. In general about 90% of the incoming light can be coupled to the diffracted wave whereas very little light, more than 50 dB below the input power, is transmitted when the acoustic field is off, thereby ensuring a very high extinction ratio.

The frequency of the diffracted lightwave is shifted compared to the incoming light. Because the photon-phonon collision is elastic the kinetic energy is conserved and this yields

$$h\nu_{l,\mathrm{out}} = h\left(\nu_{l,\mathrm{in}} + \nu_a\right), \tag{5.2}$$

where h is Planck's constant and $\nu_{l,\mathrm{out}}$, $\nu_{l,\mathrm{in}}$, and ν_a are the frequencies of the incoming light, diffracted light and the acoustic field, respectively. A more qualitative explanation is that the light is scattered off a moving sound wave and therefore experiences a Doppler shift. It is this frequency shift that makes the AOM an obvious candidate for use in the LSFS [56]

The maximum modulation frequency of the AOM is determined by the time it takes for the acoustic wave to move through the laser beam. An example of the rise and fall times of the AOMs used in this project is shown in Fig. 5.2(c). The modulator is capable of opening to about 80% of the full transmission in a matter of nanoseconds, whereas the last 20% takes more than $5\,\mu$s. The same applies when the AOM is closing. This poses a limiting factor for

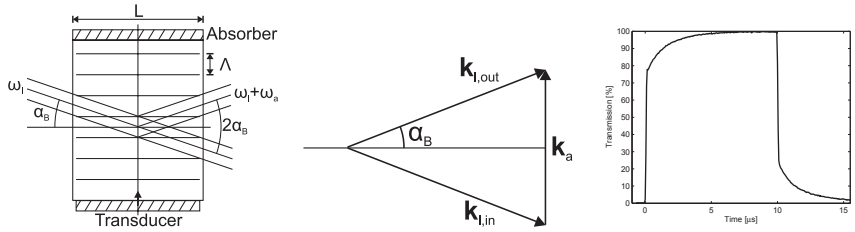

Figure 5.2: (a) Schematic drawing of an AOM. The incoming light is diffracted (into the $+1$ order) by the Bragg grating generated by the acoustic waves moving from the transducer toward the absorber. (b) Wavevector diagram for Bragg diffraction. Note than in reality $\bar{k}_{\mathrm{a}}$ is much shorter than $\bar{k}_{l,\mathrm{in}}$ and $\bar{k}_{l,\mathrm{in}}$. (c) Measured time response of one the AOMs used in the project.

the LSFS in that it dictates how close two consecutive pulses can be placed to each other without the tail of one pulse stretching into the next.

The width, L, of the transducer affects the number of diffraction orders. If the width becomes small, the acoustic waves no longer approximate plane waves and higher diffraction orders becomes possible with resulting higher order frequency shifts. This is called the Raman-Nath regime. Usually AOMs, including the two used in this project, operate in the Bragg regime and should thus give rise to only one diffracted beam. The criterion for the Bragg regime can be stated as

$$2\pi\frac{\lambda L}{\Lambda^2} >> 1. \tag{5.3}$$

If, however, the acoustic signal is not a pure sinusoidal, or if the acoustic waves becomes distorted in their way through the crystal, light can become multiple diffracted and other diffraction orders occur. These are called intermodulation products and the resulting frequency shifts of these are different from the first order shift e.g. $2\nu_{a,1} - \nu_{a,2}$, $\nu_{a,1} \pm \nu_{a,2}$, $2\nu_{a,1}$, or $2\nu_{a,2}$ are possible frequencies [57, 58]. In actual AOMs both of these phenomena occur; the first due to higher order harmonics in the transducer drive signal and the latter due to acoustic nonlinearities in the crystal. The intermodulation products are in general very weak and will furthermore be spatially separated from the main diffraction order; nevertheless a fraction of the transmitted light will be shifted in frequency compared to the main signal.

5.2 FSPT in the time domain

The overall shape, or envelope, of the FSPT as well as the individual pulses generated by the LSFS depends on a number of different parameters. The powers of the input signal, P_s, and amplifier pump, P_p, are obviously important for achieving a constant output power level, and the center frequency and width of the BPF influences e.g. how many consecutive pulses can be generated. Also various time constants such as the pulse length, $T - p$ the time for the pulse to make one revolution in the ring T_r, the total time of the entire FSPT T_t, and down time between pulse trains i.e. the time from one train is terminated to another is started T_{td}. The influence of these parameters, both in relation to experimental measurements and to different models, is discussed in the following.

Shown in Fig. 5.3 is an example of an FSPT generated using the setup shown in Fig. 5.1 with a 230 m SMF as delay line. It consists of 156 pulses each about 1 μs long and the input power of the seed pulse is approximately 7 mW. The first pulse in the pulse train is seen to be lower than following and this is due to the input 3 dB coupler not dividing the pulse power perfectly equal but rather directs a fraction more of the power into the ring. Over the first 100 pulses the envelope of the pulse train is quite flat but with a local minimum after around 50 pulses. After 100 pulses the pulse power starts to decrease and after 156 the train is terminated. The bottom level, i.e. the power level between the pulses, is a measure of the ASE building up in the ring. Caution should be exercised, however, when estimating the ASE growth on this basis, as the bottom level measured is partly if not mainly due to the finite closing time of the seed AOM as mentioned in Section 5.1.1. Therefore the bottom level here is seen to follow the top level and the ASE increase should rather be evaluated based on the difference between the top and the bottom level. On top of this a fraction of the bottom level originates from light leaking through the otherwise closed seed AOM. Although difficult to see in the figure the shape of the individual pulses changes through the FSPT. This is due to depletion of the amplifier pump and will be described in greater detail in Section 5.3.2.

5.2.1 Time independent model

A model describing the development of signal and noise inside an LSFS with an EDFA for loss compensation has been presented in [49], and this model builds on the assumption that the total output power from the ring is constant in time; an assumption which is justified through measurements. As a conse-

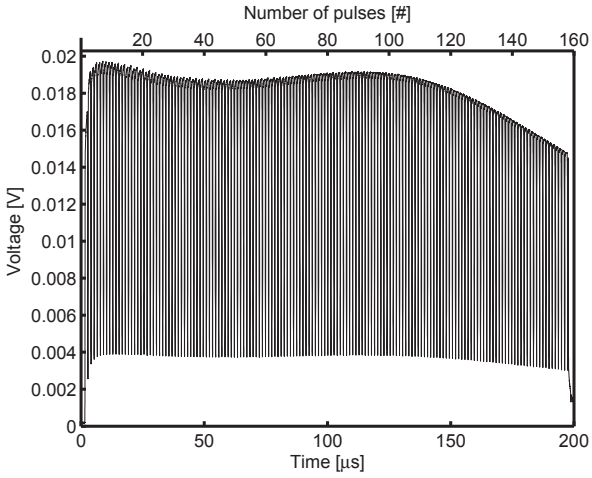

Figure 5.3: FSPT with 156 1 μs pulses as function of time.

quence of the constant output power approximation all temporal dependencies disappear from the rate equations describing the propagation of light through the ring, and the equations need only to be evaluated once for every revolution. The resulting propagation equations are written as

$$P_s^{i+1}\left(\nu_s^i + \Delta\nu\right) = L\left(\nu_s^i\right) G^i P_s^i\left(\nu_s^i\right), \tag{5.4}$$

$$pn^{i+1}\left(\nu + \Delta\nu\right) = L\left(\nu\right) G^i pn^i\left(\nu\right) + 2n_{\mathrm{sp}}(G^i - 1)h\nu L(\nu), \tag{5.5}$$

where index i is used to denote the revolution number, P_s^i is the signal power in the i^{th} pulse at signal frequency f_s^i, $L\left(\nu\right)$ is the transfer function of the optical bandpass filter, G^i is the amplifier gain, pn^i is the spectral noise power density in the i^{th} pulse, n_{sp} is the spontaneous emission factor of the EDFA and h is Planck's constant. The frequency of the $i + 1^{\mathrm{th}}$ pulse is thus the frequency of the i^{th} pulse plus the constant frequency shift, $\Delta\nu$, induced by the ring AOM. The first term in Eq. (5.5) represents noise generated in previous revolutions and is recirculated, whereas the second term describes spontaneous emission added to the noise by the amplifier in a given revolution. The spontaneous emission is generated evenly over all frequencies within the filter bandwidth and it is assumed that the ring AOM shifts all frequencies equally as implied through the notation $(\nu + \Delta\nu)$ in Eq. (5.5). The signal and noise are seen to be coupled through the amplifier gain, and the evolution of signal and noise is found iteratively by stepping through the desired number of revolutions. The

total noise power in revolution $i+1$ is found by integrating over all frequencies

$$P_n^{i+1} = \int_0^\infty pn^{i+1}(\nu)\,\mathrm{d}\nu, \tag{5.6}$$

and the constant power approximation implies that

$$P_{\mathrm{const}} = P_s^i + P_n^i = P_s^{i+1} + P_n^{i+1}. \tag{5.7}$$

Using this expression the gain is evaluated from

$$G^i = \frac{P_{\mathrm{const}}}{L(\nu_s^i)P_s^i + \int_0^\infty L(\nu)\left[pn^i(\nu) + 2n_{\mathrm{sp}}\left(\frac{G^i-1}{G^i}\right)h\nu\right]\,\mathrm{d}\nu} \Leftrightarrow \tag{5.8}$$

$$G^i = \frac{P_{\mathrm{const}} + 2n_{\mathrm{sp}}h\int_0^\infty L(\nu)\nu\,\mathrm{d}\nu}{L(\nu_s^i)P_s^i + \int_0^\infty L(\nu)\left[pn^i(\nu) + 2n_{\mathrm{sp}}h\nu\right]\,\mathrm{d}\nu}. \tag{5.9}$$

As mentioned in Section 5 the model is easily expanded to describe e.g. a sweeping BPF [45], a different signal wavelength [43] or different type of optical amplifier [48]. The former implies that the filter center frequency is shifted along with the signal e.g. in steps following

$$\nu_c^i = \nu_s^0 + \Delta + i\Delta\nu + i\delta\nu, \tag{5.10}$$

where ν_s^0 is the initial signal frequency, Δ is the offset between initial signal frequency and initial filter center frequency, $\Delta\nu$ is the signal frequency shift and $\delta\nu$ is the difference in step size between the signal frequency shift and the filter frequency shift. Whereas in the latter two cases a suitable amplifier model must be incorporated.

The model has been implemented in Matlab® for testing against experimental results and an example of such a simulation is shown in Fig. 5.4(a) and for comparison in Fig. 5.4(b) is shown the pulse train envelope of the FSPT shown in Fig. 5.3. The abscissa axes in the figures show the top level of the pulse train envelope minus the bottom level and normalized to the power of the first pulse. Clearly the simulation shows a similar behaviour as the measurement, but is also noted that the power levels do not match. After 156 revolutions the signal power compared to the ASE power is dropped by around 30% for the measurement whereas in the simulation the power is down by less than $1‰$. In the simulation the input power was set to 7 mW, the overall loss to 10.5 dB, and the spontaneous emission factor n_{sp} to 6.31 in accordance with measured values. The filter width and center position, however, were used as fitting parameters in order to get the best possible agreement with the measurement. The center position is in general unknown since the filter adjustment

system does not allow adequately accurate determination of the position. Thus, it makes good sense to work with this as a fitting parameter. The centre postion resulting from the fitting was $\nu_s^0 + 73\Delta\nu$. The filter width, on the other hand, was measured to 0.84 nm or 102.8 GHz, and it should therefore not be necessary to change this in the simulation. However, in order to attain the shown curve shape, it was necessary to use a much narrower filter of 17.7 GHz. Furthermore, the FSPT also depends on the time between pulse trains as this will influence the amplifier. A more elaborate model is therefore necessary in order to accurately simulate the generated FSPT.

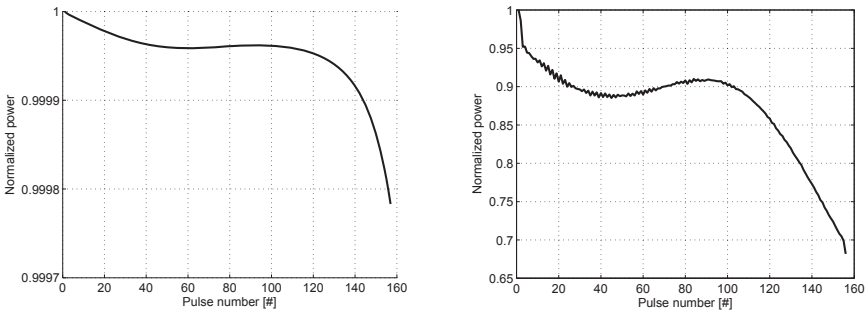

(a) (b)

Figure 5.4: (a) Simulation of signal power minus noise power in the LSFS as function of pulse number. (b) Signal power minus noise power as function of pulse number, based on the measurements shown in Fig. 5.3.

5.2.2 Time dependent model

Experiments have shown, e.g. in Fig. 5.3, that the individual pulse shape can vary drastically down through the pulse train, an effect which the time independent model can not account for. It is therefore necessary to incorporate the time dependencies of the optical amplifier and AOMs. The proposed model separates it self from the time independent model in that it takes into account the finite response of the sed AOM and uses time dependent rate and propagation equations to describe the amplifier.

With the model we aim to include all physical effects influencing the LSFS, and to neglect physical effects not affecting the LSFS. Dispersion is thus neglected due to the use of spectrally narrow pulses with a frequency bandwidth defined by the laser linewidth and, using a similar argument, the signal is simulated as monochromatic waves [59]. Because of the backward amplifier the

polarization dependence of the amplifier is not considered [60], and due to the frequency shift induced for each circulation of the ring, and the down time between pulses, laser conditions, such as phase matching, are not required. Additionally stimulated Brillouin scattering (SBS), recaptured Rayleigh scattering, and backward propagating ASE are neglected due to the low power circulating in the ring at each frequency and the elimination of backwards traveling light obtained by isolators build in to the amplifiers. Finally, scalar propagation equations are used for simplicity.

The time dependent model then constitutes the basis for a numerical simulation of the FSPT implemented in Matlab and compared to experiments in Section 5.3. For the remaining part of this chapter we aim our attention at describing the more technical aspects of the simulation as well as the propagation equations used.

In the simulation each component within the ring, except the fibre amplifier, is described by a transfer function in the time as well as the frequency domain. The fibre amplifier is described using propagation equations. For each round trip of the ring, the signal power is propagated through each of the elements in the same order as in the physical ring. The 3 dB coupler, WDM coupler, and the isolator are all considered to a simple loss of power corresponding to the experimentally measured attenuation. The loss of the BPF is wavelength dependent and is given by a Gaussian distribution, fitted to the measured loss. The loss of the AOMs are simulated as time dependent corresponding to the measured response function. The frequency shifts induced by the AOMs are simulated by defining the signal power as an array, representing monochromatic waves with a frequency spacing equal to the shift induced by the AOMs (40 MHz). The entire array is then shifted each time it passes through the AOM.

Two different optical amplifiers, an EDFA and a Raman amplifier, are considered. Both are modeled as backward pumped, and for both, the assumption is made that the group velocity of the signal and pump are identical. This implies that in a time slot Δt, the pump and signal both propagate the same distance Δz. The amplifier fibre can thus be discretized into corresponding length and time segments. In this way the amplifier can be treated as a concatenation of discrete amplifiers of length Δz where the output from one is used as input in the next. The input pump, on the other hand, will be the output from the following spatial segment, but previous time slot, due to the backward pumping scheme. In this way one time segment is affected by previous times and a memory is therefore inherent in the simulation. The amplifier propagation equations are solved using an ordinary differential equation (ODE) solver

in Matlab®.

The pulse train is generated by stepping through all time segments defined by the discretization of the amplifier fibre. An array representing the power of the seed laser is predefined in time such that it generates the initial pulse and the leak power defined by the input AOM. For each time step the power from the seed laser array is added to the output of the ring at a corresponding time through the coupler and stepped through the individual components of the setup. The part of the array representing light leaking through the input AOM, acts as the initial noise which continues to grow due to continued adding of leaked light and spontaneous emission. The resulting power segment is then the output power at a time corresponding to the input time plus the travel time around the ring. The pulse train generated by the LSFS is a result of the modulated seed laser added to the output signal through the coupler for each time step. In order to take into account the time between pulse trains where there is no signal light in the ring, but where the pump light might still be active, each simulation runs over two consecutive pulse trains. In this way the second pulse train obtained has the proper initial conditions.

The two amplifiers considered, EDFA and Raman amplifier, are described by different propagation equations. Thus, we treat them one at a time.

Erbium doped fibre amplifier

The EDFA has gained currency as the optical amplifier of choice within the field of telecommunication as it offers high gain in the wavelength range around 1550 nm with low pump power. It consists of an optical fibre doped with Erbium ions (Er^{3+}) and it is optically pumped using either 980 nm or 1480 nm light. The amplification process can be modeled by a three-level system as illustrated in Fig. 5.5(a). Pump light, $h\nu_p$, is absorbed by an Erbium ion, thereby excited from the ground energy level, E_1, to a higher level, E_3, from where it rapidly decays nonradiatively represented by the notation A_{32} into a metastable energy state, E_2. Besides from a small amount that is reemitted as stimulated emission at the pump frequency, ν_p. The difference between the two energy levels E_1 and E_2 matches the photon energy of light around 1550 nm which can therefore be amplified through stimulated emission, $h\nu_s$, when the Erbium ion is in energy state E_2. Also shown in the figure is spontaneous emission, A_{21}, arising when the Erbium ion decays spontaneously to the ground level either nonradiatively or by emitting a photon, and finally it is indicated on the figure that the signal of energy $h\nu_s$ can be absorbed by the amplifier. If the spontaneously emitted photon is guided in the fibre, it will be

amplified leading to noise called ASE [24]. The average lifetime of the excited level, E_2, or the Erbium ion is 10 ms before it spontaneously decays.

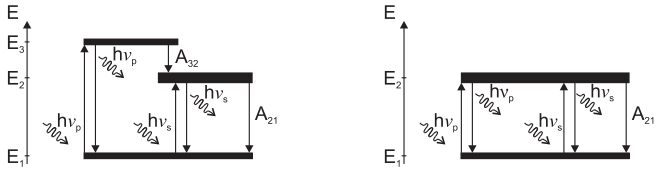

Figure 5.5: (a) Sketch of the EDFA three-level model. $h\nu_p$ is the pump photon energy, $h\nu_s$ the signal photon energy, A_{32} represents rapid non-radiative decay to the E_2 state, and finally A_21 is the spontaneous emission from E_2 to E_1. (b) The EDFA two-level model.

Mathematically, the three level system is described through the population densities, N_i, of the three energy levels, $E_{i,\ i=1,2,3}$

$$\begin{aligned}
\frac{dN_1(z,t)}{dt} &= -\left[\sum_k \frac{\sigma_{sa,k}\Gamma_{s,k}}{h\nu_{s,k}A}\left(P_{\mathrm{s}}(z,t,\nu_k)+P_a^{\pm}(z,t,\nu_k)\right)\right. \\
&+ \left.\frac{\sigma_{pa}\Gamma_p}{h\nu_p A}P_p^{\pm}(z,t,\nu)\right]N_1(z,t) \\
&+ \left[\sum_k \frac{\sigma_{se,k}\Gamma_{s,k}}{h\nu_{s,k}A}\left(P_{\mathrm{s}}(z,t,\nu_k)+P_a^{\pm}(z,t,\nu_k)\right)+A_{21}\right]N_2(z,t) \\
&+ \frac{\sigma_{pe}\Gamma_p}{h\nu_p A}P_p^{\pm}(z,t,\nu)\,N_3(z,t)\,, \qquad (5.11)\\
\frac{dN_2(z,t)}{dt} &= \sum_k \frac{\sigma_{sa,k}\Gamma_{s,k}}{h\nu_{s,k}A}\left(P_s(z,t,\nu)+P_a^{\pm}(z,t,\nu)\right)N_1(z,t) \\
&- \left[\sum_k \frac{\sigma_{se,k}\Gamma_{s,k}}{h\nu_{s,k}A}\left(P_s(z,t,\nu)+P_a^{\pm}(z,t,\nu)\right)+A_{21}\right]N_2(z,t) \\
&+ A_{32}N_3(z,t)\,, \qquad (5.12)\\
\frac{dN_3(z,t)}{dt} &= -\frac{dN_1(z,t)}{dt}-\frac{dN_2(z,t)}{dt}, \qquad (5.13)
\end{aligned}$$

where k is the frequency index, and s, p, and a denotes signal, pump and ASE, respectively. Emission and absorption cross sections, σ_e, σ_a, light-to-core overlap Γ, and fibre loss, α, are in general frequency dependent. A is

the fibre core area and h is Planck's constant. The rate equations are functions of time, t, and of distance along the fibre, z. The spatial development of signal, pump, and noise power, $P_{j,\, j=s,p,a}$ is described through the following propagation equations

$$\frac{dP_p^{\pm}(z,t,\nu)}{dz} = \pm\left[\Gamma_p\left(\sigma_{pe}N_3(z,t)\right) - \sigma_{pa}N_1(z,t) - \alpha_p\right]P_p^{\pm}(z,t,\nu), \quad (5.14)$$

$$\frac{dP_s^{\pm}(z,t,\nu)}{dz} = \left[\Gamma_{s,k}\left(\sigma_{se,k}N_2(z,t)\right) - \sigma_{sa}N_1(z,t) - \alpha_{s,k}\right]P_s^{\pm}(z,t,\nu), \quad (5.15)$$

$$\begin{aligned}\frac{dP_a^{\pm}(z,t,\nu)}{dz} = &\pm\left[\Gamma_{s,k}\left(\sigma_{se,k}N_2(z,t)\right) - \sigma_{sa}N_1(z,t) - \alpha_{s,k}\right]P_a^{\pm}(z,t,\nu) \\ &\pm 2\sigma_{se,k}N_2(z,t)\,\Gamma_{s,k}h\nu B,\end{aligned} \quad (5.16)$$

where the superscript $\pm$ indicates the direction of the pump and the ASE. The last term in Eq. 5.16 is the ASE power generated in the Erbium doped fibre in a bandwidth B.

The lifetime of the highest excited state, E_3, is much shorter than that of E_2, with a decay rate of around $10^9\ \mathrm{s}^{-1}$. As a good approximation it can therefore be regarded as instantaneous, reducing the three-level system to a two-level system, see Fig. 5.5(b). The approximation is particularly used when modeling an EDFA with a 1480 nm pump because it pumps directly into the top of the E_2 band resulting in an even faster decay to the lowest E_2 state. If a two-level model is used the rate equations reduce to

$$\begin{aligned}\frac{dN_1(z,t)}{dt} = &-\left[\sum_k \frac{\sigma_{sa,k}\Gamma_{s,k}}{h\nu_{s,k}A}\left(P_{\mathrm{s}}(z,t,\nu_k) + P_a^{\pm}(z,t,\nu_k)\right)\right. \\ &\left. + \frac{\sigma_{pa}\Gamma_p}{h\nu_p A}P_p^{\pm}(z,t,\nu)\right]N_1(z,t) \\ &+\left[\sum_k \frac{\sigma_{se,k}\Gamma_{s,k}}{h\nu_{s,k}A}\left(P_{\mathrm{s}}(z,t,\nu_k) + P_a^{\pm}(z,t,\nu_k)\right)\right. \\ &\left. + \frac{\sigma_{pe}\Gamma_p}{h\nu_p A}P_{\mathrm{p}}^{\pm}(z,t,\nu) + A_{21}\right]N_2(z,t)\end{aligned} \quad (5.17)$$

$$\frac{dN_2(z,t)}{dt} = -\frac{dN_1(z,t)}{dt}, \quad (5.18)$$

and the propagation equations

$$\frac{dP_p^{\pm}(z,t,\nu)}{dz} = \pm\left[\Gamma_p\left(\sigma_{pe}N_2(z,t)\right) - \sigma_{pa}N_1(z,t) - \alpha_p\right]P_p^{\pm}(z,t,\nu), \quad (5.19)$$

$$\frac{dP_s^{\pm}(z,t,\nu)}{dz} = \left[\Gamma_{s,k}\left(\sigma_{se,k}N_2(z,t)\right) - \sigma_{sa}N_1(z,t) - \alpha_{s,k}\right]P_s^{\pm}(z,t,\nu), \quad (5.20)$$

$$\frac{dP_a^{\pm}(z,t,\nu)}{dz} = \pm\left[\Gamma_{s,k}\left(\sigma_{se,k}N_2(z,t)\right) - \sigma_{sa}N_1(z,t) - \alpha_{s,k}\right]P_a^{\pm}(z,t,\nu) \pm 2\sigma_{se,k}N_2(z,t)\,\Gamma_{s,k}h\nu\Delta\nu. \quad (5.21)$$

These equations are simpler to implement and faster to solve and have therefore been used for simulating the LSFS output.

The EDFA used in this study is a commercially available product, easily incorporated into the setup of the LSFS. However, this also means that many of the parameters in the rate and propagation equations are unknown. Therefore parameters adopted from the literature are used. The transition rate for spontaneous emission A_{21} is set to $100\ \mathrm{s}^{-1}$, transmission losses α are set to zero due to the short fibre length of the amplifier, the fibre core area is set to $12.6\ \mu\mathrm{m}^2$, the total Er^{+3} population, N_t, is set to $2.25 \cdot 10^6\ \mu\mathrm{m}^{-1}$, and the overlap between the optical modes of pump and signal and the Erbium ions, γ, was set to 0.4 [61]. Based on the time it takes for a pulse to propagate the ring the amplifier fibre is estimated to be 20 m in length. The emission and absorbtion cross sections σ_e and σ_a are set to $3.6 \cdot 10^{-25}\ \mathrm{m}^2$ and $3.2 \cdot 10^{-25}\ \mathrm{m}^2$, respectively [62].

Raman amplifier

Another fibre based optical amplifier is the Raman amplifier and as the name implies it relies on Raman scattering for amplification of the signal light. Raman scattering is a nonlinear process in which light interacts with vibrations in the guiding medium, in this case a fibre. It can be described as inelastic scattering of light on a molecule in which energy is transferred to the molecule in form of excitation to a higher vibrational state, and as a consequence the light is downshifted in frequency. The opposite situation where energy is transferred from the material to the light is also possible, though less probable. The frequency shift depends strongly on the vibrational states of the host material, and thus on the molecular composition and the temperature, and the width of possible frequency shifts determines the Raman gain bandwidth. The amorphous structure of silica causes the vibrational states to spread out, resulting in a wide

range of possible shifts with a broad peak around 13.2 THz. For amplifier operation, stimulated Raman scattering (SRS), in which energy is transferred from a pump to a signal, is utilized. As long as the signal frequency lies within the Raman gain bandwidth of the pump, stimulated emission and thus amplification is possible [59]. Compared to the EDFA it is less efficient at converting pump light into signal and thus higher pump powers and longer interaction lengths are in general necessary.

The Raman fibre amplifier is simulated by solving the dynamic propagation equations describing signal, pump, and ASE, respectively

$$\frac{dP_s\left(z,\nu_k\right)}{dz} = g_R\left(\Omega\right)P_p\left(z,\nu\right)P_s\left(z,\nu_k\right) - \alpha_s P_s\left(z,\nu_k\right), \tag{5.22}$$

$$\pm\frac{dP_p^{\pm}\left(z,\nu\right)}{dz} = -\sum_k \frac{\nu_p}{\nu_{s,k}} g_R\left(\Omega\right)P_p^{\pm}\left(z,\nu\right)\left(P_s\left(z,\nu_k\right)+P_a^{\pm}\left(z,\nu_k\right)\right) - \alpha_p P_p^{\pm}\left(z,\nu\right), \tag{5.23}$$

$$\pm\frac{dP_a^{\pm}\left(z,\nu_k\right)}{dz} = g_R\left(\Omega\right)P_p^{\pm}\left(z,\nu\right)P_a^{\pm}\left(z,\nu_k\right) - \alpha_s P_a^{\pm}\left(z,\nu_k\right) + 2g_R\left(\Omega\right)\left[1+\eta\left(T\right)\right]h\nu_{s,k}BP_p^{\pm}, \tag{5.24}$$

where z is the distance along the fibre, t is the time, P_p is the pump power with frequency ν_p, and $g_R\left(\Omega\right)$ is the frequency dependent Raman gain coefficient. k is the frequency index of the signal power, $P_{s,k}$ is the signal power of frequency $\nu_{s,k}$ and h is Planck's constant [60, 63, 64]. α_s and α_p are the transmission loss of the signal and pump, respectively, and the signal loss is assumed to be the same for all signal frequencies. Signal and noise are described by similar equations except for the last term in Eq. (5.24) which describes spontaneous emission added by the amplifier. In the simulation no discrimination regarding phase is made, i.e. any contribution at the signal frequency, even if it originates from spontaneous emission, is regarded as signal. This means that both signal and ASE can be calculated using Eq. (5.24), reducing the number of calculations necessary in the simulations. This, together with the fact that the Raman amplifier used in this study is backward pumped and backward traveling ASE is neglected due to an isolator incorporated into the ring, implies that the propagation equations reduce to

$$\frac{dP_s\left(z,\nu_k\right)}{dz} = g_R\left(\Omega\right)P_p^{-}\left(z,\nu\right)P_s\left(z,\nu_k\right) - \alpha_s P_s\left(z,\nu_k\right) + 2g_R\left(\Omega\right)\left[1+\eta\left(T\right)\right]h\nu_{s,k}BP_p^{-}, \tag{5.25}$$

$$\frac{dP_p^{-}\left(z,\nu\right)}{dz} = \sum_k \frac{\nu_p}{\nu_{s,k}} g_R\left(\Omega\right)P_p^{-}\left(z,\nu\right)P_s\left(z,\nu_k\right) + \alpha_p P_p^{-}\left(z,\nu\right), \tag{5.26}$$

where P_p^- represents the backward traveling pump. In Eq. (5.25) the first term on the right hand side describes gain, the second term attenuation, while the last term in Eq. (5.25) describes the spontaneous emission at the i^{th} frequency in a frequency bandwidth B, in this case 40 MHz, and the so-called phonon occupancy factor

$$\eta\left(T\right) = \frac{1}{\exp\left[\frac{h\Omega}{k_B T}\right] - 1}, \tag{5.27}$$

where $\Omega = \nu_p - \nu_{s,k}$ is the frequency difference between signal and pump, k_B is Boltzmann's constant and T is the absolute temperature. The first term on the right hand side of Eq. (5.26) accounts for the depletion of the pump due to the signal, and in Section 5.3.2 we demonstrate that this term has a significant impact on the pulseshape. The last term on the right hand side accounts for attenuation of the pump.

As described in Section 5.2.2 the propagation equations (5.25) and (5.26) are solved by discretization of the Raman fibre into sections Δz and via this the signal and pump powers are also discretized into time segments Δt of corresponding lengths, $\Delta t = \Delta z / V_g$. The equations are solved for each spatial section and corresponding time segment for each power segment of the pulse train. The initial condition of the simulation is given by the steady state solution of the equations at zero signal power.

5.3 Temporal measurements

In this section different examples of FSPTs are presented together with time dependent simulations. In the following it will become clear that the individual pulse, even though so intended, is often far from rectangular and it will furthermore change through the pulse train. When comparing simulations with measurements, it is therefore necessary to define some reference points and these are, as shown in Fig 5.6, the maximum, $\circ$, mean, $\diamond$, and minimum, $\square$, of the pulse power, and the mean power between pulses, $\times$.

5.3.1 EDFA assisted LSFS

As mentioned in Section 5.2, the shape of the pulse train envelope as well as the individual pulses, depends on several parameters and these are presented in this section. For use in a lidar measurement it is desirable to have as flat a pulse train envelope as possible and to obtain this for a pulse train of a given length, the filter center frequency and amplifier pump power must be adjusted.

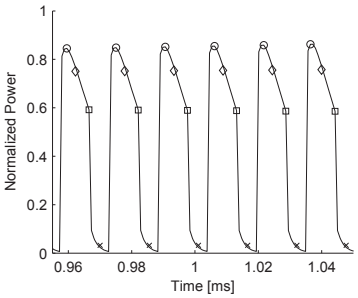

Figure 5.6: Sketch of six pulses in a pulse train with four reference points used for comparison of individual pulses: ∘ maximum, ◇ mean, and □ minimum of the pulse power, and × the mean power between pulses.

Such a pulse train optimized through adjustment of the pump power and BPF center frequency for having a flat envelope is shown in Fig. 5.7 together with a simulation based on the time dependent model. The FSPT consists of 147 1 μs pulses, the total train time T_t is 183.6 μs, and the input signal power is 5 mW. As likewise mentioned the exact parameters of the amplifier and center frequency of the BPF are not known. Therefore, the pump power and center frequency were made fitting parameters in order to obtain best possible agreement measurement and simulation. The resulting values for these two parameters were 180 mW and 8 GHz above the input signal frequency, respectively. The top plot shows the envelope of the FSPT as function of time by use of the four different reference points defined in Fig. 5.6 and for both measured values (black) as well as simulations (red). It is seen that the simulations predict the measured values very well for the three reference points describing the top level, and that the pulse shape is relatively constant through out all 147 pulses. The time dependent model, at least in this special case, is thus very capable of simulating the LSFS. At the bottom level, however, there is a clear discrepancy between measurement and simulation with the former being lower than the latter. This is considered caused by the finite closing time of the seed AOM which is not described accurately enough in the simulation. It should be emphasized that this is a consequence of the description of the particular component and not the model in general. The bottom panel shows a close-up of individual pulses in the start, middle and end of the pulse train. As implied by the top panel, excellent agreement between measurement and simulation is found also at this level, with merely the minimum pulse power

being overestimated.

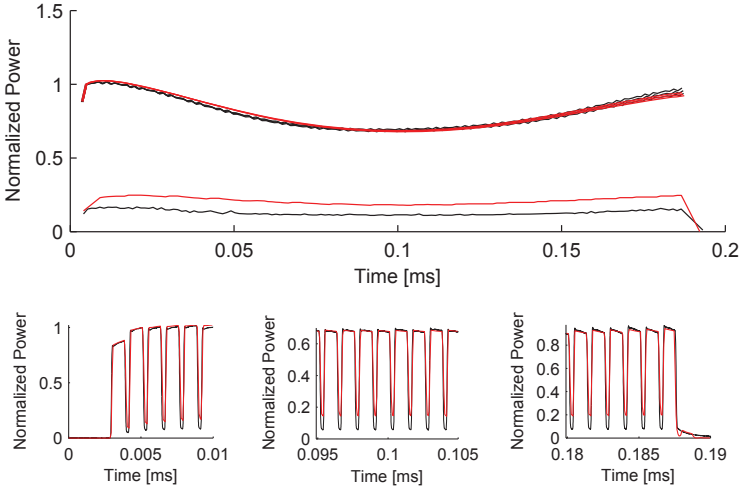

Figure 5.7: Top panel: Plot of the measured (-) and simulated (-) pulse train envelope based on the four reference points defined in Fig. 5.6. Bottom panel: Close-up of individual pulses in the beginning, middle, and end of the FSPT.

Signal and pump power

With the FSPT discussed above as reference, the different power and time parameters can then be changed individually to investigate their influence on the pulse train. However, with at least seven different parameters to vary, an exhaustive description of each and their impact on the FSPT is not presented. Instead in the following, the most important effects are discussed.

Fig. 5.8 shows the measured and simulated mean pulse power envelope of the pulse train for different values of the input pulse power but otherwise with the same settings as in Fig. 5.7. The simulation does not replicate the measurements exactly but some of the same tendencies are seen. When the input signal power is increased, the trend is that the power of the following pulse drops. This is because the energy level from where stimulated emission occurs is being emptied faster than the pump can fill it, but then as a consequence of the decrease in signal power, the population of the amplification level starts to recover and the signal can increase again. Two of the measured curves stand a bit out from the rest in that they show an increase in power level in the beginning of the pulse train. These are the ones representing the lowest and the

highest signal power of 3 mW and 22 mW. This is similarly explained by depletion of the pump, since for the former the signal level starts out being low and is therefore amplified more. For the latter we shall remember that between each pulse train there is a short period of time, T_{td}, where there is no signal in the amplifier. During this time span the pump has time to build up, so when a new train is initiated the first few pulses experience a net gain.

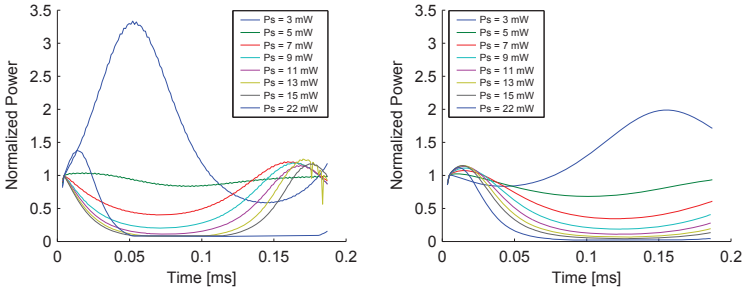

Figure 5.8: (a) Measurements of the mean pulse power envelope of the FSPT for different input signal powers P_s. (b) Simulations of the mean pulse power envelope of the FSPT for different input signal powers P_s.

Fig. 5.9 is a similar figure, only here it is the pump power, P_p, instead of the signal power which is varied. Since the actual pump power is not known, it is for the measured envelopes given as the current to the pump diode as stated on the EDFA display and for the simulations, values which resulted in plots showing good qualitative match to the measurements, were chosen. These values are given in the figures. As before a trend is observed that the pulse power begins to oscillate as the pump is depleted and recovers. The same tendency is seen in the simulations. Only for the lowest pump power $(898\ \mathrm{mW})$ does the signal power drop almost to zero without signs of recovering within the time of the pulse train.

From the figures shown in this section it is clear that in order to obtain a flat and stable pulse train it is important to find the right balance between signal and pump power. This balance also includes the different time parameters as they influence the average signal power seen by the amplifier. If the pulses are made shorter compared to the round trip time, T_r, the average signal power drops and the output power becomes unstable as was seen in Fig. 5.8. The same applies if the down time between pulse trains, T_{td}, is increased. However, the average power must be considered in relation to the averaging time of the EDFA itself,

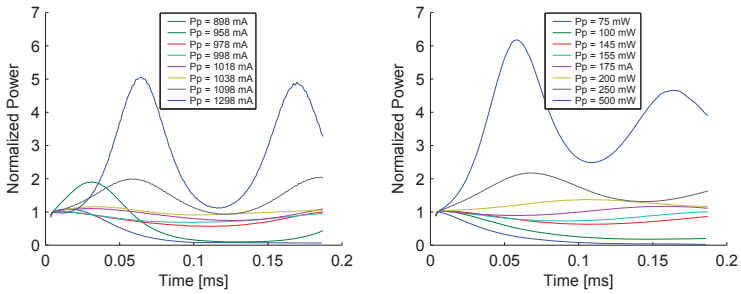

(a) (b)

Figure 5.9: (a) Measurements of the mean pulse power envelope of the FSPT for different pump powers P_p. (b) Simulations of the mean pulse power envelope of the FSPT for different pump powers P_p.

determined by the decay rate A_{21} of the amplification energy level E_2.

Also important is the BPF which must be optimized as well. It is important the total signal frequency range lies within the filter passband since if the filter attenuates the signal ASE will rapidly grow up. Even though the frequency shifts of the signal in this work is 40 MHz and thereby very small compared to the BPF of around 100 GHz, the attenuation still has a spectral distribution and different signal frequencies might be differently attenuated. There is in other words a complex interaction between various temporal and spectral parameters underlying the output of the LSFS, and this is why a model describing the dynamics of the each individual pulse is necessary in order to accurately simulate the FSPT. The disagreements between measurements and simulations are mainly ascribed to an inaccurate description of the actual EDFA used.

5.3.2 Raman assisted LSFS

As mentioned previously most of the LSFSs described in the literature operate at telecom wavelengths and include an EDFA to compensate for the losses introduced by the components in the ring. However, EDFAs have certain constraints of which the most critical is that the wavelength range of operation is limited to wavelengths between 1535 nm to 1600 nm. To circumvent this limitation Raman gain might be used to compensate for the loss. The Raman gain is well suited for this purpose since the wavelength of optimum gain is solely determined by the pump wavelength. On the other hand, Raman amplifiers may be long compared to EDFAs implying that, if quasi-CW output is wanted, the output pulses also become very long. In order to investigate the possibility of replacing the EDFA with a Raman amplifier such an amplifier was built in the laboratory and tested in the LSFS. With the relatively long pulses compared to those generated by the EDFA assisted LSFS, we furthermore get a chance to look into how, not only the pulse train envelope, but also the individual pulses change through out the pulse train.

The Raman amplifier used in this study is home built and includes a 3.17 km long high gain Raman fibre from OFS Fitel Denmark, backward pumped through a WDM coupler by a 1455 nm fibre laser giving a maximum gain around 1555 nm. The Raman fibre has a gain coefficient of $2.44\ (\mathrm{W}\cdot\mathrm{km})^{-1}$ at 1453 nm and attenuation of 0.40 dB/km at 1450 nm and 0.31 dB/km at 1550 nm. An isolator heavily attenuates residual pump light and ensures one way circulation in the ring. The Raman amplifier is inserted into the ring as shown in Fig. 5.10.

An example of a measured pulse train consisting of 116 pulses, each 10 μs long, a seed laser power of 5 mW, and a pump laser power of 363 mW is shown in Fig. 5.11. together with the corresponding simulation. The graph shown in the figure represents an average over 200 pulse trains. Subfigures (a)-(c) show a close up of five pulses from the beginning, the middle and the end of pulse train together with the simulation (dashed line). The power has been normalized to the peak of the second pulse since this is the first pulse that has propagated through the ring. The first pulses are clearly not rectangular which, as previously discussed, is due to the finite response time of the input AOM. The pulse shape, however, rapidly changes and in the middle of the train the power of the leading edge is stronger than the power of the trailing edge. This effect is caused by depletion of the pump by the leading edge of the pulse, and because the pulse recirculates in the ring, the effect reinforces itself, leading to an ever larger difference between the leading and the trailing edges of the

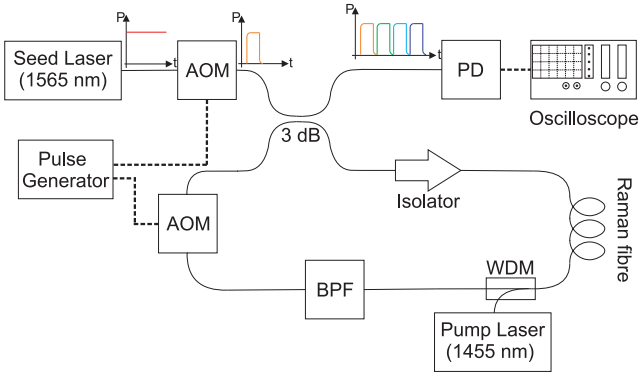

Figure 5.10: A sketch of the experimental setup. What separates this setup from the setup shown in Fig. 5.1 is the Raman amplifier consisting of an isolator, a high Raman gain optical fibre, a WDM coupler, and a pump laser.

pulses. This behaviour persists throughout the pulse train and is clearly seen in the last five pulses where the leading edge has grown to be stronger than, not only the trailing edge, but also the preceding pulses, and the trailing edge has correspondingly dropped. The simulation is seen to predict the measured pulse train well. This agreement between measurement and simulation was only achieved when including pump depletion in the simulations, hence it is concluded that this is the cause of the pulse shaping. Subfigure (d) shows a comparison of the envelopes of the measured (○) and the simulated (solid line) pulse train in their full lengths, and again the four points of comparison are used. In the beginning the three graphs, representing the pulse powers, are seen to decay slightly, but after around 0.8 ms the mean power and the peak power start to rise whereas the trailing edge continues to fall.This behavior of falling and then rising is consistent with what has earlier been described for the mean power in e.g. [49]. Also for the full length comparison, the simulation is found to fit very well with the measurement, but with a slight deviation toward the end. It is noticed that every other pulse is higher than the neighboring pulses. This phenomenon is especially pronounced for the peak of the pulses, but is not found in the simulations and it is thought to be due to a weak polarization dependence somewhere in the ring, probably in the amplifier. Apparent from the top panel of in Fig. 5.11. the bottom level is mainly resulting from the finite response time of the input AOM. However, this level allows the build up of ASE to be deduced because an increase in the power level at the bottom

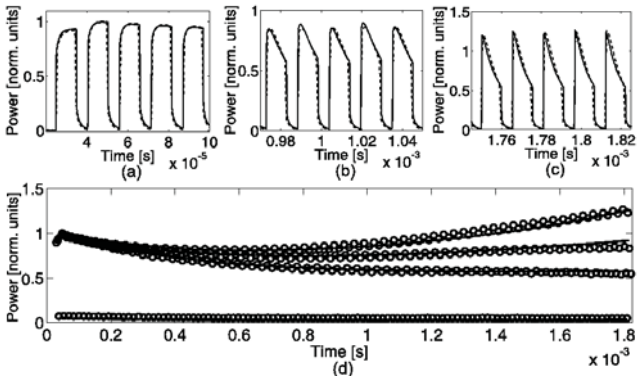

Figure 5.11: A pulse train consisting of 116 pulses, a seed laser power of 5 mW and a pump laser power of 363 mW. (a)-(c): Close up of five pulses in the beginning, the middle, and the end of the pulse train. Solid lines represent measured data and dashed lines simulated data. (d): Full length comparison of measured and simulated data for the bottom, the trailing edge, the mean, and the peak of the pulses. Solid lines represent simulated data and circles measured data.

must be attributed to the growth of ASE. In our pulse train the bottom level is flat and around $5 \cdot 10^{-2}$, in the normalized units and thus we can conclude that for this pulse train, ASE does not grow significantly before the pulse train is terminated.

Fig. 5.12. shows a pulse train where the seed laser power has been increased to 11 mW while all other parameters have been kept constant as compared to the pulse train in Fig. 5.11. Again the power has been normalized to the peak of the second pulse. It is clear from the close ups, both in the middle as well as in the end of the pulse train that the leading edge of the pulses grows up even more at the expense of the trailing edge than was seen in the first example in Fig. 5.11. The reason for this is that the shaping of the pulses caused by depletion of the pump becomes more pronounced with a higher signal. In contrast to Fig. 5.11. the pulse power fluctuates more in the beginning of the pulse train than in the end. The simulation does not replicate this and the overall agreement between measurement and simulation is not as convincing in the beginning of the pulse train as it was in the previous example. Toward the end of the pulse train, the fluctuations become less pronounced and the simulation agrees better with the measured. However, in the end of the pulse train where

the shaping of the pulses becomes very strong, the simulation cannot reach the same peak power as the measured and a deviation between the measured and simulated pulse train is visible. Once again the bottom level is flat but here with a slightly lower value of around $4 \cdot 10^{-2}$ normalized units.

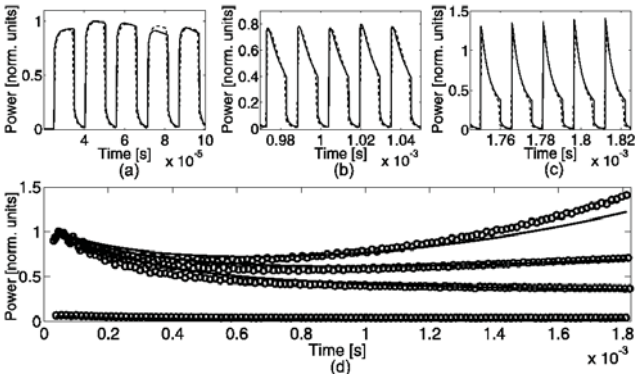

Figure 5.12: A pulse train consisting of 116 pulses, a seed laser power of 11 mW and a pump laser power of 363 mW. (a)-(c): Close up of five pulses in the beginning, the middle, and the end of the pulse train. Solid lines represent measured data and dashed lines simulated data. (d): Pulse train envelopes for the bottom, the trailing edge, the mean, and the peak of the pulses. Solid lines represent simulated data and circles measured data.

Aiming at applying the FSPT in a lidar, it is important to obtain as flat a pulse train as possible and therefore the number of pulses has been limited to 116. However, since noise does not seem to grow up, if a less flat pulse train envelope were acceptable, there should be nothing to hinder an increase in the number of pulses generated. Both the Raman amplifier as well as an EDFA work for this purpose. The problem with the Raman amplifier compared to the EDFA in respect to lidar measurements is the long pulses; 10 μs pulses corresponds to a range cell length of 3 km which is clearly too long for practical use. Shorter pulses would require considerably higher pump power or a fibre with an even higher Raman gain.

5.4 Summary

In this chapter the LSFS was presented as a method for generating an FSPT. The experimental setup was described and a brief explanation of the

working principles behind two of its key components the AOM and the fibre optical amplifier, was given. A model describing the FSPT as function of time from the literature was presented and implemented in Matlab. A more accurate description of the FSPT was achieved with a time dependent model incorporating the temporal dependencies of the amplifier. Two different types of fibre amplifiers the EDFA and the Raman amplifier were tested experimentally and in simulations. It was shown that they were both able to deliver the needed amplification and satisfactory pulse trains were obtained. It was seen that the shape of the individual pulses changed along the pulse train. This was ascribed to depletion of the amplifier pump. For use in a FSPT modulated lidar the pulses generated by the Raman assisted LSFS are too long so for this application the EDFA is the preferred amplifier. The simulations showed good agreement with experiments for both amplifier types and were able to replicate many features, although the simulation of the Raman assisted LSFS performed better. This can probably to a large extend be explained by the fact that most of the parameters in the EDFA simulations are not known in detail, and it would be a relevant test of the model to repeat the experiments with a different and better known amplifier.

CHAPTER 6

FSPT in the frequency domain

So far we have looked at the output of the lightwave synthesized frequency sweeper (LSFS) in the time domain. However, since the idea behind it all is to use the LSFS as light source in a lidar the spectral content and stability are just as important as temporal stability. In this section the spectra of the individual pulses in the frequency stepped pulse train (FSPT) are measured and the time independent model is further developed to incorporate parasitic noise induced by the two acousto-optic modulators (AOMs).

The work presented in this chapter has led to the publication of [65].

6.1 Noise due to AOM

As described in the previous chapters, build up of amplified spontaneous emission (ASE) is an important noise factor in the FSPT. In the models presented the spontaneous emission generated within the limits of the bandpass filter (BPF) is assumed spectrally flat. However, the AOMs additionally contribute to the noise through intermodulation products, leading to part of the power being either non- or double frequency shifted. Intermodulation products arise due to more than one acoustic frequency being present in the modulator, e.g. because of harmonics in the radio frequency (RF) signal feeding the AOM, as well as acoustic nonlinearities in the modulator [58]. These parasitic frequencies are amplified and frequency shifted during the subsequent revolutions, and over time they build up discrete noise components at integer multiples of the AOM RF frequency. In this section the time independent model of Section 5.2.1 is expanded to take non-shifted light into account.

Restricting ourselves to the case where the two AOMs only leak light

which is not frequency shifted Eqs. (5.4) and (5.5) transform into

$$P_s^{i+1}(\nu_s^i + \Delta\nu) = (1-\beta)L(\nu)G^i P_s^i(\nu) \quad (6.1)$$

$$p_{n,t}^{i+1}(\nu + \Delta\nu) = p_{n,\Delta\nu}^{i+1}(\nu + \Delta\nu) + p_{n,\beta}^{i+1}(\nu) + \varepsilon P_{\text{seed}}(\nu_s^0), \quad (6.2)$$

where $p_{n,t}$ is the total spectral noise density and

$$p_{n,\Delta\nu}^{i+1}(\nu + \Delta\nu) = (1-\beta)L(\nu)\Big[G^i p_{n,t}^i(\nu) + 2n_{sp}(G^i - 1)h\nu\Big], \quad (6.3)$$

$$p_{n,\beta}^{i+1}(\nu) = \beta L(\nu)\Big[G^i P_s^i(\nu_s^i) + G^i p_{n,t}^i(\nu) + 2n_{sp}(G^i - 1)h\nu\Big]. \quad (6.4)$$

Here β and ε is the fraction of light leaking through the open ring AOM and the closed seed AOM,respectively, without getting frequency shifted. P_{seed} is the power of the seed laser operating at a frequency ν_s^0. Eq. (6.3) thus describes noise which is frequency shifted in the given revolution and is the equivalent of Eq. (5.5), whereas Eq. (6.4) describes noise which is not shifted during that revolution. Eq. (6.4) further contains an additional term originating from the non-shifted part of the signal, P_s^i. Applying the constant output power approximation as in Section 5.2.1 the amplifier gain is found as

$$G^i = \frac{P_{\text{const}} + 2n_{\text{sp}}h(1-\beta)\int_0^\infty L(\nu)\nu\,\mathrm{d}\nu - \varepsilon P_{\text{seed}}(\nu_s^0)}{L(\nu_s^i)P_s^i + \int_0^\infty L(f)\left[p_{n,t}^i(\nu) + 2n_{\text{sp}}h\nu\right]\mathrm{d}\nu}. \quad (6.5)$$

6.1.1 Constant loop gain

Eqs. (6.2-6.5) describe the growth of noise originating from spontaneous emission as well as leakage from the two AOMs. The latter leading to parasitic frequency components at integer multiples of Δf in the RF beat spectrum. However, a much simpler expression describing the growth of noise may be obtained if we neglect the seed AOM leakage, ε, and furthermore assume a constant loop gain which is not affected by the growth of power at frequencies of previous signal frequencies. That means that the power in the signal peak remains constant as function of number of round-trips, even though the noise builds up. How these components grow as function of revolutions is outlined in Table 6.1.

In the first pulse only the pure signal is present with frequency ν_s^1. The second pulse has propagated the ring once and as a result the main signal is shifted $\Delta\nu$, but a fraction, β, has not and remains at the initial frequency. For the third pulse the main power is shifted to $\nu_s^i + 2\Delta f$, while the contribution at $\nu_s^i + \Delta\nu$ is the sum of leakage from the main signal and previous leakage

		Signal frequency →					
		ν_s^1	$\nu_s^1 + \Delta\nu$	$\nu_s^1 + 2\Delta\nu$	$\nu_s^1 + 3\Delta\nu$	$\nu_s^1 + 4\Delta\nu$	$\nu_s^1 + 5\Delta\nu$
↓ # rev.	0	P_s					
	1	$\beta \cdot P_s$	P_s				
	2	$\beta^2 \cdot P_s$	$2\beta \cdot P_s$	P_s			
	3	$\beta^3 \cdot P_s$	$3\beta^2 \cdot P_s$	$3\beta \cdot P_s$	P_s		
	4	$\beta^4 \cdot P_s$	$4\beta^3 \cdot P_s$	$6\beta^2 \cdot P_s$	$4\beta \cdot P_s$	P_s	
	5	$\beta^5 \cdot P_s$	$5\beta^4 \cdot P_s$	$10\beta^3 \cdot P_s$	$10\beta^2 \cdot P_s$	$5\beta \cdot P_s$	P_s

Table 6.1: Table illustrating how noise grows at specific frequencies due to AOM leakage as function of round-trips through the ring.

which is now shifted, and again a fraction β is leaked and remains at the initial frequency.

As seen from the table it is possible to continue in this manner for the desired number of revolutions, but a simple expression emerge if the position of the main signal is used as reference. This means that every frequency component is denoted according to how many frequency shifts it trails the main signal. The noise density may in this case be written as

$$p_n(i,k) = \frac{i!}{(i-k)!k!}\beta^k P_s, \text{ of frequency } \nu_s^1 + (i-k)\Delta\nu \text{ for } k \leq i, \quad (6.6)$$

where i is the pulse number and k represents the trailing components, e.g. $k = 2$ means the frequency slot $2\Delta\nu$ behind the main peak in pulse number i [65].

6.2 Comparison of the two models

The development of signal and noise is evaluated through an iterative numerical simulation using Eqs. (6.1-6.5), or alternatively the noise is calculated directly using Eq. (6.6) when applying the constant loop gain approximation. Inputs to the simulations are based on careful measurements of the actual physical setup as presented in Fig. 5.1. The optical bandpass filter transfer function is approximated by a Gaussian function with a 3 dB bandwidth of 0.84 nm and an insertion loss at the center frequency of 2.67 dB. The center frequency is assumed to be matched with the input frequency of the first pulse. All other loss components, e.g. connector losses or losses due to the 3 dB coupler, are assumed to be frequency independent, hence they may be simulated as a combined loss contribution of approximately 10 dB. The optical input power is

3.5 mW, the spontaneous emission factor, n_{sp}, is set to 6.31 based on measurements of the Erbium doped fibre amplifier (EDFA) noise figure (NF), and the frequency shift, $\Delta\nu$, induced by either AOM is 40 MHz. The seed leakage from the input AOM, ε, is set to -52.52 dB and β to -58.29 dB, see Section 6.3.

Fig. 6.1 shows a comparison based on Eqs. (6.2) and (6.6) of the growth of noise relative to the power in the main peak in the frequency slots trailing the main peak by one and two shifts. The results governed by the two different calculations are seen to give different results, particularly for the second trailing frequency slot. The two curves describing noise in the slots trailing by one frequency step are seen to follow each other quite closely but with the one based on Eq. (6.2) $2-3$ dB higher than the other. This is due to leakage from the seed AOM, ε, which in Eq. (6.6) is assumed to be zero, neglecting zero point fluctuations, but finite in Eq. (6.2). Note that the two curves approach each other with increasing pulse number. By contrast, the curves describing the second trailing slot appear qualitatively different. The curve based on Eq. (6.2) is almost completely flat on the scale used whereas the one based on Eq. (6.6) shows a similar shape to the one trailing by one frequency shift. Furthermore, the latter is 26 dB lower than the former at pulse number 170. This is again all due to leakage from the seed AOM which is not taken into account by Eq. (6.6), but in this case completely dominates in Eq. (6.2). The number of pulses in the simulations is actually limited by Eq. (6.6) due to its factorial dependence on pulse number, hence the maximum number of pulses on a standard desktop computer is 170.

6.3 Spectral measurement

To measure the spectrum of the individual pulses in the FSPT, a heterodyne measurement utilizing a balanced photo detector (BPD) and an electrical spectrum analyzer (ESA) is used, as shown in Fig. 6.2. To generate the FSPT a standard LSFS, as described in Chapter 5, is used with an 11 km single-mode fibre as delay line, resulting in pulses of approximately 50 μs in length. One percent of the seed laser power is split off before the ring and subsequently joined with the resulting pulses at the output side of the ring. This is the local oscillator (LO) which the pulses are beating against in the heterodyne process discussed in Chapter 2. In order to measure one and only one pulse at a time a time-gate is used. Every time a new pulse train is initiated a trigger signal goes to the ESA which then measures for a given length of time, e.g. 10 μs, and

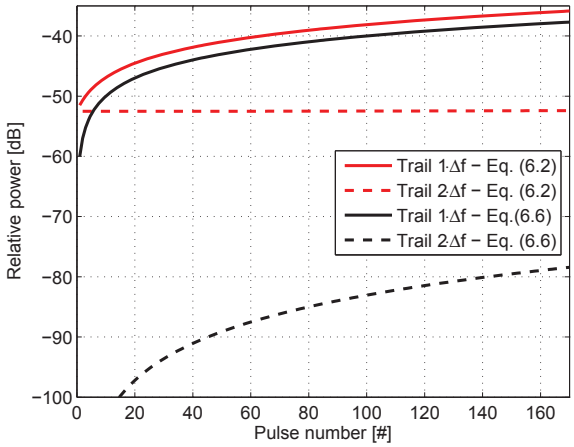

Figure 6.1: Development of noise at the frequency slots trailing the main signal frequency by one and two frequency shifts.

by changing the time between the trigger signal is received and the initiation of the measurement, one may measure all the pulses individually. The figure shows an additional 1% tap placed immediately after the 3 dB coupler. This is a test tap that can, be placed at any of the six points, ①-⑥, and thereby used for monitoring the pulses on their way through the ring.

The amount of light, β, leaking unshifted through the ring AOM is measured using an interferometric setup as shown in Fig. 6.3. From the measured electrical spectrum β is determined through the following calculations and by assuming that β is the same for the two AOMs [65]. The current generated in the photo detector (PD) is given by

$$I(t) = 2R\sqrt{P_S P_{LO}}\cos\left(\omega_{IF}t + \Phi_{IF}\right), \tag{6.7}$$

where R is the PD responsitivity, P_S and P_{LO} are the optical powers in the signal and the reference arm, respectively, and ω_{IF} and Φ_{IF} are the intermediate frequency and phase [24]. The optical powers at either of the photo diodes in the BPD are

$$P_{LO} = \frac{1}{4}P_{\text{seed}}, \tag{6.8}$$

$$P_{2\Delta\nu} = \frac{1}{4}(1-\alpha)^2 P_{\text{seed}}, \tag{6.9}$$

$$P_{\Delta\nu} = \frac{1}{4}(1-\alpha)\beta P_{\text{seed}}, \tag{6.10}$$

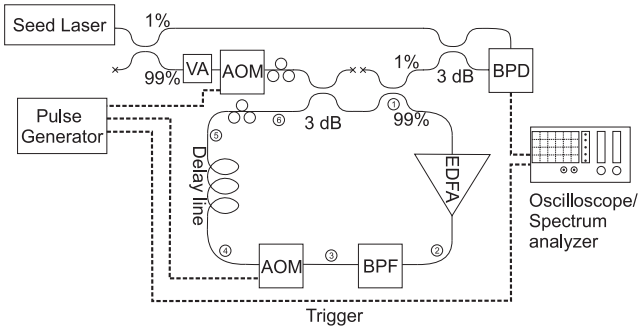

Figure 6.2: Sketch of the setup used for measuring the spectra of the individual pulses.

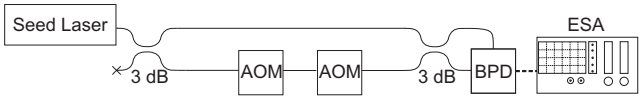

Figure 6.3: Setup for measuring the non-frequency shifted fraction β.

where α is the insertion loss of the AOMs which is here assumed to be identical for the two modulators. The power is divided by four due to the two couplers and it is assumed that interference of the components with the same frequency originating from the two AOMs over the detection time averages the optical power on the detector according to $\frac{1}{2}P_1P_2$. Since the electrical power, S, measured by the spectrum analyzer is proportional to the square of the current we can write

$$S_{2\Delta\nu} = 2R^2 P_{\Delta\nu} P_{LO} = \frac{1}{4} R^2 (1-\alpha)^2 P_{\text{seed}}^2 \tag{6.11}$$

$$S_{\Delta\nu} = 2R^2 P_{2\Delta\nu} P_{LO} = \frac{1}{4} R^2 (1-\alpha)\beta P_{\text{seed}}^2, \tag{6.12}$$

where R is the detector responsivity assumed to be the same for the two detectors. The ratio between the electrical powers at frequencies $\Delta\nu$ and $2\Delta\nu$ then leads to

$$\begin{aligned} \frac{S_{\Delta\nu}}{S_{2\Delta\nu}} &= \frac{\beta}{(1-\alpha)} \Leftrightarrow \\ \beta &= \frac{S_{\Delta\nu}}{S_{2\Delta\nu}}(1-\alpha). \end{aligned} \tag{6.13}$$

The same analysis can be made for other frequency components e.g. at 120 MHz.

The electrical spectrum is shown in Fig. 6.4 and it seen that most of the power is located at 80 MHz as expected with a peak height of 0.715 dBm. There are, however, distinct peaks at 40 MHz and 120 MHz with peak heights of -56.2 dBm and -67.2 dBm, respectively, and these must be due to light which is either non- or double-shifted in one of the modulators. A fourth peak seen at 160 MHz is the first harmonic of the main signal generated in the detector and is therefore not optical in origin even though there might be a weak optical signal at that frequency as well. The peak around 107.5 MHz is background noise. The insertion losses for the two modulators were measured with an optical powermeter as 1.32 dB and 1.36 dB, and are as assumed practically identical. Using Eq. (6.13) and the average insertion loss the leakage coefficient, β, is found to be -58.3 dB or $1.48 \cdot 10^{-6}$ in linear units and the equivalent at 120 MHz -69.2 dB or $1.19 \cdot 10^{-7}$. Note that the 40 MHz peak is an order of magnitude higher than the 120 MHz peak justifying the restriction of Eq. (6.2) to consider only the non-shifted part.

The leakage coefficient through the closed AOM, ε, is measured in the same way as the insertion loss and found to be -52.5 dB and -47.5 dB for the two AOMs. This leaked light is not frequency shifted.

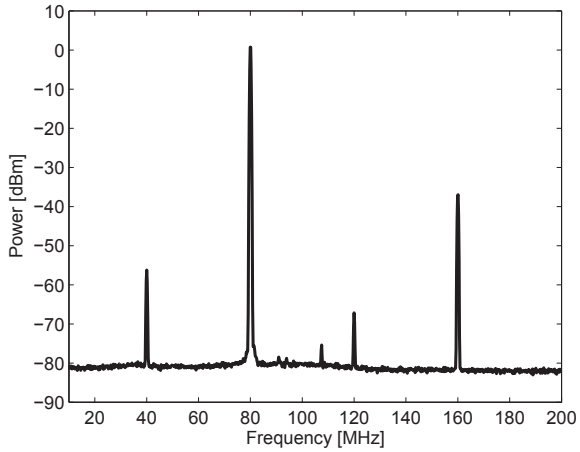

Figure 6.4: The electrical beat spectrum used for determining the leakage coefficent β.

Fig. 6.5 shows an example of a pulse train generated by the LSFS and

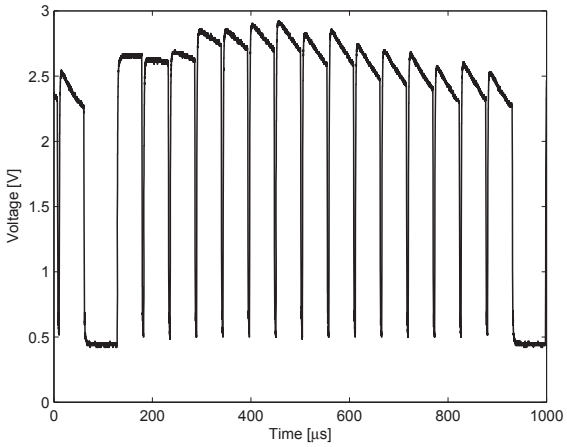

Figure 6.5: Temporal measurement of the pulse train consisting of 15 pulses each 50 μs long. Note that the pulses become more and more distorted, just like the pulses generated by the Raman assisted LSFS.

used for spectral analysis. The data sampling is performed using an InGaAs photodetector and a digital oscilloscope. The optical power is therefore expressed in units of Volts. The train consists of fifteen individual pulses, each 50 μs long. As seen the first pulse in the train is relatively flat, but already the second pulse shows a tendency of the trailing edge of the pulse being lower than the front edge. As discussed in Section 5.3.2 this is due to depletion of the amplifier and it is an effect which reinforces itself leading to ever larger differences between the leading and trailing edges throughout the pulse train [53]. In between the pulse trains as well as between the individual pulses, the voltage does not drop to zero. This is mainly due to the constant background transmitted directly from the laser to the detector and used as LO in the beating process. Build-up of ASE also contributes to the non-zero voltage between pulses, but with the train terminated after only 15 pulses this effect is negligible. The envelope describing all 15 pulses is seen to be relatively flat which indicates that the constant output power approximation used in the time independent model (Eq. 6.2) is valid.

Fig. 6.6 shows the spectrum of the eleventh pulse in the pulse train measured from 10 MHz to 640 MHz with a resolution bandwidth of 390 kHz. The main peak is readily seen at 440.0 MHz, in excellent agreement with eleven frequency shifts of 40 MHz, and a peak of -3.23 dBm. This peak is very

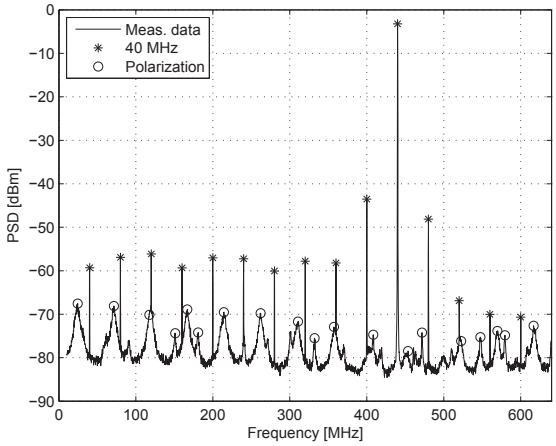

Figure 6.6: Spectrum of the eleventh pulse. The main peak at 440 MHz is clearly visible, but so are a number of other peaks due to non- or double shifted light a integer multiples of 40 MHz.

narrow with a 3 dB width less than the resolution bandwidth of the measurement owing to the narrow linewidth of the seed laser. Beside the main peak, two distinct features stand out in the spectrum. The first of these are the narrow peaks equidistantly separated on either side of the main peak and marked using stars $(*)$. The spacing between these peaks is 40 MHz, strongly indicating that they are related to the AOMs, i.e. light that is either non- or double shifted in frequency during transmission through the modulator. Most prominent of these are those two immediately next to the main at 400 MHz and 480 MHz with peak values of -43.5 dBm and -48.1 dBm, respectively. Below 400 MHz the hight of these peaks lies between -60 dBm and -56 dBm, but with small variations which seem to repeat themselves for every 120 MHz. A satisfactory explanation for this periodicity has not been found, but speculative possible causes are that something in the averaging leads to the spectrum shown or perhaps that it is somehow related to the pulse shape which, as seen in Fig. 6.5, becomes more and more sawtooth shaped. For frequencies higher than the main peak the height of the peaks gradually decreases, but they are nevertheless visible in the entire measured spectrum. In a lidar measurement these peaks will act as relative intensity noise (RIN) in the middle of every frequency slot, thus decreasing the sensitivity at low wind speeds. The second distinct feature is a series of low but much wider peaks which have been

marked with circles (○) to help guide the eye. The first of these is centered around 24.4 MHz and has a 3 dB width of approximately 6 MHz. The following peaks are of similar width and separated by about 48 MHz, but their height tends to decrease slightly at frequencies closer to the main peak.

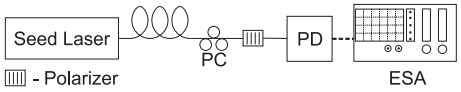

Figure 6.7: Setup for investigation of laser beat spectrum. Light from the seed laser is propagated through a length of fibre and then polarization filtered. The PC is used to control the polarization of the light entering the polarizer. The self-heterodyne spectrum is measured with a PD and an ESA.

In order to find the cause of the circled peaks, a simple setup was established as shown in Fig. 6.7. The seed laser is first launched into the 11 km single-mode fibre (SMF) used in the LSFS at this stage, and into a PC and a polarizer. The PC is used to align the output polarization with the polarizer by maximizing the input power on the PD, and the self-heterodyne beat spectrum is finally measured with the ESA. The procedure is then repeated but this time with the polarization misaligned compared to the polarizer and therefore a lower power emitted to the detector. An oscilloscope measures the power at the detector, which is therefore expressed as a voltage. The power levels are 8.5 V and 6.5 V for the aligned and misaligned case, respectively. The resulting spectra are shown in Fig. 6.8 and it is clearly seen how peaks are present when the polarization is misaligned with the polarizer but completely absent when the polarization is aligned. The peaks arise when the light at the detector is intensity modulated and this modulation is induced by the polarizer. It is therefore concluded that the peaks must be related to beating between different polarization states propagating in the 11 km delay fibre. The frequency spacing between the peaks in this spectrum is 30 MHz. The frequency spacing is obviously narrower than what was observed in the spectrum of the eleventh pulse; in that case, however, the configuration is much more complex and the light is affected by various components and is hence not directly comparable with the simple setup in Fig. 6.7.

Different possible explanations have been considered for the polarization related peaks. One is to regard the fibre as an interferometer where two polarization states propagates with different speeds due to the inherent birefringence in the fibre. In this picture we can calculate the polarization beat length given

by a specified frequency spacing, $\Delta\nu$, as

$$L_B = \frac{c}{\Delta\nu\,(n_x - n_y)}, \tag{6.14}$$

where c is the speed of light, and n_x and n_y are the refractive indices of the two orthogonal principal axes [59]. Using a frequency spacing of 30 MHz and an index difference of 10^{-5}, leads to a beat length of 1000 km, which obviously can not be correct as it is much longer than the fibre used and furthermore the typically beat length of standard SMFs is about 1 m. Thus the frequency spacing is too small to fit this explanation. Another speculative cause for the observed peaks which has been considered is to regard the system as a Fabry-Pérot etalon and the frequency spacing can then be transferred into a cavity length through

$$L = \frac{c}{2n\Delta\nu} \tag{6.15}$$

By using the 30 MHz frequency spacing and $n = 1.45$ the cavity length becomes 3.44 m which is actually comparable to the polarization beat length of typical SMF [59]. However, the problem with this explanation is that there is no 3.44 m cavity in the setup.

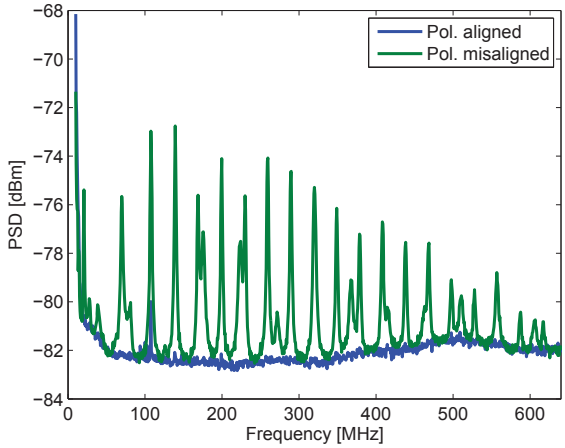

Figure 6.8: Self-heterodyne spectra of light propagated through 11 km of fibre and the polarization filtered as shown in Fig. 6.7. For the blue curve the polarization of the light exiting the fibre is aligned with the polarizer and for the green curve the polarization is misaligned.

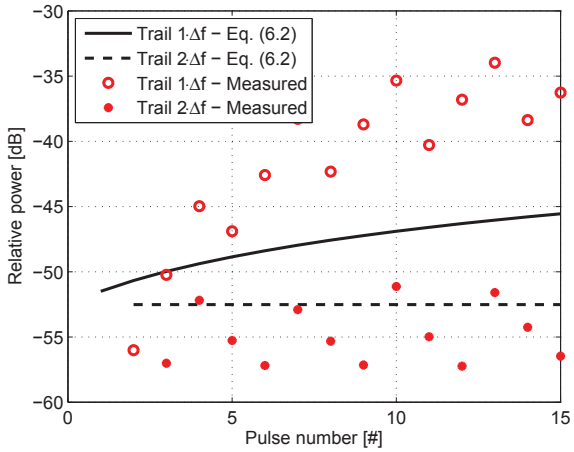

Figure 6.9: Development of noise at the frequency slots trailing the main signal frequency by one and two frequency shifts, measured and simulated.

As was the case with Fig. 6.1, Fig. 6.9 shows the development of the first two trailing components, but this time comparing measured data with simulations based on Eqs. (6.1-6.5) as this model includes ε. The same input parameters to the simulations as in Fig. 6.1 has been used. Again a periodicity over 120 MHz is seen in the measured data, but there is also a clear difference between the frequency components trailing by one shift compared to the components trailing by two shifts. For the former the peak height increases over two pulses whereafter it drops and the pattern is repeated. For the latter the opposite is the case. Here the peak height first decreases two times and then increases. When comparing with the simulation the same general tendency in the growth of the noise is seen. The components trailing one slot are growing as function of pulse number, whereas the components trailing two slots are dominated by leakage from the seed AOM and seem almost totally flat. However, the measured noise grows faster than predicted by the simulations and attempts to overcome this by increasing the value of β proved futile.

6.4 A different application of the LSFS

One of the distinct features of lasers in general is that they are nearly perfectly mono-chromatic or in other words have narrow linewidths. The linewidth is fundamentally limited by spontaneous emission even though it

is often other phenomena, such as mechanical vibrations or pump instabilities which define the linewidth of real lasers [66]. One way to measure the linewidth is to use an interferometer, i.e. spliting the light in two separate paths and measuring the electrical beat spectrum when recombining the light in a PD. Fibre lasers, however, often have linewidths even down in the sub-kilohertz range and with this narrow lasers measuring the linewidth can become a challenge. The problem is that the light must be uncorrelated in order to measure the correct linewidth and this requires the difference in path length in the two arms of the interferometer to be longer than the coherence length of the laser. With coherence lengths of narrowband lasers sometimes of the order of tens of kilometres it can therefore be troublesome first of all to transmit light the required distance without too much loss of power, and secondly to ensure that the light is totally uncorrelated. In [67] it was suggested that both these problems can be solved using a setup similar to the LSFS but without the seed AOM. In this way the ring is thus continuously seeded and the output will be continuous as well but containing a comb of frequencies separated by the AOM frequency shift. In the beat spectrum these frequencies will stand out as peaks and by measuring the width of these one can find the laser linewidth. The center frequency of each peak represents the difference in carrier frequency and thereby also the difference in optical path length that the two light waves have travelled. The first peak is beating of light separated by only one round trip and thus one ring length which is probably not enough for them to be uncorrelated and the peak will therefore be narrow. However, going to higher and higher beat frequencies the light will be more and more uncorrelated and the peaks wider and wider, and when the peak widths approaches a constant level, the coherence length has been exceeded and the linewidth is then found as half the peak width [68].

In addition, the matter is further complicated when applying this technique to a fibre laser. The frequency noise of fibre lasers is not white but dominated by 1/f-noise which in the beat spectrum manifests itself as an approximately Gaussian broadening of the laser line. The measured spectrum is therefore a convolution of the Lorentzian spectrum of the natural laser line and the Gaussian spectrum of the 1/f-noise also known as a Voigt profile which is calculated from

$$V(a,u) = \mathrm{Re}\left[W(z)\right], \qquad z = a + iu, \tag{6.16}$$

where $W(z)$ is the complex error function and

$$a = \frac{\sqrt{\ln 2}\Delta\nu_L}{\Delta_G}, \tag{6.17}$$

$$u = \frac{2\sqrt{\ln 2}\,(\nu - \nu_c)}{\Delta\nu_G.} \tag{6.18}$$

Here $\Delta\nu_L$ and $\Delta\nu_G$ is the full width at half maximum (FWHM) of the Lorentzian and Gaussian, respectively [69]. The Gaussian linewidth depends on the delay length even for very long delays [70, 71] and will thus continue to increase when extending the delay. Two different techniques have been suggested to dig out the Lorentzian linewidth from underneath the Gaussian, and one is a nonlinear least squares fitting of the Voigt profile and the other is, if possible, to use the 20 dB width of the peak [70, 72]. The assumption underlying the latter technique is that due to the wide flanks of the Lorentzian this will dominate the spectrum far away from the center and the linewidth is then calculated from

$$\Delta\nu_L = \frac{\Delta\nu_{RF,20\ dB}}{2\sqrt{99}}, \tag{6.19}$$

where $\Delta\nu_{RF,20\ dB}$ is the 20 dB width of the beat spectrum.

To test the technique and at the same time to find the linewidths of the two lasers used in this project, the seed AOM was removed from the LSFS and the linewidth measuring setup thus established with a 11 km fibre as delay line. Each of the resulting peaks in the beat spectrum were measured using an ESA in a bandwidth of 800 kHz and Fig. 6.10 shows an example together with a fit of a Gaussian and a Voigt profile. The peak shown in the figure is centered around 320 MHz, thus representing beating of light with a path difference of 88 km. The peak is clearly well approximated by a Gaussian and the laser is thus dominated by 1/f noise as expected. The Voigt profile, however, fits the spectrum even better which is seen on the flanks of the peak. These wide flanks are a result of the underlying Lorentzian line shape, and Fig. 6.11 shows the measured FWHM Lorentzian width of the Voigt fit and on the 20 dB width, described above, and for both of the two lasers used. Fig. 6.11(a) shows the width of the 1565 nm laser and it is seen that the width based on the Voigt fit seems to flatten and approach a constant level of about 15 kHz after seven round-trips through the ring, or 77 km, whereas the 20 dB on the contrary just seems to increase linearly. The latter is also much wider starting around 16 kHz and growing to 36 kHz for twelve revolutions. The same general trend applies for the 1548 nm laser (Fig. 6.11(b)), though the constant level of the

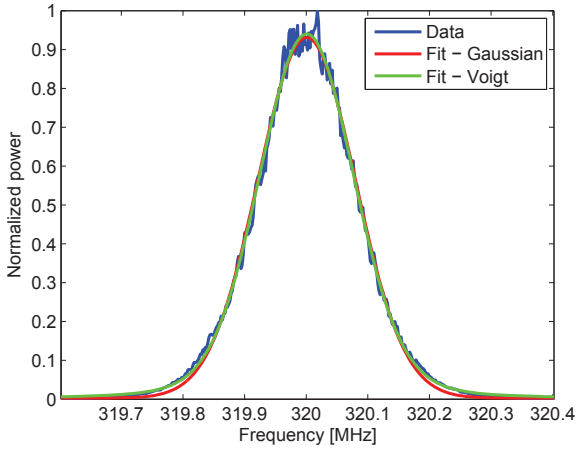

Figure 6.10: Plot of the beat spectrum around 320 MHz for the 1565 nm laser together with a least squares fit of a Gaussian and a Voigt profile. The peak is clearly very close to being Gaussian but is nevertheless better approximated by the Voigt profile due to the long tails.

Voigt fitted Lorentzian width of around 8 kHz is less sharply defined. The linewidth of the lasers is simply specified by the manufacturer to be lower than 50 kHz for both lasers [73]. The measurements here obviously support this. The different values found with the two methods can thus not be verified. However, only fitting to a proper Voigt function fulfils the expectation of a width approaching a constant value as the coherence length is exceeded.

Measuring the linewidth of narrowband fibre lasers accurately and not least interpreting the measurements correctly is a complicated matter and not within the scope of this project. Therefore we will not pursue further verification of the obtained linewidths, but complete this section by concluding that the measurements carried out show promising potential for an LSFS operated in continuous wave (CW) mode for determination of very narrow laser linewidths.

6.5 Other frequency swept light sources

The LSFS is not the only way for generating a frequency swept laser output; other methods exist and in all-fibre configurations as well. One simple way is to use a piezoelectric actuator to stretch or compress the fibre Bragg

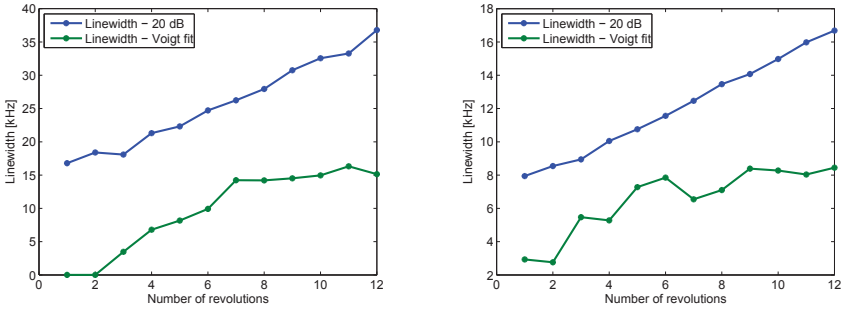

Figure 6.11: Measured linewidth as function of number of revolutions in the ring for (a) the 1565 nm laser and (b) the 1548 nm laser. The blue and the green curve represents the linewidths found based on the 20 dB width and fitting of a Voigt profile to the beat spectrum, respectively

grating (FBG) constituting the reflectors defining the laser cavity in a fibre laser. This will change the dominating laser mode and the wavelength thus be shifted. The output of the laser during tuning of the frequency will lead to range ambiguities in the lidar measurement, and thus needs to be blocked. This can be achieved with an amplitude modulator, e.g. an AOM. The usability of this technique in an FSPT modulated lidar depends on how fast the frequency can be changed and stabilized.

An example of a more recent swept source is a laser which utilizes a fibre optical parametric amplifier with a swept pump [74]. The parametric amplifier works utilizes the nonlinear process called four-wave mixing (FWM) in which the pump amplifies a signal but also generates an idler at a frequency satisfying the relation

$$\omega_{\mathrm{pump}} - \omega_{\mathrm{idler}} = \omega_{\mathrm{signal}} - \omega_{\mathrm{pump}}, \tag{6.20}$$

[59]. Hence, signal and idler are placed symmetrically around the pump. The pump in the proposed scheme is a supercontinuum pulse which is temporally broadened by transmission through a dispersive medium, e.g. an optical fibre, resulting in a mapping of the spectrum of the pulse into the time domain and a swept pump is created. Since the pump is swept, the frequency of the idler resulting from the parametric process can be controlled by controlling the time at which the signal pulse is injected into the amplifier, and injecting several pulses one after the other will generate an FSPT. There is, however, the implication that since the pump is continuously swept the pulses generated will be

chirped and if used as light source in a lidar range ambiguities are introduced. Furthermore, the pulses generated in this way are very short, in the order of picoseconds, complicating the data processing.

6.6 Summary

In this chapter we have investigated the spectral content of the pulses generated by the LSFS. As expected the frequency shift induced by the ring AOM led to a very stable frequency sweep. As an example, it was shown that after eleven revolutions the frequency had been shifted 440 MHz with high accuracy. However, the spectra also distinct noise components at frequency shifts equivalent of integer multiples of the AOM shift, $\Delta\nu$. This was ascribed to light leaking unshifted through the AOM and two different descriptions of how these noise components build up were developed. Both these models predicted qualitatively the same growth in noise but were not able to replicate the exact noise levels.

Finally it is shown how a same setup very similar to of the LSFS can be used for measuring the linewidth of narrowband fibre lasers.

CHAPTER 7

Wind speed measurements with an FSPT modulated lidar

In this chapter the lightwave synthesized frequency sweeper (LSFS) is coupled to a lidar system and used as light source for the frequency stepped pulse train (FSPT) modulated lidar. As mentioned in Chapter 2 the positive result of a proof-of-principle campaign was presented in [31], but in that campaign light was backscattered from a rotating cardboard disc i.e. a hard target measurement. In this chapter we present actual wind speed measurements obtained with the FSPT modulated lidar. The lidar system used is originally a monostatic continuous wave (CW) lidar and a few modifications have therefore been necessary. These modifications are described together with the data processing procedure that has been developed in order to retrieve meaningful data. The development of a working FSPT modulated lidar has been a long process and sometimes with no or only little progress. This is attempted illustrated through presentations of measurements obtained by approximately six months separation during 2011.

The work presented in this chapter has resulted in the publication of [75, 76].

7.1 Setup

The lidar system to which the LSFS is coupled is an early prototype of what has evolved into the *ZephIR* CW wind lidar [6]. It is owned by DTU Risø and has been modified to work with the LSFS as light source. The system in its original form consists of a base unit and a transceiver unit connected by approximately 10 m of cables; electrical as well as optical. The base unit

contains a narrowband fibre laser and an Erbium doped fibre amplifier (EDFA) for generating the signal, and photo detector and electronics for converting the optical signal into a digital electrical signal. Data processing such as discrete Fourier transform (DFT) is carried out with a PC. The transceiver unit is responsible for focusing the laser beam in the desired target range and collecting the backscattered light. This is done using a 7 cm diameter lens with a focal length of 28 cm and an accurate stepper motor which can move the delivery fibre back and forth behind the lens. A fibre optical circulator placed inside the transceiver directs light from the transmitting path to the delivery fibre, and collected backscattered light to the receiving path leading to the detector. The output fibre of the circulator constitutes the delivery fibre. This fibre is kept short, 10 cm, in order to avoid excess noise as was explained in Section 3.2. The local oscillator (LO) is generated from the end-facet reflection of the delivery fibre which is polished in an angle ensuring the optimum LO power at the detector. For measuring a background or noise spectrum a metal plate can be slid in front of the delivery fibre to shut off the output from the telescope.

Because the prototype is based on fibre optical components it is easy to disconnect the signal laser and connect the output fibre of the LSFS instead. Fig. 7.1 shows in a schematic form the entire lidar system separated into the optical domain (top), analog electrical domain (middle), and digital electrical domain (bottom). The optical part of the system is the same as for the CW lidar with the obvious exception that the single-frequency laser operating at 1548 nm is replaced by the LSFS. Instead the laser is used to seed the LSFS as illustrated in Fig. 5.1. The post EDFA used to boost the signal power naturally tends to influence the overall envelope of the FSPT, but this can in general be compensated with the optical bandpass filter (BPF) and the EDFA in the ring. In this way a flat output is obtained as long as the number of pulses is kept relatively low to around twenty.

The photo detector (PD) converts the optical signal into an analog electrical signal. This signal is initially filtered by a $0 - 190$ MHz low pass filter, in principle allowing for the first five range cells to be measured. There is additionally the possibility of highpass filtering of the signal which is normally done for CW lidars to eliminate the contribution to the noise floor added by relative intensity noise (RIN). However, the temporal response of the 100 kHz filter the system is born with, is not fast enough to respond to the highly dynamical pulse train and the filter is therefore removed from the system. It is, however, a possibility to use a highpass filter with a higher cut-off frequency e.g. 20 MHz in order to eliminate the difference between top and bottom of the pulses in the FSPT. This will be discussed in greater detail in Section

7.1.2. The final step at the analog level is the analog to digital conversion performed by the analog-to-digital converter (ADC), or digitizer with a sampling frequency, f_s, of 400 MHz equivalent to a Nyquist frequency of 200 MHz fitting well with the cut-off frequency of the low pass filter. The digitized data is temporarily stored in a buffer and when the buffer is full the data is passed to the PC for further data processing. During the processing data sampling is paused.

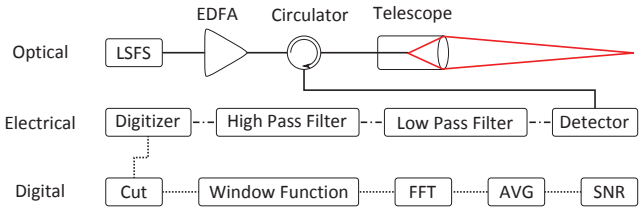

Figure 7.1: Block diagram of the FSPT modulated lidar separated into the optical (top), analog electrical (middle) and, digital electrical (bottom) parts of the system.

7.1.1 Data processing

The data processing of an FSPT modulated lidar signal includes a few more steps than the processing of a conventional CW lidar signal; especially, accurate time gating is important. For this task a programme has been written in the development environment *LabView*. The programme was developed to function in combination with the already existing control software of the lidar so that e.g. also focus range can be controlled through the same graphical user interface.

The time between pulses contains no information about wind speed and the first step in the data processing is therefore to cut away these periods from the time series and thereby separate each individual pulse. This is done based on knowledge about the pulse length and interpulse time which is manually fed to the data processing programme. The alternative would be to let the computer search the data string to identify the pulses, but this increases the processing time. Next step is to apply a window function to each pulse before it is digitally Fourier transformed. The default window is a rectangular or top hat function, but others such as cosine, Hann, or Hamming windows may be chosen [77]. The windowed pulses are then Fourier transformed via LabView's built in fast

Fourier transform (FFT) algorithm and the power spectrum calculated as the absolute square of the DFT. The length of the DFT can be chosen freely but often a 512 point DFT is chosen leading to a bin width of 781 kHz with a sampling frequency of 400 MHz. A 1 μs pulse sampled at 400 MS/s is resolved in 400 points and the time series is therefore zero padded to reach the 512 points of the DFT. This is done automatically by the FFT algorithm. In reality the useful part of the pulse is shorter than 1 μs due to the rise time of the acousto-optic modulator (AOM) and thus consist of fewer than 400 points. Finally, all the resulting power spectra are averaged and then normalized to a background power spectrum measured with the shutter closed.

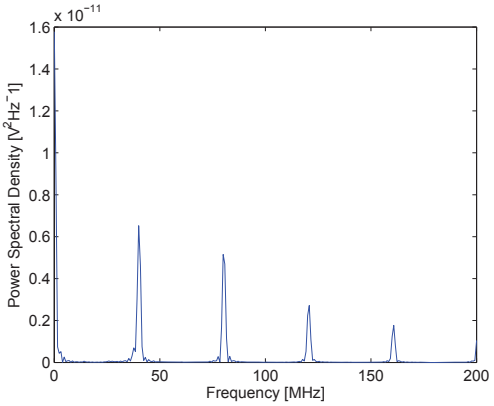

Figure 7.2: Raw spectrum of an FSPT modulated lidar signal sampled at 400 MS/s and calculated using a 512 point DFT, leading to a bin width of 781 kHz. Clearly seen are peaks at 40 MHz, 80 MHz, 120 MHz, and 160 MHz resulting from non-shifted leakage in the ring.

Fig. 7.2 shows an example of a raw spectrum from an FSPT modulated lidar. Most noticeable are the distinct peaks separated by 40 MHz from 0 MHz all the way up to 200 MHz. These are due to non-shifted light in the LSFS as discussed in detail in Chapter 6, but note that in the present case the pulses are beating against themselves and not a fixed LO, and therefore the main signal is found at 0 MHz and light trailing by one frequency shift at 40 MHz and so on. These peaks can lead to a degradation of the signal to noise ratio (SNR) in the centre of the frequency slots, thus impeding the measurement of low wind speeds [65]. Also seen are small peaks on either side of the larger peaks. These are due to spectral leakage and arise in the DFT [77]. They can be reduced by

applying a window function, e.g. a cosine-window.

7.1.2 Highpass filter

As seen from the measurements presented in Chapter 5 the pulse trains in the temporal domain are highly dynamic with a large difference between the power levels of the top and bottom of the pulses, constituting a challenge for the wind speed measurement. Any wind signal will lie on the top of the pulses and for this reason it is critical to resolve this part of the time series very precisely. The digitizer has a fixed ratio between the dynamic range on the voltage scale and the resolution of this, implying that for achieving a higher resolution it is necessary to decrease the voltage span, i.e. "zoom in" on the top of the pulse train. This again requires a very flat and stable pulse train output, a requirement that is in general not met by the pulse trains generated with the current LSFS; at least to the degree that is needed. Fig. 7.3(a) illustrates the situation with an FSPT which after being post amplified is not flat. Decreasing the dynamic range on the digitizer risks to lead to some of the pulses not being detected. The problem here actually concerns stability rather than the instantaneous envelope shape because it tends to change considerably over a time scale of a few minutes after which it is necessary to readjust the BPF, polarization controller (PC) and ring amplifier.

One way to circumvent this problem is to insert a highpass filter in the setup after the low pass filter as shown in Fig. 7.1. The filter should have a cut off frequency high enough to filter out the fluctuations in the pulse train caused by the difference between top and bottom of the pulses. The pulse repetition rate within the FSPT is about 800 kHz but the down time between pulses is 0.25 μs, leading to frequencies of around 4 MHz, and also the steep flanks of the pulses generates high frequency components, all of which must be removed. A filter with a stop band stretching up 20 MHz and a pass band which starts at 27 MHz has therefore been employed. This of course leads to the drawback that the first frequency slot is completely removed from the measurement.

Fig. 7.3(c) shows the FSPT after the electrical signal has been highpass filtered. It is seen how the DC component has been eliminated and the voltage fluctuations are now centered around 0 V while the voltage span is reduced from 2.5 V to 0.2 V compared to the unfiltered pulse train. It turns out that it is in general possible to use a 0.5 V span for the unfiltered FSPT but 0.2 V when the highpass filter is applied. The figure also reveals large spikes at the beginning of each pulse reaching beyond the limits of the plot though. These

are the temporal response of the filter to the FSPT dynamics. In Fig. 7.3(d) a close-up on one pulse shows that the spikes causes oscillations stretching into the pulse in a ringing effect leading to corrupted data in that part of the pulse and in practice it can be necessary to disregard this part in the data processing.

Even if the highpass filter is not applied it is necessary to remove the DC component from each pulse before doing the DFT. Another method for this is to apply a digital filter by fitting a function, e.g. a polynomial, to the top of the pulse and subsequently subtract it. This does not solve the problem with the dynamic range though, and it is furthermore quite demanding computerwise thus increasing the data processing time. In practice this approach leads to a processing time of several minutes for an amount of data equivalent to what can be stored in the digitizer buffer. Another difficulty of this method is to find a suitable function to fit after. A low order polynomial might lead to a poor fit while a higher order polynomial might lead to some of the wind induced oscillations in the time series be filtered out.

7.2 Wind speed measurements

The FSPT modulated lidar has been tested concurrently with different changes made to the setup and data processing procedure. In the following three different measurements are presented in chronological order together with the modifications made to the setup leading from one measurement to the next. Direct comparisons between the different measurements are difficult though as they are not performed at the same time or even day and therefore reference CW lidar measurements are used. All three measurements have in common that they are performed in atmospheric conditions with a high backscattering coefficient, i.e. in hazy but still quite windy weather. This is because at the present state the FSPT modulated lidar is still not capable of measuring in all atmospheric conditions and some of the reasons for this will be discussed at the end of the section.

7.2.1 First wind speed measurement

The first successful wind speed measurement was obtained with no external electrical filters. The output power is set to approximately 1 W and the electrical signal digitally filtered, i.e. fitted with a fifth order polynomial to filter out the DC component as described in Section 7.1.2. This means that every measurement takes two to three minutes, or rather between measurements there is a period of a couple of minutes where data is being processed. Data is

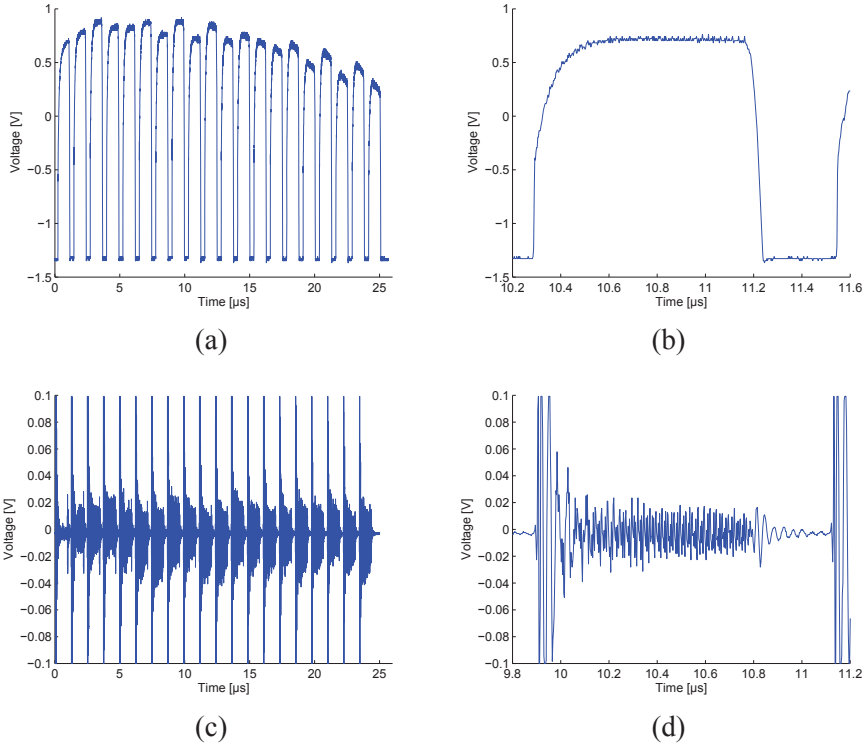

Figure 7.3: (a) FSPT consisting of twenty 1 μs pulses measured with the photo detector in the lidar. (b) Close-up of the ninth pulse. (c) highpass filtered FSPT. (d) Close-up of the highpass filtered FSPT. It is seen that ringing stretches about 0.2 μs into the pulse.

stored in the digitizer buffer in a single array making it sensitive to drift in the trigger signal. We shall return to discuss this issue and how to improve this in Section 7.2.3 The pulse trains generated consist of twenty 1 μs pulses which means that about 205 trains are sampled before the buffer is full and data is passed to the computer for further processing. The telescope unit is placed on a tripod with the beam pointing upward in an angle of approximately 45° compared to horizontal and the beam focused at 180 m which is in the center of the second range cell. Fig 7.4 shows the calculated weight functions of the first three range cells, and it is seen how the second cell is expected to dominate. The full width at half maximum (FWHM) of the second range cell is 36 m.

Fig. 7.5(a) shows an example of the measured spectra normalized to a

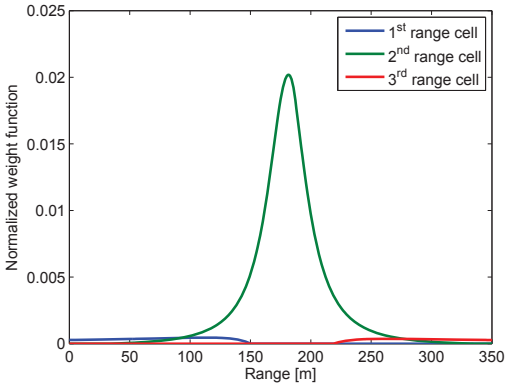

Figure 7.4: Spatial weight function of the first three range cells normalized to the area of the second range cell weight.

background measured with the shutter closed. A peak is clearly seen in both the first and the second frequency slots, the first of these at 4.71 MHz and the second at 46.27 MHz. By using Eq. 2.16 this is equivalent of an line-of-sight (LOS) wind speed of 3.64 ± 0.30 m/s and 4.85 ± 0.30 m/s, respectively. The uncertainty stated is equivalent of half a bin width on either side. The SNR values of the wind peaks are 3.46 and 2.18, respectively, and very different from what was expected from Fig. 7.4. A possible explanation for this disagreement relates to the attenuation of the laser pulses as they move through the air. The fact that the weather was hazy at the day of the measurement supports that backscattered light from the second range cell can have been attenuated relative to the first range cell. For reference Fig. 7.5(b) shows a measurement done with the lidar in CW mode, but focused at 260 m, and the Doppler shift of 6.27 MHz is in good agreement with the FSPT measurements. On the other hand, the SNR value of 33.2 is an order of magnitude higher than the highest peak seen in Fig. 7.5(a) even though the focus point lies much further away. The lidar is thus obviously more sensitive when operated in CW mode. Also noticed are the ripples in the noise floor in the centre of the frequency slots, i.e. at 40 MHz, 80 MHz, and 120 MHz. These are due to light leaking non-shifted through the ring AOM as described in Chapter 6, leading to peaks in the raw spectrum as shown in Fig. 7.2. If these peaks changes between the reference measurement and the actual measurement the noise floor of the normalized spectrum will not come out completely flat. It is therefore

very important to have a stable pulse train which does not change over time.

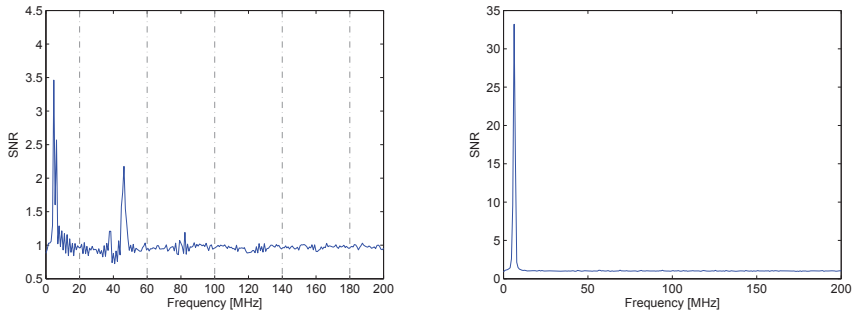

(a) (b)

Figure 7.5: (a) Wind speed measured with the FSPT modulated lidar focused at 180 m but also showing a wind speed result for a closer distance. The dashed vertical lines indicate the different frequency slots. (b) Wind speed measured with the lidar in standard CW mode focused at 260 m.

7.2.2 Second wind speed measurement

In this measurement an electrical bandpass filter is added to the setup a illustrated in Fig. 7.1. In practice the filter consists of a lowpass and a highpass filter connected in series. The lowpass filter has a cut-off around 190 MHz and is used for eliminating high frequency noise which would otherwise be aliased into the spectrum. The highpass filter has a cut-off frequency of 27 MHz and is used to remove the DC component from the signal as well as frequency components originating from the steep flanks of the pulses in the FSPT as described in Section 7.1.2. The pulses generated by the LSFS are 1 μs and the time between pulses, T_{inter}, is 0.25 μs. As shown in Fig. 7.3(d), however, the highpass filter itself introduces some parasitic oscillations in the beginning and in the end of each pulse and therefore a part of the pulse must be discarded. This is done by letting the computer search for the high spike at the beginning of the pulse and then remove the desired number of measured points. Because of the highpass filter the first range cell is shielded off and wind from here is not measured, but the second and third range cell are fully available and are centered around 187.5 m and 375 m.

Figs. 7.6(a) and 7.6(b) show two examples of measurements with the high-pass filtered lidar signal and the focus of the beam at the center of the third range cell. Fig. 7.6(a) is a measurement with the lidar beam pointing generally

against the wind direction so that a positive Doppler shift is obtained. Even though the beam is focused in the centre of the third range cell a peak of almost equal height is seen in the second range cell. The two peaks are situated at 31.37 MHz and 71.37 MHz equivalent of a wind speed of $+6.68 \pm 0.30$ m/s for both ranges along the LOS towards the lidar and with SNR values of 3.14 and 3.23, respectively. However, based on the close agreement in Doppler shift between the two frequency slots it seems natural to suspect that both originate from the same range and that this is due to the partially overlapping range cells. The suspicion is reinforced by the measurement shown in Fig. 7.6(b) where the beam is now staring along the wind. Again two distinct peaks are seen in the second and third range cell at 50.20 MHz and 90.98 MHz corresponding to 7.87 ± 0.30 m/s and 8.50 ± 0.30 m/s along the LOS away from the lidar and with SNR values of 3.40 and 2.86, respectively. However, the Doppler shift in the two frequency slots only differ by 780 kHz which is the same as one frequency bin so the difference between them is the smallest possible. Note that the sign of the wind velocity is determined by on which side of the centre of the frequency slot the Doppler peak is located. In both examples shown here the SNR values lie around 3. For comparison the SNR of a CW lidar measurement was 42.17 and there is thus a factor of 14 in difference between the CW and the FSPT measurement. Again, ripples in the noise floor around 40 MHz are noticed. Nevertheless, these measurements clearly demonstrate the ability of the FSPT modulated lidar to distinguish the sign of the Doppler shift and thereby direction of the wind.

7.2.3 Third wind speed measurement

The EDFA used in all measurements including those presented in Chapters 5 and 6 up until now has been a commercial 24 dB gain amplifier from Keopsys. It has been working satisfactory so far and the measurements presented in Chapter 5 revealed no apparent increase in noise level as function of pulse number even for pulse trains longer than 100 pulses. However, during the work with the LSFS installed in the FSPT modulated lidar, it turned out after all that the noise in the spectrum did in fact increase rapidly with the number of pulses, and a measurement showed that the noise figure (NF) of the amplifier is about 8 dB when operated in the regime required by the LSFS. This is considerably higher than the 3 dB in the quantum limit and also higher than what would be expected from a well designed amplifier [78]. As a first attempt to correct this, a new EDFA was therefore constructed based on about 5 m of Erbium doped single-mode fibre (SMF). A 980 nm pump diode and

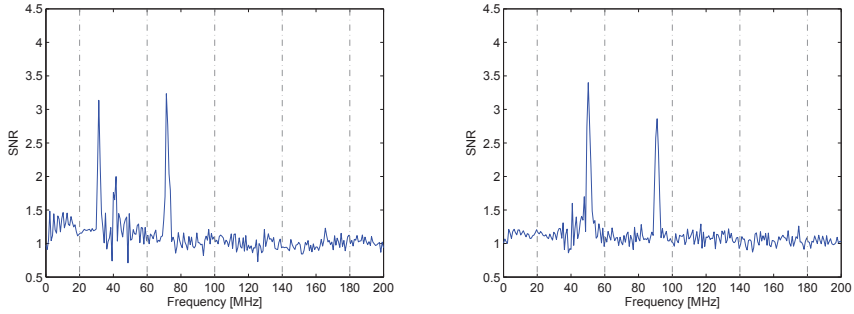

(a) (b)

Figure 7.6: (a) Wind speed measurement with the FSPT modulated lidar pointing into the wind. The measured wind speed is $+6.68 \pm 0.30$ m/s in both range cells. (b) Wind speed measurement with the FSPT modulated lidar pointing along the wind. The measured wind speeds are 7.87 ± 0.30 m/s and 8.50 ± 0.30 m/s in the two range cells separated by only one bin.

a forward pumping scheme were chosen to minimize the NF because, with an overall loss in the ring of about 10 dB, a high gain is not crucial [79]. A schematic drawing of the amplifier is shown in Fig. 7.7. Apart from Erbium doped fibre and pump diode it only consists of a wavelength division multiplexing (WDM) coupler for combining signal and pump, and an isolator for eliminating backward propagating amplified spontaneous emission (ASE) in the ring. The length of the fibre is simply determined by the fibre available so no special considerations have been made regarding this or the doping level. Despite this a NF of 4 dB has been measured in the relevant regime and it thus performs considerably better than the previous EDFA.

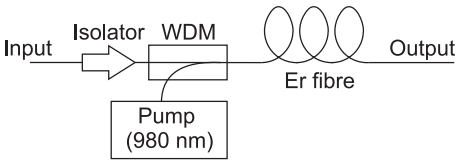

Figure 7.7: Sketch of the EDFA build for the LSFS. The amplifier is forward pumped by a 980 nm diode and the Erbium doped fibre is approximately 5 m in length. The isolator is used to ensure unidirectional propagation in the LSFS.

Another improvement compared to the previous measurements is the data

sampling. Here data is stored in a matrix format such that each column represents one pulse train and in units of voltage. The data storage is synchronized with the FSPT by the use of a common trigger supplied by pulse generator so every time a pulse train is initiated a trigger signal goes to the digitizer and a new measurement is started. As a result any jitter in the trigger signal is eliminated and if removal of the first part of the pulses is desired, it can be done by simply defining a constant time delay with no need of searching through all the sampled data, thus reducing the processing time considerably.

Fig. 7.8 shows two wind speed measurements, one obtained with the FSPT modulated lidar with the home built EDFA in the LSFS and segmented data storage, and one with the lidar in CW mode for reference. The laser beam is in both measurements focused at 170 m from the telescope near the centre of the second range cell. In Fig. 7.8(a) a peak is seen at 47.84 MHz with a height of 6.44 in agreement with the focus being in the second range cell. The Doppler shift of 7.84 MHz corresponds to a LOS wind speed of 6.07 ± 0.30 m/s. In contrast to what was experienced in Fig. 7.6, a wind signal is only observed in the second frequency slot. This we ascribe to the shorter focus range and the following smaller geometric probe length resulting in lower weighting functions of the first and third range cells. The noise floor seems more flat than what was seen in the other measurement campaigns with the ripples in the centre of the frequency slots less pronounced. However, during the measurements it became clear that once in a while spikes would occur around 40 MHz in the normalized spectrum. This strongly indicates that something regarding the non-shifted light trailing by one frequency shift is not stable, but an explanation for this phenomenon has yet to be found. For comparison Fig. 7.8(b) depicts a CW measurement showing a wind induced Doppler shift of 7.84 MHz and a SNR value of 19.72 is seen. The Doppler shift matches the one measured by the FSPT modulated measurement while the SNR value is about a factor of three higher. This is a significant improvement to the factor of fourteen and ten observed in Sections 7.2.1 and 7.2.2. It is therefore intriguing to that the new EDFA has improved the sensitivity of the FSPT modulated lidar, but further investigations are necessary to verify this.

7.2.4 Noise

As learned in the previous sections the SNR achieved with the FSPT modulated lidar is considerably lower than with the CW lidar, and high scattering conditions are necessary for the former to work satisfactory. There can be several reasons for this. For instance the system is designed such that the LO

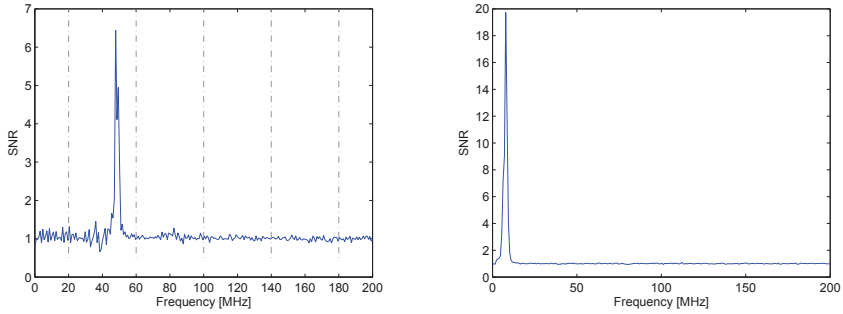

(a) (b)

Figure 7.8: (a) Wind speed measured with the FSPT modulated lidar focused at 170 m. The wind speed measured is 6.07 m/s. (b) Wind speed measured with the lidar in standard CW mode focused at 170 m. The measured wind speed is 6.07 m/s.

power at the detector is very near the saturation point of the detector as this ensures maximum shot noise domination. Though, it also implies that a slight increase in power will lead to saturation, decreasing drastically the sensitivity. This can very easily become a problem for the FSPT modulated lidar if the output envelope is not completely flat so that part of the pulse train saturates the detector. Or the opposite situation can occur where some pulses are low in power and shot noise domination is not achieved. Furthermore, the frequency response of the detector must be taken into account. When operated in CW mode with a non-shifted LO, only frequency shifts from 0 MHz to 25 MHz are considered and in this range roughly 6 dB of shot noise domination can be achieved with the present detector [80]. However, when used as an FSPT modulated lidar, frequency shifts up to 200 MHz are measured and in this range the response will have dropped by 3 dB according to the detector spec sheet.

The basic concept of the LSFS with a recirculating pulse also leads to a degradation of the SNR because for every revolution the amplifier contributes with additional ASE, incoherently adding, thus raising the noise floor. It is further expected that the data processing procedure influences how the noise level grows in the beat spectrum as function of pulse number in the FSPT. Therefore, the following measurements have been carried out for each of the methods presented in Sections 7.2.1-7.2.3. Pulse trains consisting of twenty 1 μs pulses are generated, sampled, and processed pulse by pulse. From each pulse 0.52 μs is used, equivalent of 208 data points when sampled at 400 MS/s,

a cosine window function is applied to reduce spectral leakage from the strong peaks at 40 MHz, and 80 MHz, and the length of the DFT is also 208 points resulting in a bin width of 1.92 MHz. In each measurement data from a full buffer are used, in this case resulting in approximately 205 pulse trains. The raw spectra belonging to each pulse number are then averaged and finally the average noise level between 55 MHz and 65 MHz for each pulse number is found.

Fig. 7.9(a) shows the noise level as function of pulse number relative to the noise level when no light is incident on the detector, i.e. the dark noise, for five different measurement configurations:

CW: Standard CW lidar configuration

1: Keopsys EDFA, and unfiltered electrical signal as described in Section 7.2.1

2: Keopsys EDFA, and electrical signal bandpass filtered as described in Section 7.1.2

3: Keopsys EDFA, electrical signal bandpass filtered, and data stored in matrix format as described in Section 7.2.2

4: Home build EDFA, electrical signal bandpass filtered, and data stored in matrix format

The digitizer voltage span is set to 0.5 V, even though with the bandpass filtered measurements it is possible to go down to 0.2 V. The CW measurement is, for obvious reasons, not pulsed and is therefore depicted as a constant of 1.55 dB above the dark noise level for all twenty pulses. This is assumed to be the shot noise floor, seen to be considerably lower here around 60 MHz than the 6 dB shot noise domination at lower frequencies [80]. However, the noise levels of the pulsed measurements show a similar and rapid increase as function of pulse number from about 2 dB to about $7-9$ dB above the dark noise. Measurement 1 has the lowest starting point of 0.74 dB, which is actually below the level of the CW measurement, but number 4 has the smallest increase compared to the starting point. This is more easily seen in Fig. 7.9(b) which shows the noise level relative to the noise level of the first pulse. Curve 4 increases relatively smoothly to 4.51 dB above the starting point. Curves 1 and 2 more or less follow each other up to a level of 6.5 dB, although number 2 is less smooth. Finally, number 3 ends at a level of 7.67 dB above its starting point. This strongly supports the presumption that the introduction of a new EDFA has

helped to bring the noise level of the measurement down. It would be of great interest to design an amplifier specifically for the use in the LSFS and FSPT modulated lidar, just more work on the noise in the FSPT modulated lidar in general is needed.

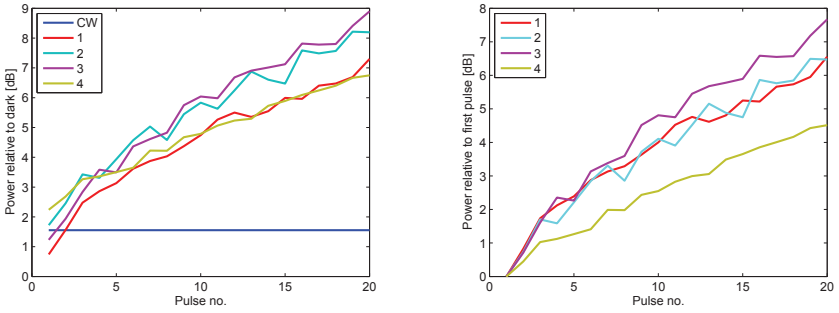

(a) (b)

Figure 7.9: (a) Noise level between 55 MHz and 65 MHz as function of pulse number compared to the noise level when no light is incident on the PD. (b) Noise level as function of pulse number compared to the noise level in the first pulse.

7.3 Summary

In this chapter the ability of the FSPT modulated lidar to remotely measure the speed of the wind has been demonstrated through three different measurements. Between the measurements the lidar itself and the data processing procedure have undergone different modifications to improve the performance of the lidar, both with regard to the sensitivity as well as to the processing time. The most important modification is probably the introduction of a new EDFA which has been constructed with a forward propagating 980 nm pump with the purpose of reducing the ASE. This EDFA shows considerably better performance with a measured NF of around 4 dB than the previously used amplifier which had an NF around 8 dB. Furthermore, it has no difficulties delivering the necessary gain of 10 dB. This has seemingly led to an improvement in the lidar sensitivity, but even though the new amplifier performs better than the old one, it is important to note that when using a loss compensated recirculation loop as the LSFS for light source, the amplifier will always contribute to increasing the noise level. The work on minimizing the optical noise in the

FSPT and to understand its influence on lidar performance therefore continues. Another benefit of the new EDFA is that full insight into all details such as fibre length and pump power etc. is now available enabling an update of the model presented in Chapter 5, paving the way for a better understanding of the physical processes involved in generating an FSPT suited for reliable wind speed measurements.

The large difference between top and bottom of the pulses which proved to be a challenge, was solved by inserting an electrical highpass filter in the lidar, although this resulted in the lidar being blinded in the first range cell. An important improvement would be to remove this restriction, and different ideas for doing so, including a better resolved digitizer and an electrical integrating circuit for subtracting the envelope function from the pulse train, are currently under consideration.

CHAPTER 8

Conclusion

The knowledge of atmospheric wind speeds is important within various fields of research as well as industries including, meteorology, aerospace, and wind energy. A tool for measuring the wind speed is the Doppler lidar which, since its commercial emergence about ten years ago, has been playing an increasingly important role, especially within the wind energy industry. Wind lidars has been the subject of this thesis, with special focus on the light source, i.e. the laser providing the basis for lidar measurements.

A brief introduction to the broad field of lidars has been given and the principles underlying wind lidars described. This included a description of a basic lidar setup, the difference between focused and range gated systems, the important phenomenon of heterodyne detection, and the various demands put on the laser by the lidar. The concept of an frequency stepped pulse train (FSPT) modulated lidar as a type of lidar combining the advantages of fast measurements of a continuous wave (CW) system with the inherent range gating of a pulsed system was introduced.

The FSPT modulated lidar mainly separates itself from other wind lidars in that the light source needs to be a hybrid between conventional CW and pulsed lasers. Such a light source, the lightwave synthesized frequency sweeper (LSFS), has been described in detail, including the acousto-optic modulator (AOM) which works as frequency shifter and the fibre optical amplifier used for compensating the loss in the loop. Two different amplifiers, an Erbium doped fibre amplifier (EDFA) and a Raman amplifier, were tested in the setup and both were found capable of delivering the necessary gain to compensate the losses. However, the relatively low pump to signal conversion efficiency of the Raman amplifier meant that a longer fibre was necessary than for the EDFA, which again resulted in the pulses generated by the Raman assisted LSFS being too

long to be used with the FSPT modulated lidar. The long pulses also led to the shape of the pulses changing with the number of revolutions as a result of amplifier pump depletion. A time dependent model of the LSFS, capable of describing the individual pulses in the pulse train as well as the pulse train envelope was developed and tested against experiments. As for the physical LSFS, either an EDFA or a Raman amplifier were used in the model but in general the agreement between measurements and simulations was better for the Raman assisted LSFS. This was partly ascribed to the fact that the EDFA is a commercial product and the exact properties such as fibre length or doping levels are not known.

The spectral properties of the FSPT were investigated using a time gated measurement of the beat spectrum between the individual pulses and a CW local oscillator (LO). The frequency stability of the pulses proved to be very high owing to the stable laser and AOMs used. However, the measurements also revealed parasitic noise at integer multiples of the frequency shift induced by the AOM, and this was attributed to light leaking through the AOM without being frequency shifted. The amount of light not shifted was measured using an interferometric setup including two AOMs and used as a parameter in a model made to describe the build-up of noise in the ring. The model is an expansion of a time independent model describing the LSFS adopted from the literature. The model showed qualitatively the same behaviour of the build-up of noise as observed in measurements, but was not able to accurately predict the noise level. This was speculated to relate to the fact that the time independent LSFS model underlying this simulation is less accurate than the time dependent LSFS model.

Finally, the LSFS was coupled to a CW lidar system to establish an FSPT modulated lidar system. Measurements of wind speed were successfully achieved, although only in hazy weather, demonstrating the functionality of lidar as well as its ability to distinguish the sign of the Doppler shift. However, measurements were only successful using a focused beam. This is because the lidar is not nearly as sensitive when operating in the FSPT modulated mode as in CW mode. Measurements showed that noise quickly builds up in the pulses suppressing the shot noise domination. In order to increase the sensitivity, it is thus vital to reduce this noise as much as possible. Work on this is ongoing as we shall return to shortly.

Lidars are increasingly being used for active control of wind turbines and it seems natural that the next step will be to implement lidars in the turbine wings for active pitch control. An initial study investigating the potential risks impeding the feasibility of such an implementation, has been presented. The

risks considered included saturation of the detector due to reflections from the ground, loss of signal strength due to misalignment of receiver and backscattered signal, and loss of sensitivity due to broadening of the signal caused by the movement of the transceiver. The analysis led to the conclusion that the considered risks are unlikely to stand in the way for a successful realization of the envisioned blade-mounted lidar system. The positive outcome of the risk analysis led to the testing of a system designed for implementation in a turbine blade, carried out in a high-performance wind tunnel. The trial mainly focused on testing the lidar performance at various wind speeds up to 75 m/s, and it showed very good agreement with the two reference measurement systems used; so good that lidars one day might become part of standard wind tunnel equipment. The testing further allowed for an experimental confirmation of the studied phenomenon of spectral broadening occurring when aerosols move quickly through the lidar beam. A good match with the derived dependency of this so-called speckle broadening on the wind speed was found, while for all wind speeds, the measured broadening exceeded the derived one by a constant offset. The digital signal processing was given as a plausible explanation for this.

In conclusion, the main achievement during this PhD project was the establishment of an LSFS setup which in combination with a FSPT modulated lidar, modified for the purpose, resulted in successful demonstrations of the ability to measure, not only the wind speed, but also the wind direction.

However, there are still many unresolved issues concerning the FSPT modulated lidar, not least the optical noise building up in the ring during repeated recirculation and amplification; a noise that can never be completely eliminated with the recirculation loop used. Nonetheless, a new EDFA being designed, optimized for minimizing noise in the LSFS is expected to improve the signal to noise ratio. With an increased signal to noise ratio (SNR) measurements can hopefully be performed more regularly in all weather conditions, and the accuracy regarding wind speed can be investigated. Also the highly dynamic signal of the FSPT presents a challenge which needs to be addressed, e.g. through implementation of an integrating circuit. Finally, if a tighter spatial confinement is desired, shorter pulses are necessary, imposing further requirements on the data processing .

APPENDIX A

Wind tunnel trial correlation plots

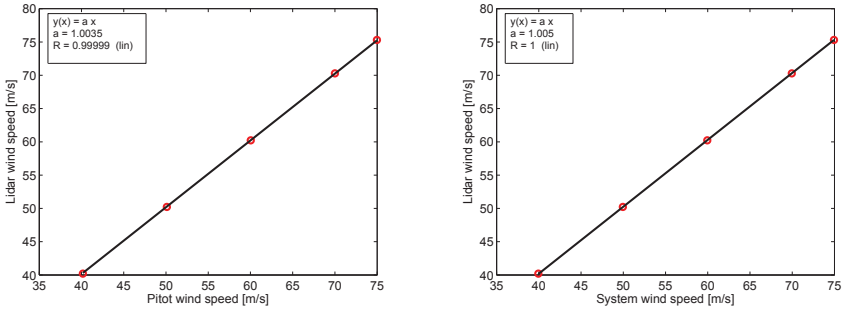

(a) (b)

Figure A.1: Plot of the mean wind speeds in the initial "high speed test" measured by the lidar against the wind speeds measured by the reference Pitot tube (a) and System (b).

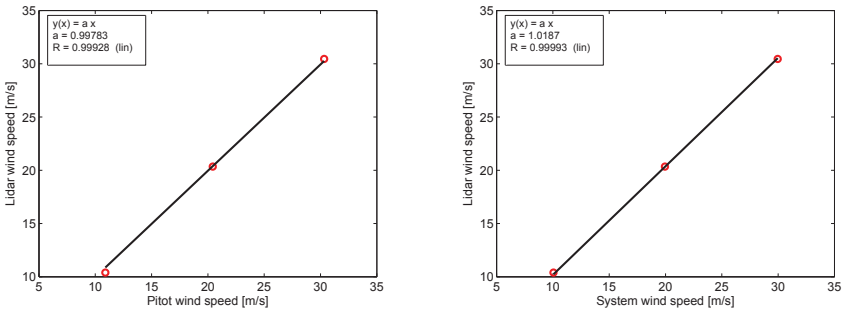

(a) (b)

Figure A.2: Plot of the mean wind speeds in the "short range test" measured by the lidar with a focus length of 1.3 m against the wind speeds measured by the reference Pitot tube (a) and System (b).

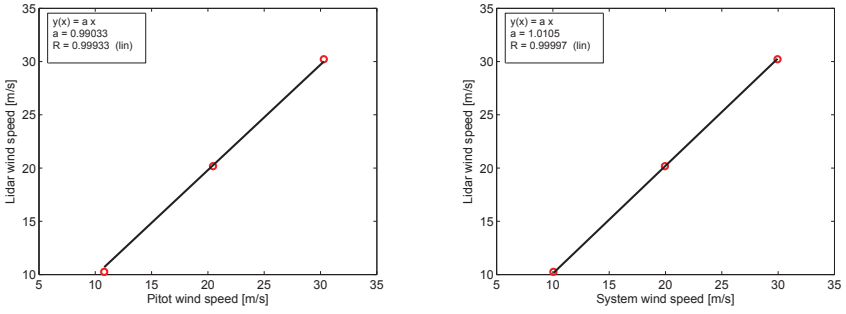

(a) (b)

Figure A.3: Plot of the mean wind speeds the "long range test" measured by the lidar with a focus length of 5.9 m against the wind speeds measured by the reference Pitot tube (a) and System (b).

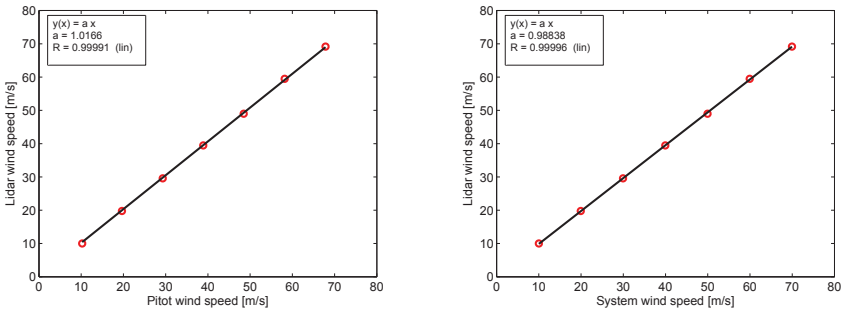

(a) (b)

Figure A.4: Plot of the mean wind speeds in "the turbulent wind flow test" measured by the lidar against the wind speeds measured by the reference Pitot tube (a) and System (b).

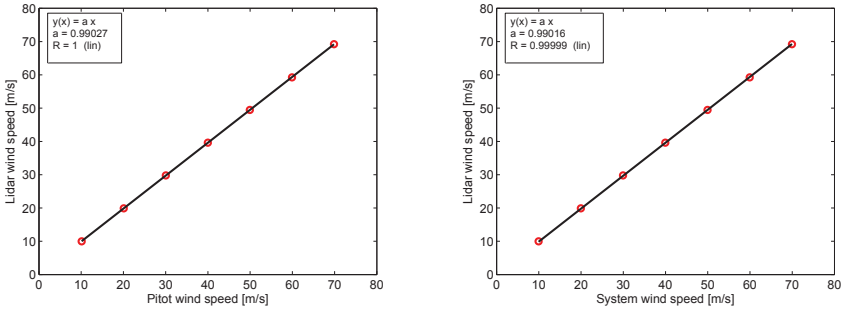

(a) (b)

Figure A.5: Plot of the mean wind speeds in the "high angle of attack test" measured by the lidar after correction for the angle of attack against the wind speeds measured by the reference Pitot tube (a) and System (b).

APPENDIX B

List of acronyms

ADC analog-to-digital converter

AOM acousto-optic modulator

ASE amplified spontaneous emission

BPD balanced photo detector

BPF bandpass filter

BPLO back propagating local oscillator

CNR carrier to noise ratio

CW continuous wave

DFT discrete Fourier transform

DSP digital signal processor

EDFA Erbium doped fibre amplifier

ESA electrical spectrum analyzer

FBG fibre Bragg grating

FFT fast Fourier transform

FSPT frequency stepped pulse train

FWHM full width at half maximum

FWM four-wave mixing

LSFS lightwave synthesized frequency sweeper

LOS line-of-sight

LO local oscillator

NF noise figure

ODE ordinary differential equation

OSA optical spectrum analyzer

PC polarization controller

PD photo detector

RF radio frequency

RIN relative intensity noise

SBS stimulated Brillouin scattering

SMF single-mode fibre

SNR signal to noise ratio

SOA semiconductor optical amplifier

SBS stimulated Brillouin scattering

SRS stimulated Raman scattering

TOF time-of-flight

VA variable attenuator

WDM wavelength division multiplexing

YDFA Ytterbium doped fibre amplifier

Bibliography

[1] Torben Mikkelsen. Remote Sensing of Wind. In Alfredo Peña and Charlotte B. Hasager, editors, *Remote sensing for wind energy*, pages 7–20. Risø DTU, 2011.

[2] Petter Lindelöw. *Fiber Based Coherent Lidars for Remote Sensing*. PhD thesis, Technical University of Denmark, November 2007.

[3] G. Comte-Bellot. Hot-wire anemometry. *Annual Review of Fluid Mechanics*, 8:209–231, 1976.

[4] Rex Klopfenstein Jr. Air velocity and flow measurement using a pitot tube. *ISA Transactions(R)*, 37(4):257–263, 1998.

[5] Gennaro H. Crescenti. The degradation of doppler sodar performance due to noise: a review. *Atmospheric Environment*, 32(9):1499–1509, 1998.

[6] `http://www.yourwindlidar.com/`. December 16, 2011.

[7] `http://www.lidarwindtechnologies.com/`. December 16, 2011.

[8] `http://www.sgurrenergy.com/`. December 16, 2011.

[9] `http://www.catchthewindinc.com/products`. December 16, 2011.

[10] F. Barbaresco, P. Juge, M. Klein, Y. Ricci, J. Schneider, and J. Moneuse. Optimising runway throughput through wake vortex detection, prediction and decision support tools. *Proceedings of 2011 Tyrrhenian international workshop on Enhanced Surveillance of Aircraft and Vehicles*, pages 27–32, 2011.

[11] Scott M. Spuler, Dirk Richter, Michael P. Spowart, and Kathrin Rieken. Optical fiber-based laser remote sensor for airborne measurement of wind velocity and turbulence. *Applied Optics*, 50(6):842–851, 2011.

[12] Takashi Fujii and Tetsuo Fukuchi. *Laser remote sensing*. CRC Press, 2005.

[13] U. Platt. Modern methods of the measurement of atmospheric trace gases invited lecture. *PCCP. Physical chemistry chemical physics*, 1(24):5409–5415, 1999.

[14] Claus Weitkamp, editor. *Lidar - Range-resolved optical remote sensing of the atmosphere*. Springer, 2005.

[15] Michael Harris, Graham Constant, and Carol Ward. Continuous-wave bistatic laser doppler wind sensor. *Applied Optics*, 40(9):1501–1506, 2001.

[16] M. Hand M. Harris and A. Wright. Lidar for turbine control. Technical Report NREL/TP-500-39154, National Renewable Energy Laboratory, January 2006.

[17] Jean-Pierre Cariou. Pulsed lidars. In Alfredo Peña and Charlotte B. Hasager, editors, *Remote sensing for wind energy*, pages 65–81. Risø DTU, 2011.

[18] Rene Skov Hansen and Christian Pedersen. All semiconductor laser doppler anemometer at 1.55 mu m. *OPTICS EXPRESS*, 16(22):18288–18295, 2008.

[19] Jean-Pierre Cariou, Beatrice Augere, and Matthieu Valla. Laser source requirements for coherent lidars based on fiber technology. *Comptes Rendus Physique*, (2):213, 2006.

[20] Anders Tegtmeier Pedersen, Lars Gruner-Nielsen, and Karsten Rottwitt. Measurement and modeling of low-wavelength losses in silica fibers and their impact at communication wavelengths. *Journal of Lightwave Technology*, 27(10):1296–1300, 2009.

[21] Harris, Pearson, Vaughan, Letalick, and Karlsson. The role of laser coherence length in continuous-wave coherent laser radar. *Journal of Modern Optics*, 45(8):1567–1581, 1998.

[22] Jack A McKay. Remote sensing - modeling of direct detection doppler wind lidar. i. the edge technique. *Applied Optics*, 37(27):6480, 1998.

[23] Jack A McKay. Modeling of direct detection doppler wind lidar. ii. the fringe imaging technique. *Applied Optics*, 37(27):6487–6493, 1998.

[24] G. P. Agrawal. *Fiber-optic communication systems*. Wiley, 2002. Wiley series in microwave and optical engineering.

[25] G.A. Ball, G. Hull-Allen, C. Holton, and W.W. Morey. Low noise single frequency linear fibre laser. *Electronics Letters*, 29(18):1623–1625, 1993.

[26] Michael Harris. Introduction to continuous-wave Doppler lidar. In Alfredo Peña and Charlotte B. Hasager, editors, *Remote sensing for wind energy*, pages 41–64. Risø DTU, 2011.

[27] C. M. Sonnenschein and F. A. Horrigan. Signal-to-noise relationships for coaxial systems that heterodyne backscatter from the atmosphere. *Applied optics.*, 10(7):1600–1604, 1971.

[28] A. E. Siegman. *Lasers*. University Science Books, 1986.

[29] Christian Werner, Friedrich Koepp, and Ronald L. Schwiesow. Influence of clouds and fog on lda wind measurements. *Applied Optics*, 23(15):2482–2484, 1984.

[30] Petter Lindelöw and Johan Jacob Mohr. Coherent lidar modulated with frequency stepped pulse trains for unambiguous high duty cycle range and velocity sensing in the atmosphere. *International Geoscience and Remote Sensing Symposium (IGARSS)*, pages 2787–2790, 2008.

[31] Petter Lindelöw. Velocity sensing FSPT-modulated coherent lidar. In *Proceedings of 14th Coherent Laser Radar Conference*, 2007.

[32] Michael Harris, David J. Bryce, Adrian S. Coffey, David A. Smith, Jochen Birkemeyer, and Ullrich Knopf. Advance measurement of gusts by laser anemometry. *Journal of Wind Engineering and Industrial Aerodynamics*, 95(12):1637–1647, 2007.

[33] Torben Mikkelsen, Kasper Hjorth Hansen, Nikolas Angelou, Mikael Sjöholm, Michael Harris, Paul Hadley, Richard Scullion, Gary Ellis, and G. Vives. Lidar wind speed measurements from a rotating spinner. *EWEC 2010 Proceedings online*, page 8, 2010.

[34] Frank L. Pedrotti, Leno Matthew Pedrotti, and Leno S. Pedrotti. *Introduction to optics*. Pearson Prentice Hall, 2007.

[35] J. H. Shaprio. Correlation scales of laser speckle in heterodyne-detection. *Applied Optics*, 24(12):1883–1888, 1985.

[36] E. Jakeman and K. D. Ridley. *Modeling fluctuations in scattered waves*. CRC Press, 2006. Series: Series in optics and optoelectronics.

[37] Andreas Fischer. Hot wire anemometer turbulence measurements in the wind tunnel of lm wind power. Technical Report Risø-R-2000(EN), Risø DTU, Roskilde, Denmark, February 2011.

[38] `http://www.mathworks.com/matlabcentral/fileexchange/10176`. May 21, 2012.

[39] Personal communication with wind tunnel operator Olaf Müller.

[40] M. Harris, G. N. Pearson, K. D. Ridley, C. J. Karlsson, F. A. Olsson, and D. Letalick. Single-particle laser doppler anemometry at 1.55 μm. *Applied optics.*, 40(6):969–973, 2001.

[41] P. Coppin and T.G. Hodgkinson. Novel optical frequency comb synthesis using optical feedback. *Electronics Letters*, 26(1):28–30, 1990.

[42] Aida and Nakagawa. Time shared lightwave reference frequency distribution for photonics networks. *Journal of Lightwave Technology*, 14(6):1153–1160, 1996.

[43] Frederik D. Nielsen, Lars Thrane, Peter E. Andersen, John F. Black, and Anders Bjarklev. Swept wavelength source in the 1 μm range. *Optics Express*, 13(11):4096–4106, 2005.

[44] H. Takesue and T. Horiguchi. Chromatic dispersion measurement of optical components using lightwave synthesized frequency sweeper. *Journal of Lightwave Technology*, 20(4):625–633, 2002.

[45] Takesue and Horiguchi. Broad-band lightwave synthesized frequency sweeper using synchronous filtering. *Journal of Lightwave Technology*, 22(3):755–762, 2004.

[46] Takesue, Yamamoto, Shimizu, and Horiguchi. 1 THz lightwave synthesised frequency sweeper with synchronously tuned bandpass filter. *Electronics Letters*, 34(15):1507–1508, 1998.

[47] Takesue, Yamamoto, Shimizu, and Horiguchi. Stabilization of pulsed lightwave circulating around an amplified fiber-optic ring incorporating a Lyot depolarizer. *IEEE Photonics Technology Letters*, 10(12):1748–1750, 1998.

[48] Paola Parolari, Lucia Marazzi, Pierpaolo Boffi, and Mario Martinelli. Amplified recirculating circuits for pseudo-continuous wave generation. *Optics Communications*, 165(4-6):195–198, 1999.

[49] K. Shimizu, T. Horiguchi, and Y. Koyamada. Frequency translation of light waves by propagation around an optical ring circuit containing a frequency shifter: Ii. theoretical analysis. *Applied Optics*, 33(15):3209–3219, 1994.

[50] Katsumi Takano, Kiyoshi Nakagawa, and Hiromasa Ito. Influence of optical filters on pulse circulation in fiber rings with a frequency shifter and EDFA. *Optics Express*, 14(22):10313–10323, 2006.

[51] Anders Sig Olesen. Frequency stepped pulse train generator. Master's thesis, Technical University of Denmark, 2010.

[52] Anders Tegtmeier Pedersen and Karsten Rottwitt. Raman assisted lightwave synthesized frequency sweeper. *Proceedings of Optical Sensors*, 2010.

[53] Anders Tegtmeier Pedersen, Anders Sig Olesen, and Karsten Rottwitt. Accurate simulation of Raman amplified lightwave synthesized frequency sweeper. *Journal of the Optical Society of America B: Optical Physics*, 28(6):1493–1497, 2011.

[54] Akis P. Goutzoulis and Dennis R. Pape, editors. *Design and fabrication of acousto-optic devices*. Marcel Dekker, 1994.

[55] Adrianus Korpel. Acousto-optics - a review of fundamentals. *Proceedings of the IEEE*, 69(1):48–53, 1981.

[56] IntraAction Corp. Acousto-optic modulator - instruction manual. Instruction manual.

[57] David L. Hecht. Multifrequency acoustooptic diffraction. *IEEE Trans Sonics Ultrason*, SU-24(1):7–18, 1977.

[58] André Pérennou, Véronique Quintard, Yves Mevel, and Jean Le Bihan. Intermodulation product effects on the working of a phased-array transducer acousto-optic switch. *Optical engineering*, 43(5):1042–1050, 2004.

[59] G. P. Agrawal. *Nonlinear fiber optics*. Elsevier, 4. ed. edition, 2007. Previous ed.: 2001.

[60] K. Rottwitt and A. J. Stentz. Raman amplification in lightwave communication systems. In Ivan Kaminow and Tingye Li, editors, *Optical Fiber Telecommunication IV A*, pages 213–257. Academic Press, 2002.

[61] Giles and Desurvire. Propagation of signal and noise in concatenated Erbium-doped fiber optical amplifiers. *Journal of Lightwave Technology*, 9(2):147–154, 1991.

[62] Giles and Desurvire. Modeling Erbium-doped fiber amplifiers. *Journal of Lightwave Technology*, 9(2):271–283, 1991.

[63] J. Bromage. Raman amplification for fiber communications systems. *Journal of Lightwave Technology*, 22(1):79–93, 2004.

[64] Chien-Jen Chen and W. S. Wong. Optical communication - transient effects in saturated Raman amplifiers. *Electronics Letters*, 37(6):371, 2001.

[65] Anders Tegtmeier Pedersen and Per Jonas Petter Lindelöw. Investigation of noise in lightwave synthesized frequency sweeper seeded lidar anemometers from leakage through the acousto optic modulators. *CLRC 15th Coherent Laser Radar Conference*, 2009.

[66] P.W. Milonni and J.H. Eberly. *Lasers*. Wiley, 1988.

[67] Dawson, Park, and Vahala. An improved delayed self-heterodyne interferometer for linewidth measurements. *IEEE Photonics Technology Letters*, 4(9):1063–1066, 1992.

[68] Hanne Ludvigsen, Mika Tossavainen, and Matti Kaivola. Laser linewidth measurements using self-homodyne detection with short delay. *Optics Communications*, 155(1-3):180–186, 1998.

[69] Kendra L. Letchworth and D. Chris Benner. Rapid and accurate calculation of the Voigt function. *Journal of Quantitative Spectroscopy and Radiative Transfer*, 107(1):173–192, 2007.

[70] Mercer. 1/f frequency noise effects on self-heterodyne linewidth measurements. *Journal of Lightwave Technology*, 9(4):485–493, 1991.

[71] Horak and Loh. On the delayed self-heterodyne interferometric technique for determining the linewidth of fiber lasers. *Optics Express*, 14(9), 2006.

[72] Xiaopei Chen, Ming Han, Yizheng Zhu, Bo Dong, and Anbo Wang. Implementation of a loss-compensated recirculating delayed self-heterodyne interferometer for ultranarrow laser linewidth measurement. *Applied Optics*, 45(29):7712–7717, 2006.

[73] `http://www.nktphotonics.com/files/files/adjustik\%20system-110325.pdf`. December 4, 2011.

[74] C Zhang, K. K. Y. Cheung, P. C. Chui, K. K. Tsia, and K. K. Y. Wong. Fiber and waveguide amplifiers and lasers - fiber-optical parametric amplifier with high-speed swept pump. *IEEE Photonics Technology Letters*, 23(16-16):1022, 2011.

[75] Anders Sig Olesen, Anders Tegtmeier Pedersen, and Karsten Rottwitt. Simultaneous measurements of wind speed at multiple distances without range ambiguity. *CLRC 16th Coherent Laser Radar Conference*, 2011.

[76] Anders Sig Olesen, Anders Tegtmeier Pedersen, and Karsten Rottwitt. Frequency stepped pulse train modulated wind sensing lidar. *Proceedings of SPIE–the international society for optical engineering*, 8159(1):81590O–8, 2011.

[77] John G. Proakis and Dimitris G. Manolakis. *Digital signal processing / principles, algorithms, and applications*. Pearson, 2007.

[78] E. Desurvire. Erbium-Doped Fiber Amplifiers: Basic Physics and Characteristics. In Michel J. F. Digonnet, editor, *Rare-Earth-Doped Fiber Lasers and Amplifiers*, pages 531–582. Marcel Dekker, 2001.

[79] Olshansky. Noise figure for Erbium-doped optical fibre amplifiers. *Electronics Letters*, 24(22):1363–1365, 1988.

[80] Paul Hadley and Michael Harris. ZephIR service and repair report - prototype ZephIR. Technical report, Natural Power, July 2010.

ISBN: 87-92062-77-6

Published by:
DTU Fotonik
Department of Photonics Engineering
Technical University of Denmark
Ørsteds Plads, building 343
DK-2800 Kgs. Lyngby

Anders Tegtmeier Pedersen was born in Næstved, Denmark in 1981. He received the M. Sc. in engineering physics in 2007 from DTU with a thesis on attenuation of light in optical fibres. He then worked as a research assistant at DTU Fotonik and Danish Fundamental Metrology before starting his PhD in the fall of 2008. The PhD work was concerned with remote sensing of wind speed using laser light and included development and characterization of a fibre based laser source as well as wind speed measurements under different conditions.

DTU Fotonik
Department of Photonics Engineering

Printed in Denmark by SaloPrint, 2620 Albertslund